Characterization of Flapping Wing Aerodynamics and Flight Dynamics Analysis using Computational Methods

by

ALOK ASHOK REGE

Presented to the Faculty of the Graduate School of
The University of Texas at Arlington in Partial Fulfillment
of the Requirements
for the Degree of

DOCTOR OF PHILOSOPHY

THE UNIVERSITY OF TEXAS AT ARLINGTON

December 2015

Copyright © by ALOK ASHOK REGE 2015

All Rights Reserved

To my parents,

Anagha and Ashok Rege,

And my grandparents,

Mangala and Rajaram Bilaye

Nalini and Pandurang Rege

ACKNOWLEDGEMENTS

I begin this acknowledgement by expressing my deepest gratitude to my supervising professor Dr. Kamesh Subbarao, without whom I would not have seen this day. I would have never known my potential had he not backed me even before I was here. It has been five years since I have known him. All this while he has pushed me hard to set high standards for myself.

I also extend my deepest gratitude to my thesis co-supervisor Dr. Brian Dennis for his continued support and guidance. He has always been very resourceful and has helped me in formulating my research core.

I am deeply honored and privileged to have had Dr. Frank Lu, Dr. Zhen Han and Dr. Manfred Huber as committee members. I am grateful to Dr. Lu for encouraging me to dissect work of others and more importantly, be critical of one's own work. I thank Dr. Huber for imparting knowledge during each of our meetings. I thank Dr. Han for giving invaluable insights into my research.

Words fail me to describe the kind of love and affection I have received from Debi Barton, Lanie Gordon, Sally Thompson, Janet Gober, Kathy Priester and Louella Carpenter. They never made me miss my mom.

I would like to thank my colleagues from Aerospace Systems Laboratory (ASL) and Computational Fluid Dynamics Laboratory (CFDLAB) for their invaluable friendship. I would also like to thank all my close friends in the US for being with me during my low phases and sharing my successes. I am thankful to my current and past roommates for tolerating my OCD.

Finally, I thank all my family members, well-wishers and friends for helping me out in every possible way. I am also grateful to all my past and present teachers who have a played a big part in me getting here.

I wouldn't be pursuing PhD if not for the support of few people, namely Harish Shah, Prakash Mayekar, Kiran Rege, Chhaya-Narendra Rane, Saiprasad Vaingankar, Kunal Mayekar and Shailesh Bilaye. Y'all made this happen.

I cannot begin to stress the importance of my parents in my life. My dad has stood by me through very rough times, allaying all my fears and giving me enough strength to stand the test of time. My mother has provided a gentle balm to heal me from all my failures. Most importantly, they managed to keep me grounded when I tasted success. In their well-being and prosperity alone lies my happiness!

November 16, 2015

ABSTRACT

Characterization of Flapping Wing Aerodynamics and Flight Dynamics Analysis using Computational Methods

ALOK ASHOK REGE, Ph.D.

The University of Texas at Arlington, 2015

Supervising Professors: Kamesh Subbarao and Brian H Dennis

Insect flight comes with a lot of intricacies that cannot be explained by conventional aerodynamics. Even with their small-size, insects have the ability to generate the required aerodynamic forces using high frequency flapping motion of their wings to perform different maneuvers. The maneuverability obtained by these flyers using flapping motion belies the classical aerodynamics theory and calls for a new approach to study this highly unsteady aerodynamics. Research is on to find new ways to realize the flight capabilities of these insects and engineer a micro-flyer which would have wide range of applications, including but not limited to

- Autonomous Pollination of crop fields;
- High Resolution Weather and Climate Mapping;
- Traffic Monitoring;
- Oil & Gas Exploration; and
- Area Surveillance, Detection & Rescue Missions

In this research, a parametric study of flapping trajectories is performed using a two-dimensional wing to identify the factors that affect the force production. These

factors are then non-dimensionalized and used in a design of experiments set-up to conduct sensitivity analysis. A procedure to determine an aerodynamic model comprising cycle-averaged force coefficients is described. This aerodynamic model is then used in a nonlinear dynamics framework to perform flight dynamics analysis using a micro-flyer with model properties based on *Drosophila*. Stability analysis is conducted to determine different steady state flight conditions that could achieved by the micro-flyer with the given model properties. The effect of scaling the mass properties is discussed. An LQR design is used for closed-loop control. Open and closed-loop simulations are performed. The results show that nonlinear dynamics framework can be used to determine values for model properties of a micro-flyer that would enable it to perform different flight maneuvers.

TABLE OF CONTENTS

ACKNOWLEDGEMENTS iv

ABSTRACT vi

LIST OF FIGURES xi

LIST OF TABLES xvi

Chapter Page

1. INTRODUCTION 1

1.1 Insect Flight 1

1.2 Literature Review 2

1.2.1 Aerodynamic Models used in Flight Dynamics 4

1.3 Research Objectives and Contributions 6

1.3.1 Objectives 6

1.3.2 Secondary Objectives 6

1.3.3 Original Research Contributions 7

1.3.4 List of Published Works 7

1.4 Dissertation Organization 8

2. PROPOSED METHODOLOGY AND PRELIMINARY STUDY 9

2.1 Parametric Study of Flapping Paths 9

2.1.1 Computational Grid 10

2.1.2 Flapping Trajectories 11

2.1.3 Computational Flow Solver 13

2.1.4 Results 17

2.2 Sensitivity Analysis using Non-Dimensional Parameters 22

2.2.1 Non-Dimensional Parameters 22
2.2.2 Design of Experiments 24
2.2.3 Results 29
3. STRUCTURED GRID FOR CFD STUDY 34
3.1 Rigid Body Dynamic Mesh Zone Motion with Structured Grid 34
3.2 Grid Convergence Study 36
3.3 Validation of the Numerical Implementation 39
3.3.1 Ramp Motion of NACA-0012 Airfoil 39
3.3.2 Two-Dimensional Flow over a Hovering Flapping Wing 44
4. RESULTS FOR PARAMETRIC STUDY OF FLAPPING PATHS 48
5. RESULTS FOR SENSITIVITY ANALYSIS WITH LARGE DOE 54
5.1 Role of Stroke Angle of Attack and Local Reynolds Number 55
5.2 Role of Stroke Angle of Attack and Strouhal Number 59
6. FLIGHT DYNAMICS ANALYSIS 62
6.1 Flight Dynamics Formulation 62
6.2 Micro-flyer Model 63
6.3 Aerodynamic Forces and Moments Calculation 66
6.4 Aerodynamic Model 69
6.4.1 Micro-flyer Body Drag 71
6.5 Governing Equations of Motion 72
6.5.1 Longitudinal Flight Dynamics 75
6.6 Simulation Parameters 76
6.7 Closed-Loop Control of Micro-flyer 77
6.7.1 Trim Analysis 77
6.7.2 System Linearization 79
6.7.3 Linear Control Design 80

6.7.4 Nonlinear Dynamics Open and Closed Loop Simulations . . . 81
6.8 Micro-flyer with Scaled Mass Properties 87
6.8.1 Combined Straight & Level and Climb Maneuver 88
6.9 Summary of Results 100
7. CONCLUDING REMARKS 101
7.1 Summary 101
APPENDIX
A. DERIVATIONS & FORMULAE 103
REFERENCES 105
BIOGRAPHICAL STATEMENT 113

LIST OF FIGURES

Figure Page

1.1 Flapping motion of an insect 2

1.2 Time history of lift (C_{L}) and drag (C_{D}) coefficients for 7 angle of attack values, taken from Dickinson et al. [1]. The dotted lines indicate the interval over which values are averaged 5

2.1 Flow chart for CFD analysis 10

2.2 Model of a wing section used for CFD analysis 11

2.3 Computational domain large and refined mesh 11

2.4 Figure-8 flapping path, (a) Flapping direction and (b) Instantaneous wing flapping positions 12

2.5 Straight flapping path, (a) Flapping direction and (b) Instantaneous wing flapping positions 12

2.6 Pictorial representation of a grid cell 14

2.7 Unstructured mesh around the wing section with smoothing and remeshing employed 16

2.8 C_{Lavg} convergence plot for figure-8 path 17

2.9 C_{Lavg} convergence plot for straight path 18

2.10 Velocity vector plot for figure-8 path (Inlet Velocity = 0.01 m/s, Original Outer Boundary) 19

2.11 Velocity vector plot for straight line path (Inlet Velocity = 0.01 m/s, Original Outer Boundary) 19

2.12 Velocity vector plot for figure-8 path (Inlet Velocity = 0.01 m/s, Increased Outer Boundary) 19

2.13 Velocity vector plot for straight line path (Inlet Velocity = 0.01 m/s, Increased Outer Boundary) 19

2.14 Velocity vector plot for figure-8 path (Inlet Velocity = 0.1 m/s, Original Outer Boundary) 20

2.15 Velocity vector plot for straight line path (Inlet Velocity = 0.1 m/s, Original Outer Boundary) 20

2.16 Velocity vector plot for figure-8 path (Inlet Velocity = 1 m/s, Original Outer Boundary) 21

2.17 Velocity vector plot for straight line path (Inlet Velocity = 1 m/s, Original Outer Boundary) 21

2.18 Stroke angle of attack α_S 24

2.19 Variation of wing path length over span 24

2.20 Re_l-St Surface plot for horizontal force coefficient C_{Xavg} at $\alpha_S = 0$ deg 29

2.21 Re_l-St Contour plot for horizontal force coefficient C_{Xavg} at $\alpha_S = 0$ deg 29

2.22 Re_l-St Surface plot for vertical force coefficient C_{Zavg} at $\alpha_S = 0$ deg 30

2.23 Re_l-St Contour plot for vertical force coefficient C_{Zavg} at $\alpha_S = 0$ deg 30

2.24 Re_l-α_S Contour plot for horizontal force coefficient C_{Xavg} at $St = 0.003$ 30

2.25 Re_l-α_S Contour plot for vertical force coefficient C_{Zavg} at $St = 0.003$ 30

2.26 Plot for C_{Xavg} versus St 31

2.27 Plot for C_{Zavg} versus St 31

2.28 Plot for C_{Xavg} versus α_S 32

2.29 Plot for C_{Zavg} versus α_S 32

2.30 Plot for C_{Xavg} versus Re_l 32

2.31 Plot for C_{Zavg} versus Re_l 32

3.1 Inner Structured Grid 35

3.2 Outer Structured Grid 35

3.3 Sliding interfaces at the boundary between the outer and inner grid shown in Fig. (a) and the corresponding flapping position of the flat

plate shown in Fig. (b) 36

3.4 Cycle-averaged vertical force coefficient 37

3.5 Cycle-averaged horizontal force coefficient 37

3.6 Structured grid for ramping motion 40

3.7 Clustered grid around the wall to resolve the turbulent boundary layer 40

3.8 Pitch angle variation over time for ramping motion 41

3.9 Comparison of normal force coefficient values for ramping motion . . . 43

3.10 Lift and drag coefficients during advanced rotation (ϕ=π/4; A_0/c=2.8) (a) Instantaneous wing positions (b) Results Comparison 45

3.11 Lift and drag coefficients during symmetric rotation (ϕ=0; A_0/c=2.8) (a) Instantaneous wing positions (b) Results Comparison 46

3.12 Lift and drag coefficients during delayed rotation (ϕ=$-\pi$/4; A_0/c=2.8) (a) Instantaneous wing positions (b) Results Comparison 46

4.1 Force coefficients convergence for figure-8 path (a) C_{Zavg} (b) C_{Xavg} . . 49

4.2 Force coefficients convergence for straight path (a) C_{Zavg} (b) C_{Xavg} . . 49

4.3 Instantaneous C_{Z}-C_{X} values of 51st cycle for straight path at (a) Sr=0 (b) Sr=10 50

4.4 Vorticity contours in percent cycle times for $Sr = 0$. The first row shows downstroke (right to left), the next upstroke (left to right) 52

4.5 Vorticity contours in percent cycle times for $Sr = 10$. The first row shows downstroke (right to left), the next upstroke (left to right) . . . 52

4.6 Z-Velocity contours in percent cycle times for $Sr = 0$. Upstroke only (left to right) 53

4.7 Z-Velocity contours in percent cycle times for $Sr = 10$. Upstroke only (left to right) 53

5.1 (a) C_{Zavg} vs α_{S} (b) C_{Xavg} vs α_{S} for different local Reynolds number values at $St = 0.1$ 56

5.2 (a) C_{Zavg} vs Re_{l} (b) C_{Xavg} vs Re_{l} for different stroke angle of attack values at $St = 0.1$ 56

5.3 (a) C_{Zavg} (b) C_{Xavg} for different α_{S} at $Re_{\text{l}} = 40$ 57

5.4 (a) C_{Zavg} (b) C_{Xavg} for different α_{S} at $Re_{\text{l}} = 100$ 58

5.5 (a) C_{Zavg} vs α_{S} (b) C_{Xavg} vs α_{S} for different local Reynolds number values at $St = 5$ 58

5.6 (a) C_{Zavg} vs Re_{l} (b) C_{Xavg} vs Re_{l} for different stroke angle of attack values at $St = 5$ 59

5.7 (a) C_{Zavg} vs α_{S} (a) C_{Xavg} vs α_{S} for different Strouhal number values at $Re_{\text{l}} = 40$ 59

5.8 (a) C_{Zavg} vs St (b) C_{Xavg} vs St for different stroke angle of attack values at $Re_{\text{l}} = 40$ 60

5.9 (a) C_{Zavg} vs α_{S} (b) C_{Xavg} vs α_{S} for different Strouhal number values at $Re_{\text{l}} = 200$ 61

5.10 (a) C_{Zavg} vs St (b) C_{Xavg} vs St for different stroke angle of attack values at $Re_{\text{l}} = 200$ 61

6.1 Micro-flyer model Reference Frames (a) body frame (b) Right stroke plane and wing frames 63

6.2 Different angles of flapping wing micro-flyer model (a) Right stroke plane yaw angle χ_{R} (b) Wing pitch angle $\theta_{\text{R,L}}$ and right stroke plane pitch angle $\theta_{\text{S}_{\text{R}}}$(c) Wing heave angles β_{R} and β_{L} (d) Wing flap angles ζ_{R} and ζ_{L} 65

6.3 (a) Micro-flyer wing divided into multiple sections (b) Semi-span and chord length defined for each section 66

6.4 Eulerian and Lagrangian frames for a micro-flyer flapping in straight path 67

6.5 Position vector $\vec{r}_{\text{R,L}}$ for calculating aerodynamic moments 68

6.6 Reference area (checkered region) to calculate micro-flyer body drag 71

6.7 Inertial positions and velocities 83

6.8 x-z position plot 84

6.9 Body velocities 84

6.10 Body pitch angle and pitch rate 85

6.11 Cycle-averaged forces and pitching moment 85
6.12 Input frequency f and stroke plane pitch angle θ_S 86
6.13 Inertial positions and velocities for steady climb 90
6.14 x-z position plot for steady climb 90
6.15 Body velocities for steady climb 91
6.16 Body pitch angle and pitch rate for steady climb 91
6.17 Cycle-averaged forces and pitching moment for steady climb 92
6.18 Input frequency f and stroke plane pitch angle θ_S for steady climb . . 92
6.19 Inertial positions and velocities for straight & level flight 93
6.20 x-z position plot for straight & level flight 93
6.21 Body velocities for straight & level flight 94
6.22 Body pitch angle and pitch rate for straight & level flight 94
6.23 Cycle-averaged forces and pitching moment for straight & level flight 95
6.24 Input frequency f and stroke plane pitch angle θ_S for straight & level flight 95
6.25 Inertial positions and velocities for combined flight maneuver 96
6.26 x-z position plot for combined flight maneuver 96
6.27 Body velocities for combined flight maneuver 97
6.28 Body pitch angle and pitch rate for combined flight maneuver 97
6.29 Cycle-averaged forces and pitching moment for combined flight maneuver 98
6.30 Input frequency f and stroke plane pitch angle θ_S for combined flight maneuver 98
6.31 Gain scheduling parameter σ 99

LIST OF TABLES

Table		Page
2.1	Smoothing parameters for dynamic mesh of micro-flyer model	15
2.2	Reference values for calculation of lift coefficient C_{L}	17
2.3	Wing and flow parameter values used for simulation	26
2.4	Parameter values for DOE	26
2.5	Estimated coefficient values for cycle-averaged force coefficients	28
3.1	Details of convergence study grids	36
3.2	Grid convergence calculations	38
3.3	Parameter values for AGARD experiment	40
3.4	Ramping motion data from AGARD experiment	42
5.1	Parameter Value Ranges for Large DOE Data-set	55
6.1	Parameter values for aerodynamic model	71
6.2	Body inertia tensor of micro-flyer model	75
6.3	Properties of micro-flyer model	76
6.4	Trim point $(\mathbf{X_e}, \mathbf{U_e})$ for steady descent	79
6.5	Trim point $(\mathbf{X_e}, \mathbf{U_e})$ for steady climb	87
6.6	Trim point $(\mathbf{X_e}, \mathbf{U_e})$ for straight & level flight	87

CHAPTER 1

INTRODUCTION

1.1 Insect Flight

Flapping motion used in insect flight is a fascinating topic of study for many researchers and biologists, due to its application in the development of biomimetic micro-flyers. Insects rely on a peculiar high frequency wing flapping mechanism to produce the aerodynamic forces required for sustainable flight. The amplitude of the frequency varies among different species and is a strong function of the body shape and size, as well as the flight mode to be achieved. Birds have high wing aspect ratio and operate at higher Reynolds number, and so can use their wings to achieve lift equal to their weight. For insects, the wing aspect ratio and Reynolds number are too low to produce enough lift. Instead, they use high frequency flapping mechanism at different flapping flapping trajectories for optimal power consumption to generate required aerodynamic forces [2–6]. Broad study of this lift mechanism is imperative to obtain a reasonably accurate representation of these forces.

A pictorial representation of an insect flapping motion is shown in Fig. 1.1. As seen in the figure, the flapping occurs in a 'stroke plane', which is the plane of symmetry for flapping. All the wing motions are described with respect to the stroke plane. An insect wing has three degrees of freedom: flapping or forward and backward motion in the stroke plane, heaving or upward and downward motion about the stroke plane, and pitching motion about the wing root. The flapping cycle is divided into two parts, a downstroke (moving forward) and an upstroke (moving backward). The insect may 'flip' the wing at the end of each stroke to maintain a constant wing

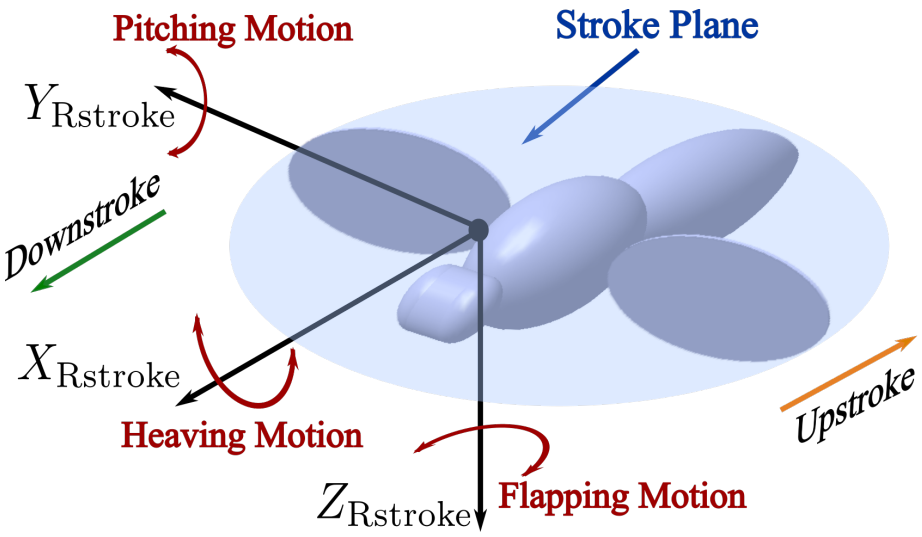

Figure 1.1. Flapping motion of an insect.

leading edge. All these wing kinematic parameters vary with different insects and for different flapping trajectories based on the requirement to perform desired flight maneuvers.

1.2 Literature Review

In most of the earlier studies, flapping flight was based on quasi-steady analysis. Ellington [7–11] used the quasi-steady aerodynamics to analyze flapping insect flight. Weis-Fogh [12] derived simple analytical expressions for average lift coefficient, Reynolds number, and aerodynamic power in insects which hover with horizontally beating wings. It was stated that unsteady aerodynamics plays an important role in very small insects at low Reynolds numbers. The three unusual phases in wing stroke were observed: the clap, the fling and the flip. The insects like *Drosophila* and butterflies use fling for creating lift and for setting up the appropriate circulation over the wing by anticipating the downstroke. In the flip mechanism a pair of counter-rotating vortices are shed and a transient circulation is set up, inducing the Wagner

effect [13]. Ellington [14] observed that unsteady aerodynamic effects like delayed stall can produce extra lift for several chords of travel during the translational phases of the wing flap. The studies revealed large leading-edge vortices which contribute to the circulation around the wing, augmenting the lift.

Researchers have often used numerical techniques to determine factors influencing the force generation in insect flight. Shyy et al. [15] offered an overview of the challenges and issues involved in using computational modeling of aerodynamic forces. Sun et al. [16] studied the lift and power requirements of hovering insect flight by solving the Navier-Stokes equations numerically. They established the lift and power dependencies on the flapping frequencies, stroke amplitude and wing length. Lee et al. [17] conducted a numerical study to investigate aerodynamic characteristics of unsteady force generation by a 2-D flapping motion under forward-flight condition. They found that found that lift is mainly generated during the downstroke of a 'figure-8' 2-D flapping motion whereas thrust is abruptly generated at the end of upstroke. Ramamurti et al. [18] verified the hypothesis presented by Dickinson et. al in their work on mechanical Drosophila wings [1] that rotational mechanisms of the wing form the basis by which the insect modulates the magnitude and direction of forces during flight. They employed a finite element flow solver to compute an unsteady flow past a 3-D Drosophila wing undergoing flapping motion. Bai et. al [19] proposed a new bionic flapping motion for Drosophila wing using CFD techniques. They justified the correctness of their numerical method and the computational program by comparing their CFD results of the Drosophila flapping motion in three modes, i.e., the advanced mode, the symmetrical mode and the delayed mode, with experimental results presented by Dickinson et al. [1]. Tang et al. in [20] Navier-Stokes equations for fluid flow around a hovering elliptic airfoil to investigate the effects of Reynolds number, reduced frequency and flapping kinematics on the flow structure and aerodynamics.

Platzer et al. in [21] found that thrust and lift are strongly dependent on flapping frequency, amplitude and Reynolds number and that thrust is a function of Strouhal number.

1.2.1 Aerodynamic Models used in Flight Dynamics

Taha et al. [22] provided an exhaustive summary of the different aerodynamic models used within the flight dynamics framework. They observed that most of these aerodynamic models are experimentally based. The models may be classified as steady or unsteady. There are very few unsteady aerodynamic models proposed based on Fourier series [23, 24], since these models may not be applicable to certain wing configurations. Most of the models in the literature follow a quasi-steady approach.

Hedrick and Daniel [25] used a revised quasi-steady model by Sane and Dickinson [26] to solve an inverse problem of finding the range of wing movements needed for sustained hovering flight. Traub [27] used geometric and kinematic data to derive cycle-averaged expression for lift for hover. Berman and Wang [28] used the model of Andersen et al. [29] to obtain optimal wing kinematics in hovering insect flight by minimizing power consumption while constraining the lift to maintain the flight altitude of insect. Orlowski et al. [30] adopted this model to develop a nonlinear flight dynamics model that included wing inertial effects. Khan and Agarwal [31] developed an aerodynamic model for a translatory flapping and pitching wing. They considered translational, rotational and added mass effects, but neglected viscous effects. Ansari et al. [32] in their model decomposed translational and rotational effects, but did not include downwash and tip vortices.

Major portion of the flight dynamic literature [33–42] uses the quasi-steady model provided by Dickinson et al. [1]. In their experiments, Dickinson et al. rapidly accelerated the wing from rest to a constant tip velocity at different angles of attack.

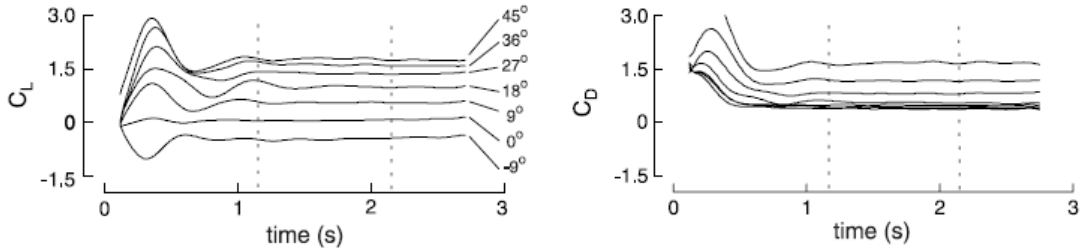

Figure 1.2. Time history of lift (C_{L}) and drag (C_{D}) coefficients for 7 angle of attack values, taken from Dickinson et al. [1]. The dotted lines indicate the interval over which values are averaged.

They recorded the time histories of lift and drag coefficients at each angle of attack. The lift and drag coefficient values were averaged over an interval where the force trajectories were constant throughout the translation, after an initial large transition caused by the rapid acceleration of wing at the start, as shown in Fig. 1.2. These mean values calculated at every angle of attack were then used in a curve fit to compute the translational force coefficients given by

$$\begin{aligned} C_{\mathrm{L}} &= 0.225 + 1.58\sin(2.13\alpha - 7.20) \\ C_{\mathrm{D}} &= 1.92 - 1.55\cos(2.04\alpha - 9.82) \end{aligned} \tag{1.1}$$

where α is the wing angle of attack in degrees. The limitations of this model however are the fact that the expressions are valid only for translational motion. Some modifications were made to this model by adding rotational lift and viscous and added mass effects [29, 43]. Moreover, the experiments were done at hovering conditions. So these expressions cannot be used in cases where forward flight is to be simulated.

1.3 Research Objectives and Contributions

1.3.1 Objectives

Most of the previous work on flapping wing aerodynamics focused mainly on identifying and studying the impact of different parameters on force production. In this work, the effects of these parameters will be quantified. An aerodynamic model comprising these parameters will be developed and used in the nonlinear flight dynamics framework to simulate different insect flight modes, that will enable the designer to size various MAV components that are a required to perform different flight maneuvers. Specifically, this research is being carried out to address the following questions:

I. Are there any optimum values of the parameters that govern the force production in insect flapping flight to get desirable forces?

II. Can we develop an aerodynamic model which will represent the aerodynamics involved in insect flapping flight, and can be used in the nonlinear flight dynamics framework?

III. Using this nonlinear dynamics framework, can we predict if a micro-flyer can achieve a desired maneuver, if its geometry, flapping amplitude and flap frequency are provided?

1.3.2 Secondary Objectives

IV. Perform parametric study of wing flapping trajectories.

V. Study the influence of nondimensional parameters on the force production by wing flapping.

VI. Develop a control architecture to perform closed loop simulations of a Micro-flyer for a desired trajectory.

1.3.3 Original Research Contributions

(i) Quantifying the dependence of aerodynamic forces in flapping wing flight on Reynolds number, Strouhal number, stroke angle of attack.

(ii) Developing a generic aerodynamic model to accommodate characteristics of different insects.

(iii) Proposing a nonlinear dynamics framework as a test-bed to develop insect based flapping micro-flyers.

1.3.4 List of Published Works

(a) Objectives I.,IV.:

Rege A., Dennis B., and Subbarao K., "Parametric Study on Wing Flapping Path of a Micro Air Vehicle using Computational Techniques", AIAA 2013–953, 51st AIAA Aerospace Sciences Meeting Including the New Horizons Forum and Aerospace Exposition, Grapevine, TX 2013. [44].

(b) Objectives I.,V.:

Rege A., Dennis B., and Subbarao K., "Sensitivity Analysis of the Factors Affecting Force Generation By Wing Flapping Motion", ASME 2013 IMECE, San Diego, CA. [45].

(c) Objectives I.,II.:

Rege A., Subbarao K., and Dennis B., "Nonlinear Dynamics of Flapping Wing MAV using Cycle-Averaged Force Coefficients", AIAA 2014-0895, AIAA Atmospheric Flight Mechanics Conference, AIAA SciTech 2014, National Harbor, MD. [46].

(d) Objectives I.,VI.:

Rege A., Dennis B., and Subbarao K., "Force Production by Wing Flapping:

The Role of Stroke Angle of Attack and Local Reynolds Number", 33rd AIAA Applied Aerodynamics Conference, Aviation 2015, June 2015, Dallas, TX.

1.4 Dissertation Organization

The organization of the chapters is as follows. Chapter 2 describes the methodology adopted to perform CFD analysis to develop an aerodynamic model. The methodology consists of two parts. In the first part, parametric study of flapping trajectories is conducted to identify parameters that influence force generation. In the second part, the identified parameters are non-dimensionalized. A sensitivity analysis is performed by conducting a design of experiments (DOE) using full factorial method to find parameter values that produce thrust and lift. A method is described to develop an aerodynamic model comprising cycle-average expressions for horizontal and vertical force coefficients for straight flapping trajectory. The entire analysis is done using an unstructured grid.

In chapter 3, results of convergence and validation study for a hybrid structured grid are presented. The grid is developed to perform the CFD analysis. Results of the parametric study using the structured grid are presented in chapter 4. Chapter 5 presents the sensitivity analysis results for a large DOE data-set, describing the influence of the non-dimensional parameters on the horizontal and vertical forces.

Chapter 6 describes a nonlinear flight dynamics framework for a flapping wing micro-flyer. Flight dynamics model is derived from first principles. An aerodynamic model developed on the lines of the method described in chapter 2 is used in the framework. Linear analysis is conducted to study steady-state flight conditions of the micro-flyer model with different material properties. Open loop and closed loop simulations are performed to achieve the desired steady-state maneuver. Chapter 7 gives a summary of the work presented and the future direction of the research.

CHAPTER 2

PROPOSED METHODOLOGY AND PRELIMINARY STUDY

A study is conducted to identify and study the effect of parameters [47] that affect the force generation due to wing flapping. This work is essentially done to facilitate the development of an effective aerodynamic model which is a function of all the force producing parameters. The preliminary results are obtained by performing the study using an unstructured grid over a 2-dimensional wing section of a micro-flyer. The methodology adopted is two-fold. First, a parametric study of flapping paths is done to identify the force influencing parameters. Then these parameters are non-dimensionalized and used in a design of experiments (DOE) to perform a sensitivity analysis.

2.1 Parametric Study of Flapping Paths

A parametric study of flapping trajectories made by 2-D wing section of the micro-flyer is presented. The procedure adopted for this study is as shown in the flow chart given in Fig. 2.1.

The following sections explain in detail the various steps taken to perform the parametric study of the different flapping paths.

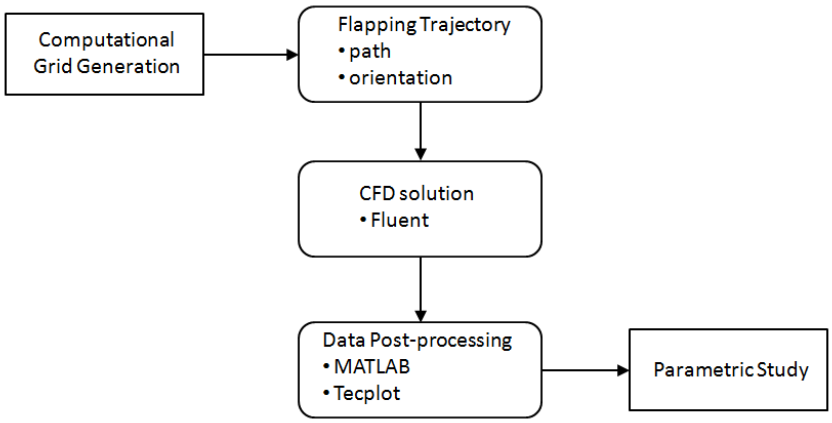

Figure 2.1. Flow chart for CFD analysis.

2.1.1 Computational Grid

The 2-D wing section of the flapping wing micro-flyer is modeled as a thin flat plate of length 1 unit and thickness 0.01 units[1]. The two edges of the model are blunted to avoid flow detachment. The model is placed with its center coinciding with the origin of the workspace coordinate system, as shown in Fig. 2.2. 100 nodes are created on each side of the model, while each of the edges had 5 nodes for cell connectivity. For this preliminary study, unstructured grid generation is preferred over structured, since unstructured grids reduce the overall complexity of the grid generation process. However, it is important to monitor the unstructured mesh schemes to check if there are high aspect ratio cells, since they add to the errors in the results. An O-type grid with a diameter of 15 times the model length and a total of 100 nodes on the outer boundary connector is created. A boundary decay factor of 0.99 is used to get refined mesh as seen in Fig. 2.3. No high aspect ratio cells are found in the generated grid.

[1]Pointwise®, a commercially available grid genetation software was utilized to generate the computational grid

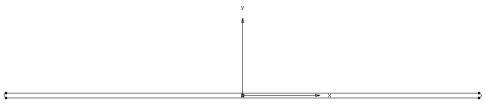

Figure 2.2. Model of a wing section used for CFD analysis.

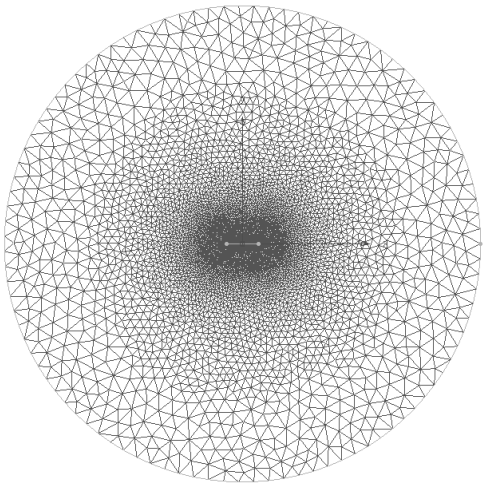

Figure 2.3. Computational domain large and refined mesh.

2.1.2 Flapping Trajectories

Insects rely on different flapping trajectories to produce the required aerodynamic forces, in order to maintain their position in case of hover, or to propel themselves to a new position, [48]. Broad study of this mechanism for producing forces is imperative to determine the required aerodynamic expressions accurately. In the previous work (Ref. [47]) four trajectories were used for the parametric study. This dissertation focuses on two such trajectories; a figure-8 path as shown in Fig. 2.4, and straight path as shown in Fig. 2.5.

As seen in Fig. 2.4(a), the circle and the diamond show the start and the direction of the wing stroke respectively. Figure 2.4(b) shows the instantaneous wing positions during the two half strokes; the downstroke or the forward flapping motion of the wing, and the upstroke or the backward flapping motion. The circular head on the wing depicts the wing leading edge. All the paths are generated using parametric

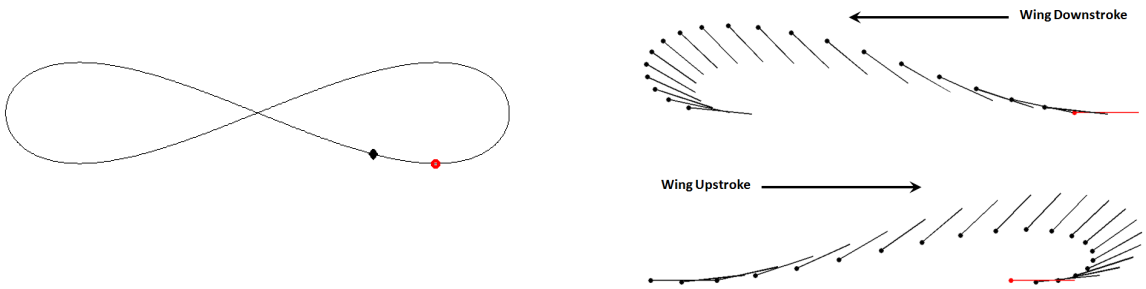

(a) (b)

Figure 2.4. Figure-8 flapping path, (a) Flapping direction and (b) Instantaneous wing flapping positions.

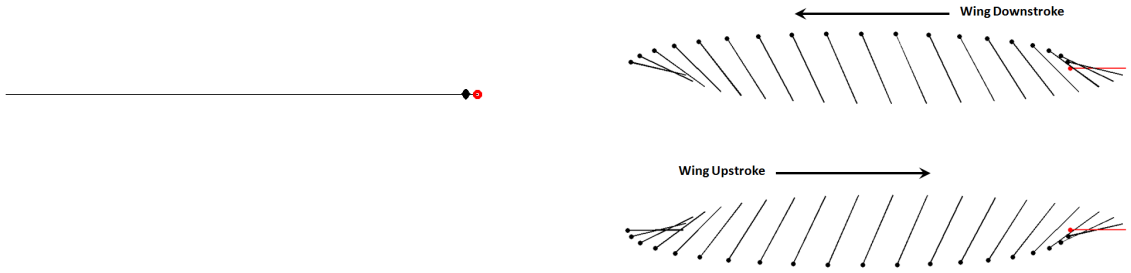

(a) (b)

Figure 2.5. Straight flapping path, (a) Flapping direction and (b) Instantaneous wing flapping positions.

functions. For uniformity, the stroke lengths for all the trajectories are kept same. The kinematics of the figure-8 flapping path is given by

$$\begin{aligned} x(t) &= A\cos(2\pi ft + \phi) \\ y(t) &= 0.2A\sin(2\pi ft + \phi) \\ \theta(t) &= sin(2\pi ft) \end{aligned} \tag{2.1}$$

while the kinematics of the straight flapping path is given by

$$\begin{aligned} x(t) &= A\cos(2\pi ft) \\ y(t) &= 0 \\ \theta(t) &= sin(2\pi ft) \end{aligned} \tag{2.2}$$

In both the cases, A is the wing flapping amplitude, set at a value of 0.004. The coordinates (x, y) give the position of the wing center, and angle θ gives the wing orientation with respect to the x-axis. The flapping frequency f is set at 100 Hz. For figure-8 path, the flapping starts with a phase shift of $\phi = \pi/4$.

2.1.3 Computational Flow Solver

The commercial CFD solver ANSYS-Fluent is used to solve the unsteady incompressible Navier-Stokes equations on an unstructured triangular mesh described earlier. For incompressible flows, this essentially means solving the momentum equation given by

$$\frac{\partial \vec{V}}{\partial \mathrm{t}} + \vec{V}.\nabla\vec{V} = -\frac{1}{\rho}\nabla p + \nu\nabla.(\nabla\vec{V}) \tag{2.3}$$

along with the continuity equation given by

$$\nabla.\vec{V} = 0, \tag{2.4}$$

where $\vec{V}$ is the velocity vector of the fluid element, ρ is the fluid density, p is the pressure acting on the fluid element, and ν is the kinematic viscosity of the fluid. A pressure-based implicit finite volume method is used. 'Coupled' scheme along with standard '2nd-order upwinding differencing method' is chosen to run all simulations. The coupled scheme implementation is necessary for transient flows to get accurate results. The coupled algorithm solves the momentum and pressure-based continuity equation together. The full implicit coupling is achieved through an implicit dis-

cretization of pressure gradient terms in the momentum equations, and an implicit discretization of the face mass flux, including the pressure dissipation terms.

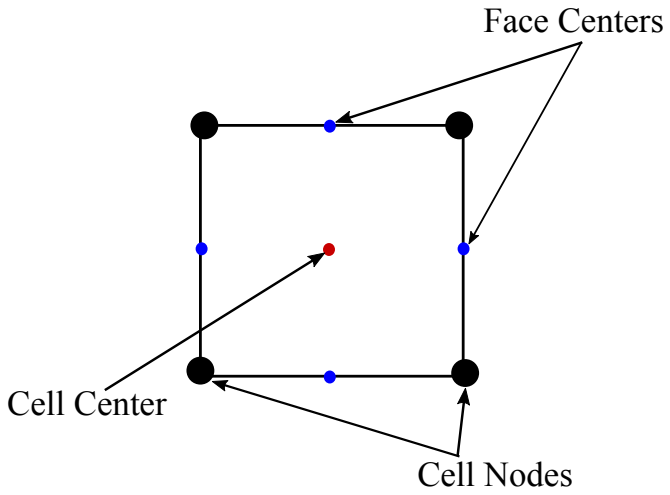

Figure 2.6. Pictorial representation of a grid cell.

When using the second order upwinding discretization scheme, the value of the scalar at the cell face ϕ_f is computed as

$$\phi_f = \phi + \nabla\phi.\vec{r} \tag{2.5}$$

where ϕ and $\nabla\phi$ are the cell-centered value and its gradient in the upstream cell respectively, and $\vec{r}$ is the displacement vector from the upstream cell centroid to the face centroid. This formulation requires the determination of the gradient in each cell. Hence, a 'Green-Gauss' cell-based gradient method is used to compute the gradient of the scalar at the cell faces and also for computing the secondary diffusion terms and velocity derivatives. The cell-center approach deals with less points over the

domain as it stores the solution at each cell-center thereby taking less memory than the node-center approach. The discrete form of this method is written as

$$(\nabla\phi)_{c_0} = \frac{1}{\nu}\sum_f \bar{\phi}_f \vec{A}_f, \tag{2.6}$$

where $\bar{\phi}_f$ is the value of the scalar ϕ at the cell face centroid c_0. The summation is over all the faces enclosing the cell. The face value, $\bar{\phi}_f$, is taken from the arithmetic average of the values at the neighboring cell centers,i.e.,

$$\bar{\phi}_f = \frac{\phi_{c_0} + \phi_{c_1}}{2} \tag{2.7}$$

A moving mesh scheme is used to maintain a boundary conforming grid despite the large relative motion of the airfoil with respect to the fixed outer boundary. The wing motion is also large relative to the mesh size so dynamic smoothing and local remeshing schemes are employed at each time step to maintain a high quality mesh. For the remeshing method, the maximum length and maximum cell skewness are set to 0.0001 m and 0.6 respectively, while a size remesh interval of 5 was used. The details of smoothing parameters are given in Tab. 2.1. Fig 2.7 shows an example of a moving mesh about the wing section with smoothing and remeshing employed.
Ueno et al. [49] observed in their preliminary experiments that 1000 time steps per

Table 2.1. Smoothing parameters for dynamic mesh of micro-flyer model

Property	Value
Spring Constant Factor	0.1
Boundary Node Relaxation	0.1
Convergence Tolerance	0.001
Number of Iterations	20

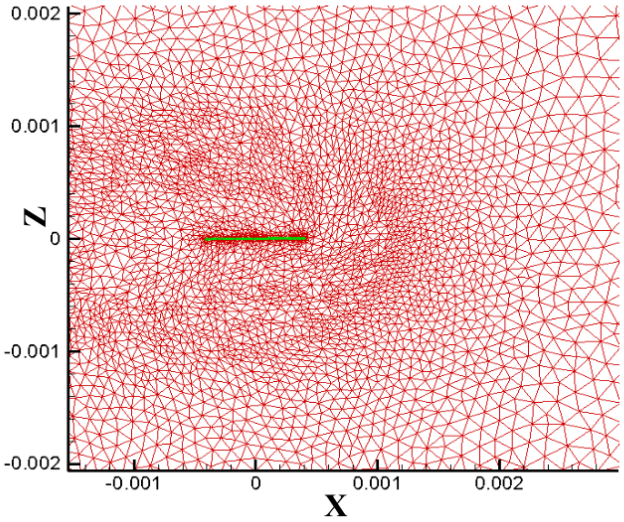

Figure 2.7. Unstructured mesh around the wing section with smoothing and remeshing employed.

cycle resulted in stable computation for all generated designs. The time step size for simulation is given as

$$\mathrm{d}t = \frac{\text{total flapping period}}{1000} = \frac{0.01}{1000} = 1{\times}10^{-5} \tag{2.8}$$

The unsteady lift produced by the wing section is computed by integrating the time-variant static pressure over the wing section during one cyclic motion. The reference values for calculation of lift coefficient C_{L} is given in Tab. 2.2. The wing section is set at a no-slip wall boundary condition with the user-defined motion. Experiments are run for 51 flap cycles. For the parametric study, the outer boundary conditions of the computational domain are varied as 'velocity inlets' of 0.01, 0.1, 1, 3, and 5 m/s in x-direction; and in the other case, the outer boundary itself is made double of the original boundary while keeping the boundary condition as a 'velocity inlet' of 0.01 m/s in x-direction.

Table 2.2. Reference values for calculation of lift coefficient C_{L}

Property	Value
Area, S	1 m^2
Density, ρ	1.225 $\mathrm{kg/m}^3$
Velocity, V_∞	1 m/s
Viscosity, μ	1.7894×10^{-5} kg/m-s

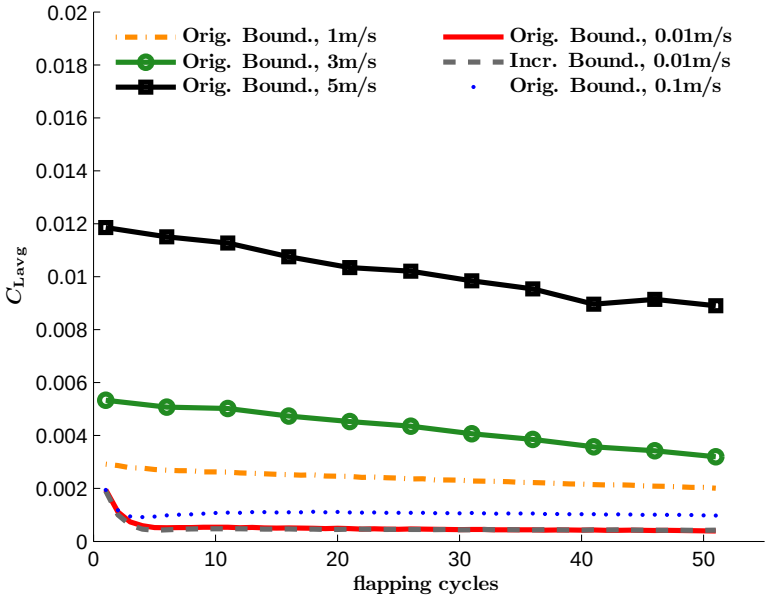

Figure 2.8. C_{Lavg} convergence plot for figure-8 path.

2.1.4 Results

User-defined functions are used to initialize the solutions for the unstructured moving mesh. A function is created to define a wing section path that would generate the input to flow solver for the mesh movement. An initialization file is created that would save the data history of the coefficients of lift for the entire solver runtime, as well as saving the ANSYS-Fluent case and data files every 50 time steps. C_{L} data history is then imported to MATLAB, while the ANSYS-Fluent data and case files are imported to Tecplot for data analysis.

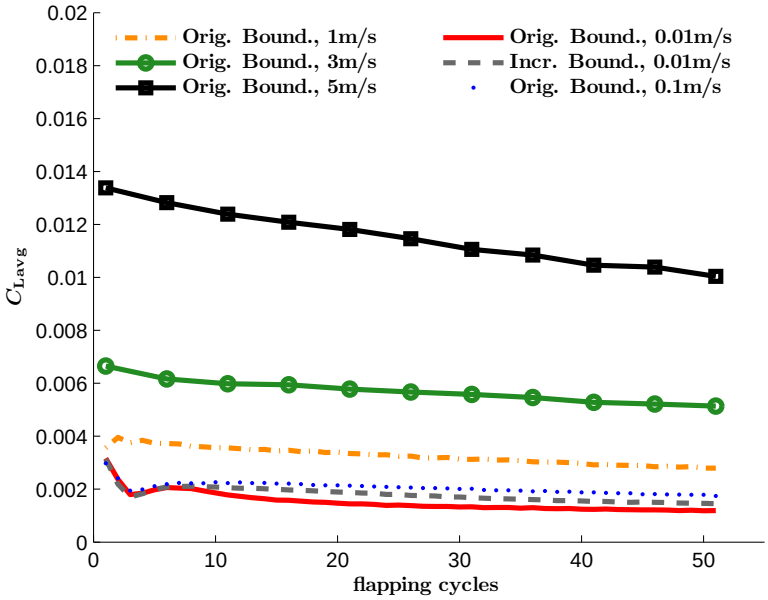

Figure 2.9. C_{Lavg} convergence plot for straight path.

The entire data history is imported to MATLAB for all the cases and the C_{L} values are averaged and plotted over each cycle to study the convergence of average lift coefficient over flapping cycles. Fig. 2.8 shows the C_{Lavg} convergence plot for different cases of the figure-8 path. As seen from the figure, increasing the outer boundary has no considerable effect on the C_{Lavg} value. When the inlet velocity is changed to 0.1 m/s, C_{Lavg} converges to a higher value of 0.001, while it reaches the highest value of 0.009 at the inlet velocity of 5 m/s. For the straight path, as shown in Fig. 2.9, increased outer boundary gives a slightly larger C_{Lavg} value of 0.0015 as compared to the original outer boundary value of 0.0012. Increasing the inlet velocity has a similar impact on the C_{Lavg} values as in the previous case, with the highest value of 0.01 obtained at 5 m/s.

Velocity vector fields are plotted for all the simulation cases. Figures 2.10 and 2.11 show the velocity vector plots for the figure-8 and straight line trajectories

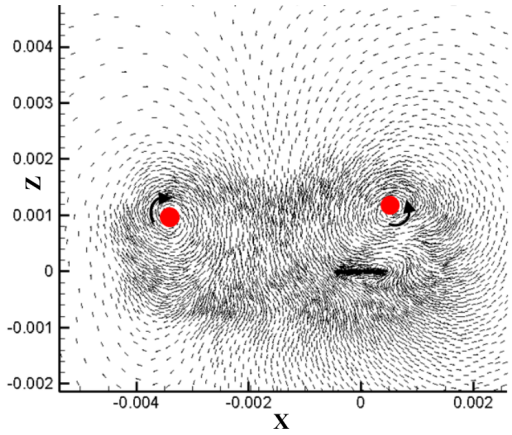

Figure 2.10. Velocity vector plot for figure-8 path (Inlet Velocity = 0.01 m/s, Original Outer Boundary).

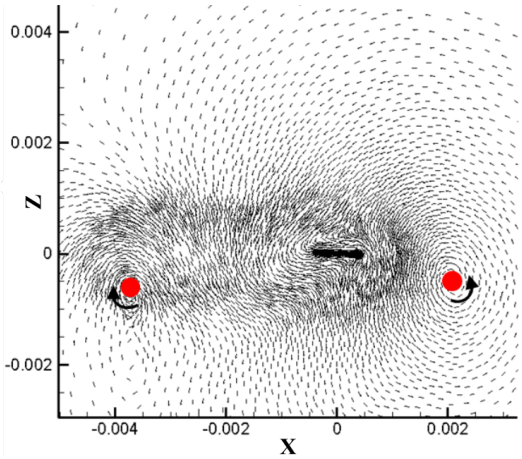

Figure 2.11. Velocity vector plot for straight line path (Inlet Velocity = 0.01 m/s, Original Outer Boundary).

respectively for the inlet velocity of 0.01 m/s for the 51st cycle with original grid size. It can be seen from the figures that there are two counter-rotating vortices set up in the flow. The red solid circle in the figures shows the origin of the vortex while the curved arrows show the direction of vortex rotation.

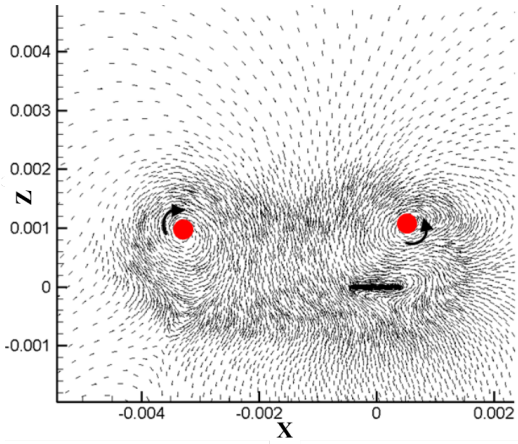

Figure 2.12. Velocity vector plot for figure-8 path (Inlet Velocity = 0.01 m/s, Increased Outer Boundary).

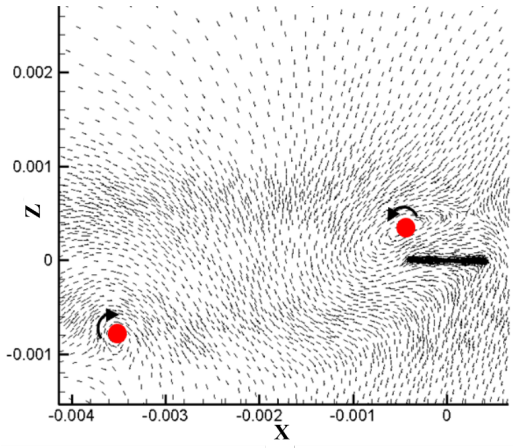

Figure 2.13. Velocity vector plot for straight line path (Inlet Velocity = 0.01 m/s, Increased Outer Boundary).

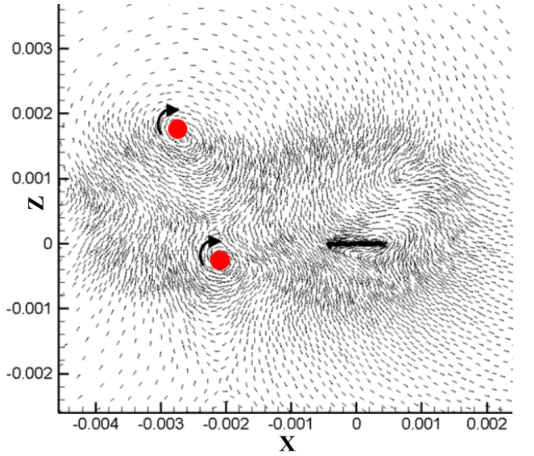

Figure 2.14. Velocity vector plot for figure-8 path (Inlet Velocity = 0.1 m/s, Original Outer Boundary).

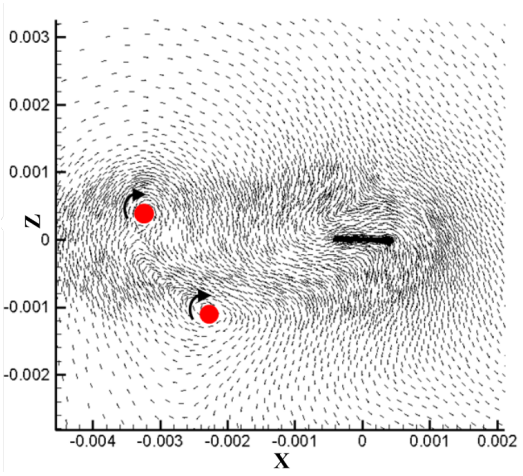

Figure 2.15. Velocity vector plot for straight line path (Inlet Velocity = 0.1 m/s, Original Outer Boundary).

These standing vortices are a result of continuous wing flapping after 51 cycles. Since the wing is flapping continuously in a bounded region, the air around it is nearly stagnant though the wing motion creates a vortex pattern in the flow. The viscous effects in the flow are not high enough to dampen the vortices to extinction after each cycle, rather the continuous flapping motion provides energy input to the flow to maintain the vortex rotation. Furthermore, the low inlet air velocity of 0.01 m/s is not able to transport the vortices downstream and away from the wing.

However, the locations of vortices for each path is different. This explains the different lift coefficient values for the two trajectories. It can be seen from Fig. 2.10 that both the vortices are located above the wing location, which create a downwash on the wing thereby reducing the net lift; while Fig. 2.11 shows that the vortex locations in this case are below the wing location, which have an upwash effect on the wing thereby increasing the net lift. This observation corroborates the results obtained for the C_{Lavg} values at inlet velocity of 0.01 m/s, with the straight line path giving a higher value than the figure-8 path.

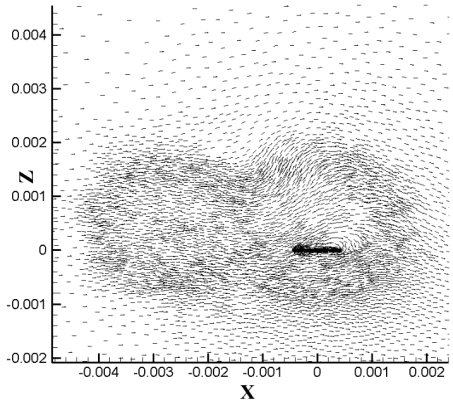

Figure 2.16. Velocity vector plot for figure-8 path (Inlet Velocity = 1 m/s, Original Outer Boundary).

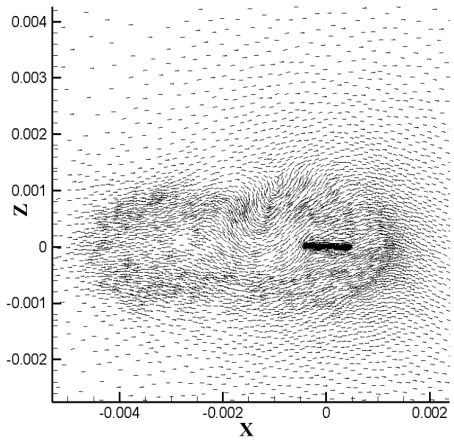

Figure 2.17. Velocity vector plot for straight line path (Inlet Velocity = 1 m/s, Original Outer Boundary).

Figures 2.12 and 2.13 show the velocity vector plots for the figure-8 and straight line trajectories respectively with the same inlet velocity but with increased grid size. As seen from the plots, the figure-8 path shows no considerable change in the flow field, while in the case of straight line path, there is only one standing vortex in the flow field. This falls in line with the C_{Lavg} values obtained for the respective cases. Similarly, from figures 2.14 and 2.15 for the inlet air velocity of 0.1 m/s, it can be seen that the vortex locations for both the cases have changed thereby affecting the C_{Lavg} values. It is to be noted however that the inlet velocity is still not high enough to blow the vortices away from the wing.

Figures 2.16 and 2.17 show the velocity vector plots for the figure-8 and straight line trajectories respectively for the inlet velocity of 1 m/s. It can be clearly seen from the plots that there are no standing vortices in the flow field of the flapping wing, which suggests that the inlet velocity is high enough the push the vortices downstream and away from the wing. This boundary condition consequently gives higher values

of average lift coefficient for both trajectories. The same observation holds true for the cases with inlet velocities of 3 and 5 m/s.

An important factor that affects the C_{Lavg} values in all the above cases is the time history of the flapping motion. As seen from the C_{Lavg} plots for both the trajectories, the values are changing after every flapping cycle. One possible explanation could be that due to the buildup of kinetic energy in the surrounding air because of the continual stirring-like motion of the airfoil. Thus flow field around the wing is altered after every flap. Since this flow field is a result of a number of flaps over a period of time, it is essential that the time history of flapping is considered while developing the new aerodynamic expressions. Therefore, for a stationary micro-flyer with flapping wings, the aerodynamic expressions should include the time history of flapping.

2.2 Sensitivity Analysis using Non-Dimensional Parameters

This section deals with conducting a sensitivity analysis of the factors that influence force generation in a wing flapping mechanism. Firstly, non-dimensional parameters are defined that incorporate these factors and a full factorial design of experiments is conducted and response surface methodology is used over a small dataset to approximate the expressions for average force coefficients. These expressions are then verified over the region of parameter limits to observe the relationships of parameters and the average force coefficients.

2.2.1 Non-Dimensional Parameters

Sensitivity analysis is performed on the non-dimensional parameters that include the factors influencing the force production. Observations from the parametric study presented earlier suggested that the average force coefficient values depend

on the free stream velocity as well as the velocity generated due to wing flapping. These velocities are incorporated by defining two non-dimensional parameters, the free stream Reynolds number and the local Reynolds number. The free stream Reynolds number is given by

$$Re_\infty = \frac{\rho V_\infty c}{\mu}, \tag{2.9}$$

where ρ is the density of air, V_∞ is the free stream air velocity, c is the micro-flyer wing chord which is taken as the reference length, and μ is the dynamic viscosity of air. The local Reynolds number is given by

$$Re_\mathrm{l} = \frac{\rho V_\mathrm{l} c}{\mu}, \tag{2.10}$$

where V_l is the local velocity due to wing flapping and is given by

$$V_\mathrm{l} = fL \tag{2.11}$$

where f is the wing flapping frequency and L is the wing semi-span. The Strouhal number is defined as the ratio of local and free stream Reynolds numbers. It is given by

$$St = \frac{Re_\mathrm{l}}{Re_\infty} = \frac{fL}{V_\infty} \tag{2.12}$$

This parameter gives the direct relation between the local and the free stream velocities. Fig. 2.18 shows the stroke angle of attack α_S, which is defined as the angle made by the wing stroke plane with respect to the free stream velocity vector.

Straight path is chosen as the flapping path for the sensitivity analysis. The orientation of the path is fixed parallel to the body X-axis. As shown in Fig. 2.19, each wing chord along the wing span will traverse a certain maximum path distance based on the geometry of the wing. To accommodate this geometric constraint of the wing, a geometric function G is defined as one of the parameters and is given by

$$G = \frac{c}{L}, \tag{2.13}$$

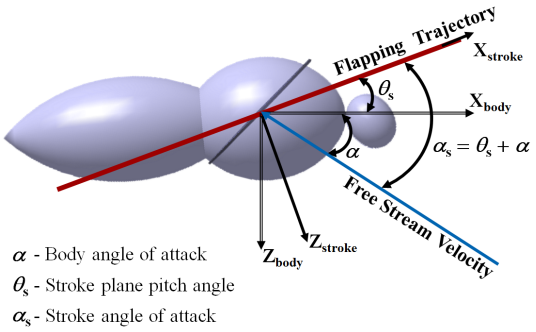

Figure 2.18. Stroke angle of attack α_S.

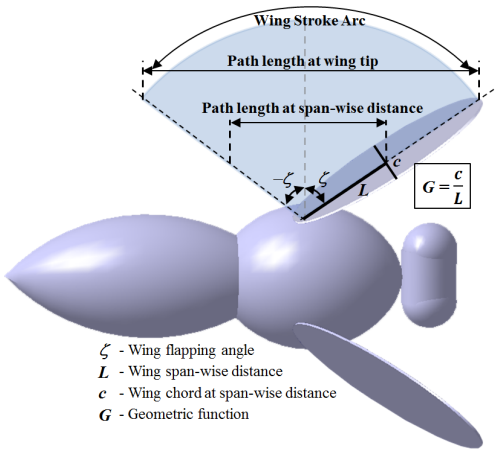

Figure 2.19. Variation of wing path length over span.

The parameters St, Re_l, G, and α_S represent the independent non-dimensional parameters that influence force production for a given airfoil geometry and path. The dependent horizontal and vertical forces are also non-dimensionalized as shown below. These forces are considered positive in the drag and upward lift directions respectively. This means that to obtain thrust, horizontal force should be negative. The independent parameters are then used in the design of experiments (DOE) to perform the force coefficient sensitivity analysis.

$$C_X = \frac{F_X}{0.5\rho(fL)^2c}, \qquad C_Z = \frac{F_Z}{0.5\rho(fL)^2c} \tag{2.14}$$

2.2.2 Design of Experiments

It is understood that the force generation by wing flapping depends on a number of factors. To sense the combined or individual effect of these factors a design of experiments is carried out. A full factorial design method with two intervals per factor is adopted to conduct response surface methodology. The local Reynolds number, Strouhal number and the absolute angle of attack are chosen as the parameters for

the design analysis, while the geometric function G is fixed at a constant value of 0.4 for the entire set of experiments. Since the number of parameters involved is 3, the full factorial design would be

$$3^k = 3 \times 3 \times 3 = 27.$$

So a total 27 simulation runs are needed to conduct a full factorial design for the given parameters. For the simulations, a pressure-based finite volume method is used to solve the unsteady incompressible Navier-Stokes equations on an unstructured moving mesh using ANSYS-Fluent as described earlier. Pressure-velocity coupled scheme along with standard 2nd-order upwinding differencing method is chosen to run all the simulations. A moving mesh scheme is used to maintain a boundary conforming grid. Dynamic mesh smoothing is employed using diffusion method. The diffusivity is defined as a function of boundary distance and the parameter is kept at 2. User-defined functions are used to initialize the simulation runs and to control the motion of the airfoil as a function of time. The grid and the boundary conditions are parametrized in terms of the chord length c, the flapping frequency f, the wing semi-span L, the free stream velocity V_∞ and the stroke angle of attack α_{S}. The wing section is set at a no-slip wall condition. The simulations are run for 5 flapping cycles with 1000 time steps per cycle. The unsteady forces produced by the wing section are computed by integrating the time-variant static pressure over the wing section to produce instantaneous force coefficients. The reference values used for calculating the corresponding horizontal and vertical force coefficients C_{X} and C_{Z} respectively are parametrized similar to the boundary conditions. These force coefficients are then further integrated over the 5th cycle to produce the cycle-averaged force coefficients.

Table 2.3. Wing and flow parameter values used for simulation

Parameter	Value
Wing chord length, c	0.0012 m
Wing semi-span, L	0.003 m
Wing flapping frequency, f	100 Hz
Density, ρ	1.225 kg/m^3
Viscosity, μ	1.7894$\times 10^{-5}$ kg/m-s

The values of wing and flow parameters used for the simulation are given in Tab. 2.3. For the full factorial design, the maximum and minimum values of the local Reynolds number and Strouhal number are calculated based on these values. The values for all the three non-dimensional parameters used in the design of experiments are given in Tab. 2.4.

A quadratic polynomial graduating function is used as a response function to approximate both the average horizontal and vertical force coefficient values. This function is of the form

$$(C_{\mathrm{Zavg}}, C_{\mathrm{Xavg}}) = \mathrm{f}\left(Re_{\mathrm{l}}, St, \alpha_{\mathrm{S}}, Re_{\mathrm{l}}^2, St^2, \alpha_{\mathrm{S}}^2, Re_{\mathrm{l}}St, Re_{\mathrm{l}}\alpha_{\mathrm{S}}, St\alpha_S\right) \tag{2.15}$$

The method of least squares minimization is used to estimate the coefficients of the approximation function that gives the best fit through the data. The least squares problem for each force coefficient is formulated as given in [**?**].

$$\tilde{\mathbf{y}} = \mathbf{H}\hat{\mathbf{x}} + \mathbf{e}, \tag{2.16}$$

Table 2.4. Parameter values for DOE

Parameter	Re_{l}	St	α_{S} (deg)
maximum	31.88	28.5	5
mean	16.48	14.25	0
minimum	1.07	0.003	-5

where

$$\tilde{\mathbf{y}} = [\tilde{\mathbf{y}}_{\mathbf{1}},\ \tilde{\mathbf{y}}_{\mathbf{2}},\ \ldots\ \tilde{\mathbf{y}}_{\mathbf{27}}]^{\mathrm{T}} = measured\ y - values$$

$$\mathbf{e} = [\mathbf{e}_1,\ \mathbf{e}_2,\ \ldots\ \mathbf{e}_{27}]^{\mathrm{T}} = residual\ errors$$

$$\hat{\mathbf{x}} = [\hat{\mathbf{x}}_{\mathbf{1}},\ \hat{\mathbf{x}}_{\mathbf{2}},\ \ldots\ \hat{\mathbf{x}}_{\mathbf{10}}]^{\mathrm{T}} = estimated\ x - values$$

$$\mathbf{H} = \begin{bmatrix} 1 & (Re_{\mathrm{l}})_1 & (St)_1 & (\alpha_{\mathrm{S}})_1 & (Re_{\mathrm{l}}^2)_1 & \ldots & (St\alpha_{\mathrm{S}})_1 \\ 1 & (Re_{\mathrm{l}})_2 & (St)_2 & (\alpha_{\mathrm{S}})_2 & (Re_{\mathrm{l}}^2)_2 & \ldots & (St\alpha_{\mathrm{S}})_2 \\ \vdots & \vdots & \vdots & \vdots & \vdots & \ddots & \vdots \\ 1 & (Re_{\mathrm{l}})_{27} & (St)_{27} & (\alpha_{\mathrm{S}})_{27} & (Re_{\mathrm{l}}^2)_{27} & \ldots & (St\alpha_{\mathrm{S}})_{27} \end{bmatrix}$$

The method of least squares solution is the optimum value of the unknown parameters vector $\hat{\mathbf{x}}$ that minimizes the sum of the squares of the residual errors, given by

$$J = \frac{1}{2}\mathbf{e}^{\mathrm{T}}\mathbf{e} \tag{2.17}$$

From the above condition, the explicit solution for the optimal estimate is given by

$$\hat{\mathbf{x}} = \left(\mathbf{H}^{\mathrm{T}}\mathbf{H}\right)^{-1}\mathbf{H}^{\mathrm{T}}\tilde{\mathbf{y}} \tag{2.18}$$

The $\mathbf{QR}$ decomposition is used to factor the full rank matrix $\mathbf{H}$ as the product of an orthogonal matrix $\mathbf{Q}$ and an upper-triangular matrix $\mathbf{R}$, given by

$$\mathbf{H} = \mathbf{QR}, \tag{2.19}$$

where $\mathbf{Q}$ is an $m \times n$ matrix with $\mathbf{Q}^{\mathrm{T}}\mathbf{Q} = \mathbf{I}$, and $\mathbf{R}$ is an upper triangular $n \times n$ matrix with all elements $\mathbf{R_{ij}} = 0$ for $\mathbf{i} > \mathbf{j}$. In this case, $m = 27, n = 10$. Therefore, eq. (2.18) simplifies to

$$\hat{\mathbf{x}} = \mathbf{R}^{-1}\mathbf{Q}^{\mathrm{T}}\tilde{\mathbf{y}} \tag{2.20}$$

Table 2.5. Estimated coefficient values for cycle-averaged force coefficients

Basis function	C_{Zavg}	C_{Xavg}
1	-247.4274	7289.5
Re_{l}	0.121	-0.054
St	27.941	-7672.3
α_{S}	3.454	-0.06
${Re_{\mathrm{l}}}^2$	0	0
St^2	-0.654	179.46
α_{S}^2	0.241	-0.353
$Re_{\mathrm{l}}St$	0	0
$Re_{\mathrm{l}}\alpha_{\mathrm{S}}$	-0.0242	0
$St\alpha_{\mathrm{S}}$	-0.1193	0

To normalize the variance in the values C_{Zavg} and C_{Xavg} data, both sides of the eq. (2.18) are multiplied by a scaling matrix $\mathbf{W}$, which is given by

$$\mathbf{W} = \mathrm{diag}[\tilde{\mathbf{y}}_{\mathbf{1}},\ \tilde{\mathbf{y}}_{\mathbf{2}},\ \ldots\ \tilde{\mathbf{y}}_{\mathbf{27}}] \tag{2.21}$$

So eq. (2.18) becomes

$$\hat{\mathbf{x}} = \left(\mathbf{H}_{\mathbf{W}}^{\mathrm{T}}\mathbf{H}_{\mathbf{W}}\right)^{-1}\mathbf{H}_{\mathbf{W}}^{\mathrm{T}}\tilde{\mathbf{y}}_{\mathbf{W}} \tag{2.22}$$

The two decomposition methods discussed above were now applied to eq (2.22). The results of the least squares solution for the vertical and horizontal force coefficients are summarized in Tab. 2.5.In order to make the approximated functions for each of the force coefficients concise, some of the basis functions which have little or no influence on the force coefficient values as compared to other basis functions are dropped. The truncated cycle-averaged vertical force coefficient is found to be

$$\begin{aligned} C_{\mathrm{Zavg}} = &-247.4274 + 0.121Re_{\mathrm{l}} + 27.941St + 3.454\alpha_{\mathrm{S}} + 0.002Re_{\mathrm{l}}^2 \\ &- 0.654St^2 + 0.241{\alpha_{\mathrm{S}}}^2 - 0.024Re_{\mathrm{l}}\alpha_{\mathrm{S}} - 0.119St\alpha_{\mathrm{S}}, \end{aligned} \tag{2.23}$$

The cycle-average horizontal force coefficient is given by

$$C_{\mathrm{Xavg}} = 7289.5 - 7672.3St + 179.46St^2, \tag{2.24}$$

We can see from the above expressions that while the average vertical force coefficient is dependent on all the three parameters, the average horizontal force coefficient is a function of Strouhal number only. The procedure used to calculate these expressions will be applied later to develop an aerodynamic model for straight flapping path. The developed model will then be used in the nonlinear flight dynamics framework.

2.2.3 Results

The vertical and horizontal force coefficients are calculated using the approximate expressions given by eq (2.23) and eq (2.24) respectively for the parameter limit range given by Tab. 2.4. Contour and surface plots of these coefficients are observed to study the relationships between the parameters and the coefficients. Figures 2.20-2.21 show that C_{Xavg} value entirely depends on the Strouhal number for a fixed α_{S}. Similarly, Fig. 2.23 shows C_{Zavg} value is not affected by Reynolds number but only for lower values of Strouhal number. As the Strouhal number approaches the largest value tested, the Reynolds number starts to influence C_{Zavg}. Fig. 2.20 and Fig. 2.22 give the surface plots showing highest values of the average force coefficients.

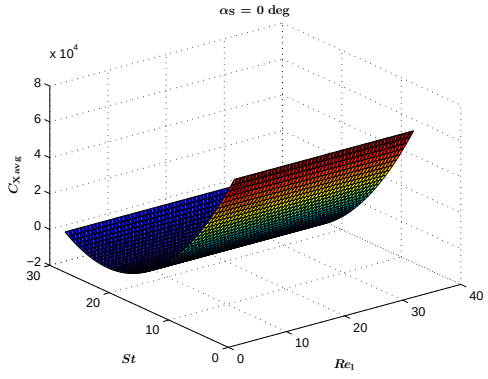

Figure 2.20. Re_{l}-St Surface plot for horizontal force coefficient C_{Xavg} at α_{S} = 0 deg.

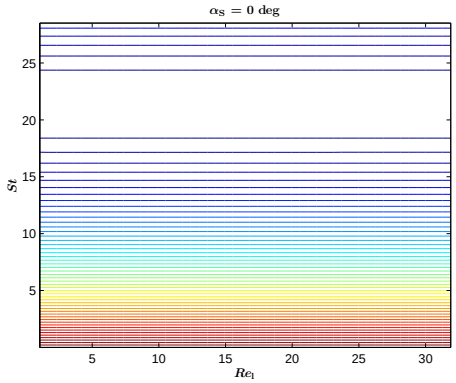

Figure 2.21. Re_{l}-St Contour plot for horizontal force coefficient C_{Xavg} at α_{S} = 0 deg.

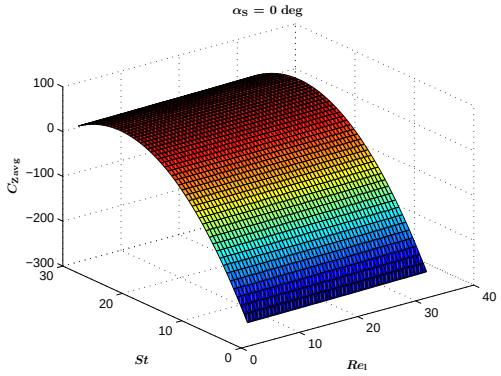

Figure 2.22. Re_l-St Surface plot for vertical force coefficient C_{Zavg} at α_S = 0 deg.

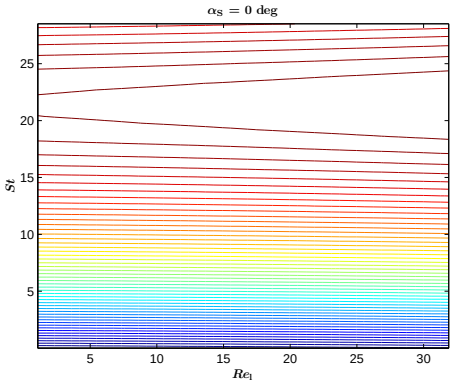

Figure 2.23. Re_l-St Contour plot for vertical force coefficient C_{Zavg} at α_S = 0 deg.

Fig. 2.24 and Fig. 2.25 show C_{Xavg} and C_{Zavg} values depend more on the Reynolds number than the stroke angle of attack.

Fig. 2.26 and Fig. 2.27 show a strong quadratic response behavior of the C_{Xavg} and C_{Zavg} values with respect to the Strouhal number, albeit the C_{Xavg}-St curve has a positive slope while the C_{Zavg}-St curve has a negative slope.

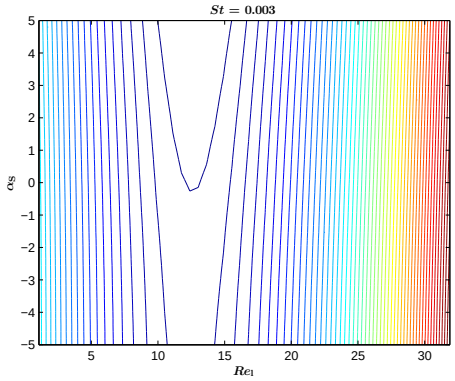

Figure 2.24. Re_l-α_S Contour plot for horizontal force coefficient C_{Xavg} at St = 0.003.

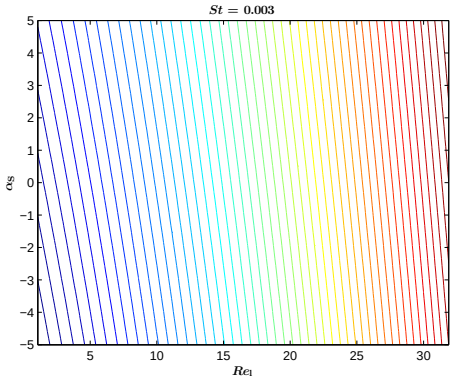

Figure 2.25. Re_l-α_S Contour plot for vertical force coefficient C_{Zavg} at St = 0.003.

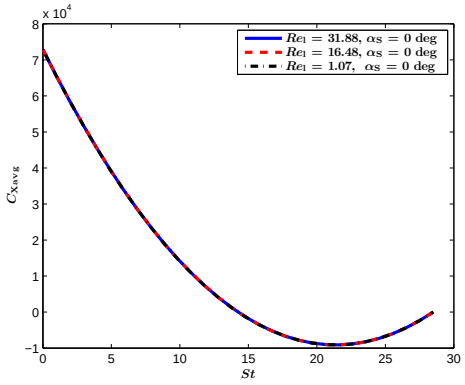

Figure 2.26. Plot for C_{Xavg} versus St.

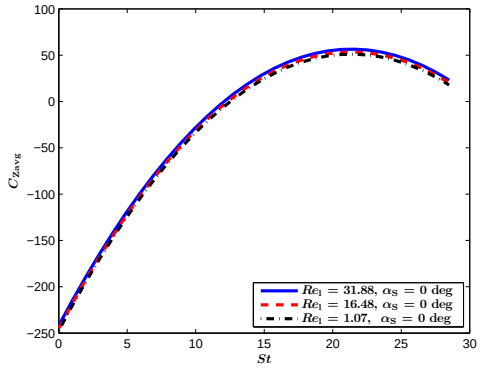

Figure 2.27. Plot for C_{Zavg} versus St.

A positive value of C_{Zavg} would indicate a net lifting force. So according to Fig. 2.22 and Fig. 2.27, a lifting force will only be produced if $St >\sim 14$. Once this critical value of St is reached, the lift force increases slightly with increased Re_l. Note that one may increase St by either increasing the frequency or the length scale or by decreasing the free stream speed. Therefore, a micro-flyer based on the flapping motion given here would require an increase in flapping frequency to maintain level flight at increased forward speeds. Since the lift force, as defined earlier, is a function of frequency squared, the required change in frequency may be slight, but still necessary to maintain steady level flight conditions.

For C_{Xavg}, a negative value would indicate a thrust force. From Fig. 2.26, the response surface indicates a thrust force would be produced with $St >\sim 14$ and is not a function of Re_l. Again, maintaining thrust force with increased free stream speed would require an increase in flapping frequency to hold the required value of St.

Fig. 2.28 shows that C_{Xavg}-α_S trend is same for different Strouhal numbers but the magnitude is different. However one can see from Fig. 2.29 that different Strouhal numbers yield entirely different slopes of the C_{Zavg}-α_S curve.

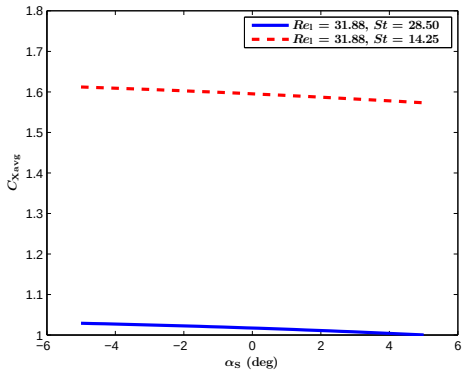

Figure 2.28. Plot for C_{Xavg} versus α_{S}.

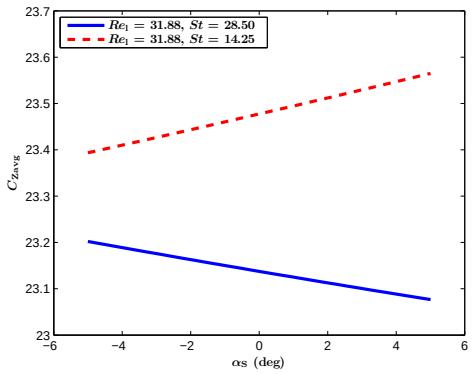

Figure 2.29. Plot for C_{Zavg} versus α_{S}.

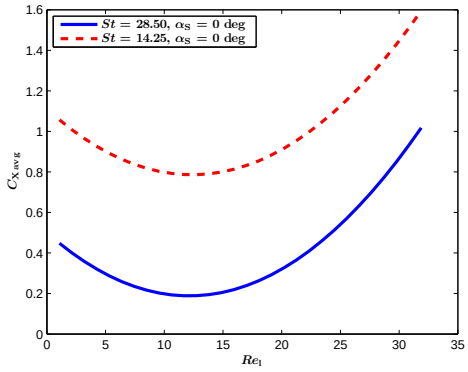

Figure 2.30. Plot for C_{Xavg} versus Re_{l}.

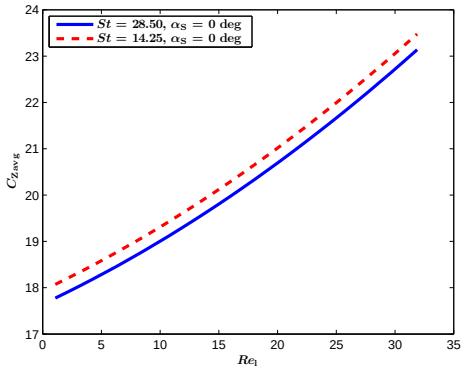

Figure 2.31. Plot for C_{Zavg} versus Re_{l}.

We can see from Fig. 2.30 that C_{Xavg} value decreases at lower values of Reynolds number but increases again after Re_{l} value crosses 14. Fig. 2.31 shows that C_{Xavg} increases steeply as Reynolds number increases.

The response surface predicts optimal values of the non-dimensional parameters to achieve maximum C_{Zavg} and minimum C_{Xavg}. The aim of this exercise is to develop an aerodynamic model that can be used in a nonlinear dynamics framework. The model developed using the method described above should include all the non-dimensional parameters. Morever, sensitivity analysis with larger parameter domain would be conducted. The larger data-set would be helpful in studying the individ-

ual role each of the non-dimensional parameters play in influencing the average force coefficient values. It would also help in determining if there are any regions of these parameter values that would help in achieving desirable forces.

CHAPTER 3

STRUCTURED GRID FOR CFD STUDY

Results of the convergence and validation study for a structured grid are presented. The validated grid will used to perform parametric study and the subsequent sensitivity analysis with non-dimensional parameters by following the methodology described in the previous chapter.

3.1 Rigid Body Dynamic Mesh Zone Motion with Structured Grid

Resolving the boundary layer requires small cell sizes around the body. Structured meshes can resolve the relevant scales and maintain good grid quality. The use of diffusion method in regions of small cells around the body might result in bad quality cells. To overcome this issue, rigid body mesh zone motion method is used close to the body for the numerical implementation. In the rigid body motion, the specified mesh zone moves about a center of gravity location. Specifically, the mesh zone acts as one rigid body, thereby avoiding any mesh smoothing since the mesh quality remains intact. For this reason, structured grid with rigid body mesh motion is chosen for better accuracy of the solution.

At first a structured O-type grid is created over the flat plate used for the DOE with a radius of 20 times the chord length as shown in Fig. 3.1. This grid is specified as a rigid body so that the entire grid moves along the straight flapping path using a user defined function (UDF) in ANSYS-Fluent, which specifies the rotational and translational velocities.

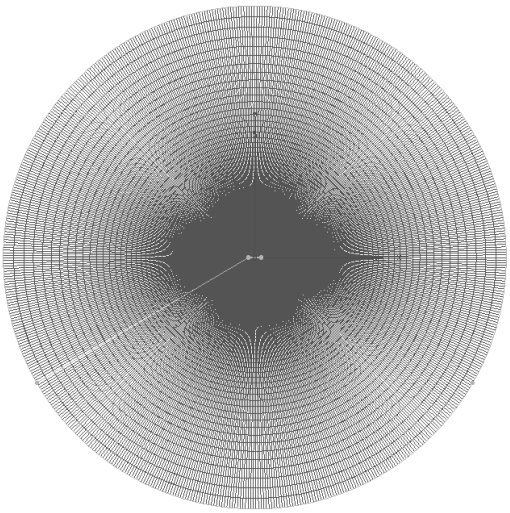

Figure 3.1. Inner Structured Grid.

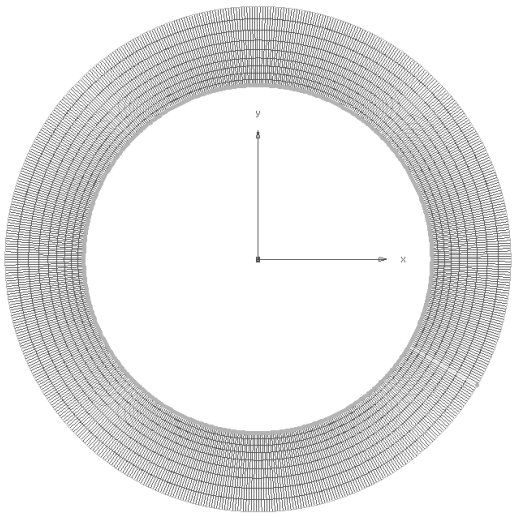

Figure 3.2. Outer Structured Grid.

Another structured O-type outer grid is created over the inner grid, extending by 10 chord lengths as shown in Fig. 3.2. The outer boundary of this outer grid is kept stationary and specified with a velocity inlet boundary condition. Keeping the outer boundary fixed creates a relative motion between the free stream and the flat plate which is pitching while translating along the straight flapping path. The interface of the outer boundary is specified as another rigid body such that the nodes at the interface boundary are made to translate along the straight path without rotating. This is done using another UDF specifying the translational velocity to the interface. As shown in Fig. 3.3(a), the interface between the two grids is specified with a sliding boundary condition, where the fluxes from overlapped faces get distributed to the overlapping cells in proportion to their area of overlap. Boundary diffusion smoothing method is employed only for the outer grid to preserve grid quality and avoid negative cell volumes. The interior nodes of the outer grid move according to the solution of the diffusion equation given by

$$\nabla.(\gamma \nabla \vec{u}) = 0 \tag{3.1}$$

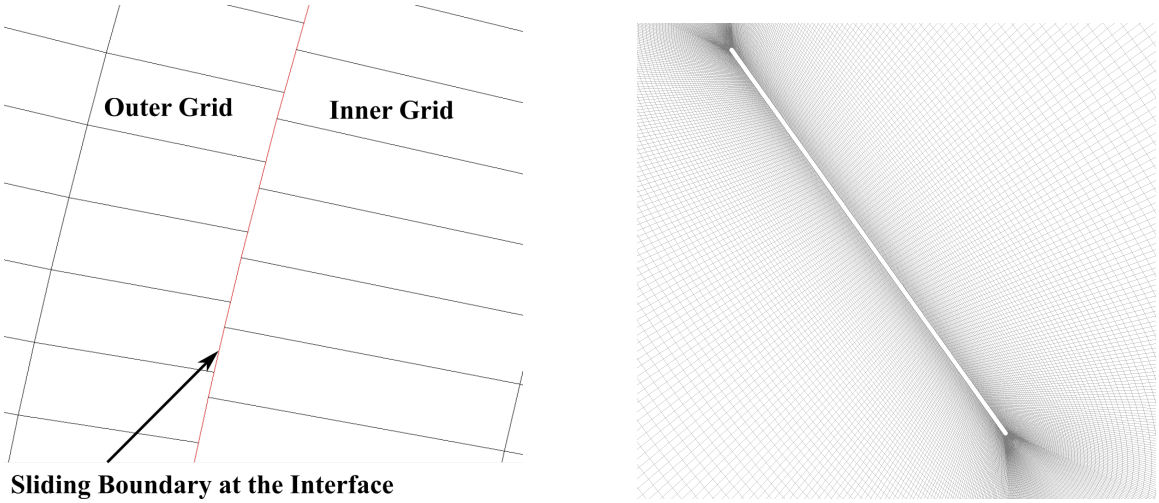

(a) (b)

Figure 3.3. Sliding interfaces at the boundary between the outer and inner grid shown in Fig. (a) and the corresponding flapping position of the flat plate shown in Fig. (b) .

In the next section a thorough grid convergence study is performed on this overset structured grid to select an appropriate refined grid for future DOE runs.

3.2 Grid Convergence Study

The procedure for grid convergence is adopted from [50] and [51]. For the study, three different sets of grids are selected and simulations are run to determine cycle-averaged force coefficient values. Starting with a coarse grid, the grid is refined twice with a refinement factor r set to 2. The parameters of the three grids are given in Tab. 3.1, with grids 1,2 and 3 being the fine, medium and coarse grids respectively.

Table 3.1. Details of convergence study grids

Grid cells	Grid 1 (Fine)	Grid 2 (Medium)	Grid 3 (Coarse)
Inner grid cells	101,916	50,336	25,752
Outer grid cells	5,364	2,544	1,216
Total grid cells	107,280	52,880	26,968

For the simulations, a test case is set for the local Reynolds number Re_{l}=100, Strouhal number St=0.1, geometric function G=0.4 and the stroke angle of attack α_{S}=30 deg. Pressure-velocity coupled solver is used with 1st order implicit transient formulation. For the spatial discretization, standard pressure interpolation scheme is used with 2nd order upwind method for momentum. Green-Gauss cell based gradient method is employed. Using two different user defined functions (UDF), rigid body dynamic mesh zone motion is applied to the inner grid and the interface between the inner and outer grids respectively, with a boundary diffusion smoothing method applied only to the outer grid. The diffusivity parameter is kept at 1. All other simulation parameters are set similar to the DOE simulations explained in chapter 2.

For all the three grids, cycle-averaged vertical and horizontal force coefficients are plotted for 5 flapping cycles as shown in figures 3.4 and 3.5. C_{Xavg} and C_{Zavg} values for the 5th cycle are used as variables for the grid convergence study. The procedure is as follows.

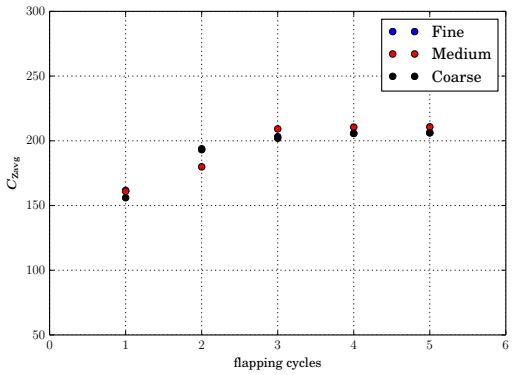

Figure 3.4. Cycle-averaged vertical force coefficient.

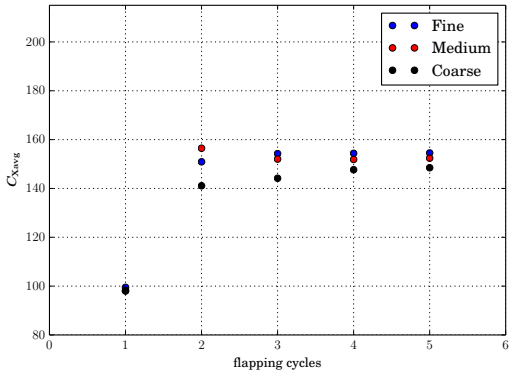

Figure 3.5. Cycle-averaged horizontal force coefficient.

Consider the grid convergence variable ϕ_{i}, for i=1 to 3. For a constant refinement factor r, the apparent order of accuracy p can be calculated from the expression

$$p = \frac{\ln(R)}{\ln(r)} \tag{3.2}$$

where R is a ratio given as

$$R = \frac{\epsilon_{32}}{\epsilon_{21}}, \tag{3.3}$$

where $\epsilon_{32} = \phi_3 - \phi_2$, $\epsilon_{21} = \phi_2 - \phi_1$. Three convergence conditions are possible:

$$\begin{aligned} &(i)\ \textit{Monotonic convergence}: \ 0 < R < 1 \\ &(ii)\ \textit{Oscillatory convergence}: \ R < 0 \\ &(iii)\ \textit{Divergence}: \ R > 1 \end{aligned} \tag{3.4}$$

The grid convergence index (GCI) for a grid solution is given by

$$\mathrm{GCI}^{\mathrm{i+1,i}} = \frac{1.25|\epsilon_{\mathrm{i+1,i}}|}{\phi_{\mathrm{i}}(r^p - 1)} \tag{3.5}$$

Tab. 3.2 summarizes the grid convergence findings for the three selected grids. Note that for C_{Zavg}, the apparent order of accuracy is found to be 3.27. However since

Table 3.2. Grid convergence calculations

Parameters	C_{Zavg}	C_{Xavg}
Grid 1 (Fine)	215.3	144.82
Grid 2 (Medium)	214.5	144.5
Grid 3 (Coarse)	215.3	141.4
ϵ_{32}	0.8	3.1
ϵ_{21}	-0.8	0.32
R	-1	0.1
p	n/a	$3.27 \approx 2$
GCI^{32} (%)	n/a	0.9
GCI^{21} (%)	n/a	0.1

our actual order of accuracy is 2 spatially, this value is used to calculate the GCI. From the table we can see that the GCI reduces substantially as we go from coarser to finer grid. C_{Zavg} gives an oscillatory convergence. So GCI for this variable cannot be found. Results from the convergence study suggest that the fine structured hybrid grid gives acceptable solution accuracy. In the next section, this grid will be used for numerical validation.

3.3 Validation of the Numerical Implementation

Two cases are studied for the validation of the numerical approach for simulations. Literature search performed to identify experimental results for moving airfoils in incompressible laminar flows uncovered flow visualization and other qualitative information. But very little data suitable for quantitative validation were found. Quantitative data for turbulent flows over moving airfoil was far more prevalent. So, in the first study, simulation results for a transient ramp motion of NACA 0012 airfoil are compared with the experimental data for the turbulent flow condition given in the Compendium of Unsteady Aerodynamic Measurements [52]. In the second study, simulation results for a hovering two-dimensional flapping wing are compared with the simulation and experimental results given in [53].

3.3.1 Ramp Motion of NACA-0012 Airfoil

In this study, a structured grid is used in conjunction with the rigid body motion dynamic mesh scheme to simulate a transient ramping motion of a NACA-0012 airfoil about its quarter chord. All the flow characteristics and parameters for the simulation are matched with the experimental set-up for a ramping motion of NACA-0012 airfoil given in the AGARD Report titled 'Compendium of Unsteady Aerodynamic Measurements' [52].

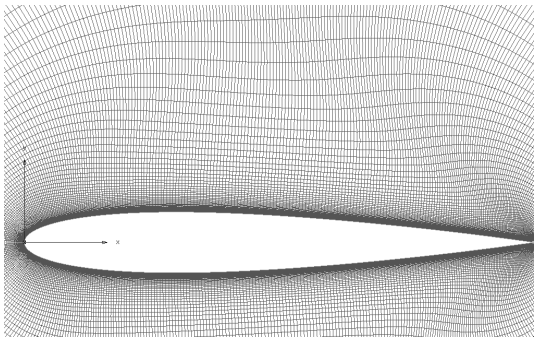

Figure 3.6. Structured grid for ramping motion.

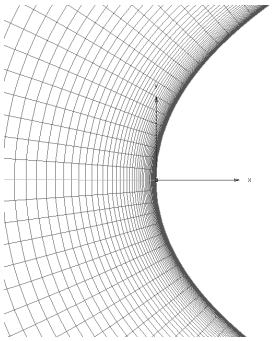

Figure 3.7. Clustered grid around the wall to resolve the turbulent boundary layer.

In the experiment, the pitch angle α is changed from -0.03 to 15.54 degrees in 0.01642 seconds with a continuous ramp motion about its quarter chord, or $0.25c$. The ramp motion data has 16 points, spaced such to have approximately equal incident increments. The ramp incidence rate $\dot{\alpha}$ is not held constant. The experiment is performed at incompressible and turbulent flow condition, with Mach number M = 0.3 and free stream Reynolds Number $Re_\infty = 2.7\times10^6$. The flow and model parameters are tabulated in Tab. 3.3.

For the simulation, a structured O-type grid is created over NACA-0012 airfoil of unit chord length with a radius of 50 times the chord length. 500 points are used along the airfoil and 140 in the vertical direction for the grid shown in Fig. 3.6 which

Table 3.3. Parameter values for AGARD experiment

Parameter	Value
Chord Length, c	0.101 m
Free stream Reynolds Number, Re_∞	2.7×10^6
Mach Number, M	0.3
Free stream Velocity, V_∞	99.73 m/s
Density, ρ	1.225 kg/m^3
Viscosity, μ	4.524845×10^{-6} kg/m-s

has 69,222 quadrilateral cells. More cells are clustered around the airfoil in order to resolve the turbulent boundary layer. The height of the first grid cell from the wall is determined for a non-dimensional wall distance y^+ value of 1 and is found to be $9.5\times10^{-6}c$. The procedure to determine the wall spacing is given in Appendix A. Note that since there is no translation involved in the motion, a hybrid grid is not required.

ANSYS-Fluent is used to solve the Reynolds Averaged Navier Stokes equations (RANS) using the Spalart-Allmaras turbulent model [54] given by the transport equation

$$\frac{\partial}{\partial \mathrm{t}}\left(\rho\tilde{\nu}\right)+\frac{\partial}{\partial x_{\mathrm{i}}}\left(\rho\tilde{\nu}u_{\mathrm{i}}\right)=G_{\nu}+\frac{1}{\sigma_{\tilde{\nu}}}\left[\frac{\partial}{\partial x_{\mathrm{j}}}\left\{\left(\mu+\rho\tilde{\nu}\right)\frac{\partial\tilde{\nu}}{\partial x_{\mathrm{j}}}+c_{\mathrm{b2}}\rho\left(\frac{\partial\tilde{\nu}}{\partial x_{\mathrm{j}}}\right)^{2}\right\}\right]-Y_{\nu}+S_{\tilde{\nu}} \quad (3.6)$$

where G_ν is the production of turbulent viscosity, Y_ν is the destruction of turbulent viscosity in the near-wall region due to wall blocking and viscous damping. $\sigma_{\tilde{\nu}}$ and c_{b2}

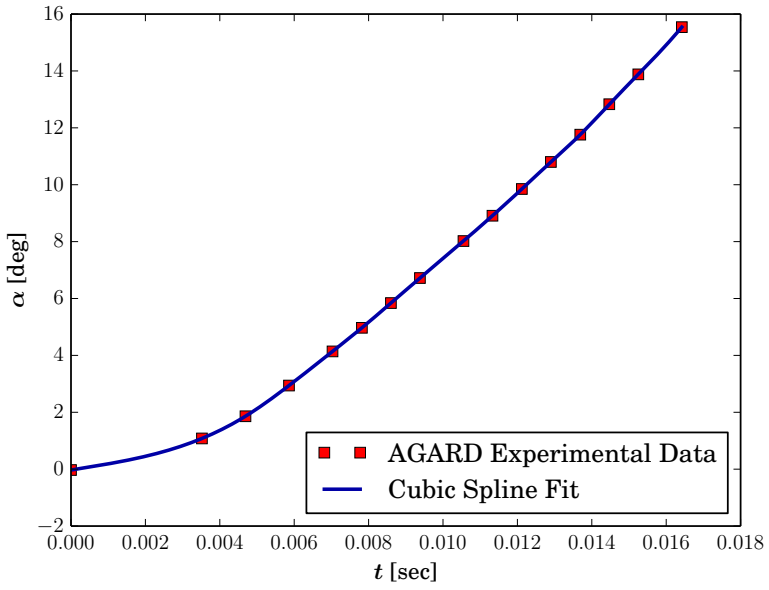

Figure 3.8. Pitch angle variation over time for ramping motion.

Table 3.4. Ramping motion data from AGARD experiment

t [sec]	M	C_{N}	α [deg]
0	0.304	0.0232	-0.03
0.00352	0.298	0.1331	1.08
0.00469	0.3	0.2097	1.86
0.00586	0.301	0.3253	2.94
0.00703	0.297	0.45	4.14
0.00782	0.294	0.5494	4.97
0.0086	0.306	0.5959	5.84
0.00938	0.301	0.7064	6.72
0.01055	0.298	0.8499	8.02
0.01133	0.298	0.9454	8.91
0.01212	0.298	1.0353	9.85
0.0129	0.299	1.127	10.8
0.01369	0.297	1.2531	11.76
0.01447	0.301	1.3046	12.83
0.01525	0.298	1.4453	13.88
0.01642	0.294	1.6368	15.54

are constants and ν is the molecular kinematic viscosity. $S_{\tilde{\nu}}$ is a user-defined source term.

A pressure-velocity coupled solver is used with 2nd order implicit transient formulation. For the spatial discretization, standard pressure interpolation scheme is used with 2nd order upwind methods for momentum and modified turbulent viscosity. Since only the inner grid is used in this case, the grid is specified a rigid body motion using a UDF. No smoothing scheme is employed for the simulation.

For the ramping motion, the pitch angle experimental data is recreated by fitting a cubic spline over the data with 1000 points. The pitch angle variation is shown in Fig. 3.8. The ramping motion data is given in Tab. 3.4, where C_{N} is the normal force coefficient. The time step for the simulation is chosen as

$$\mathrm{d}t = \frac{\text{total ramping motion time}}{1000} = \frac{0.01642}{1000} = 1.642{\times}10^{-5} \tag{3.7}$$

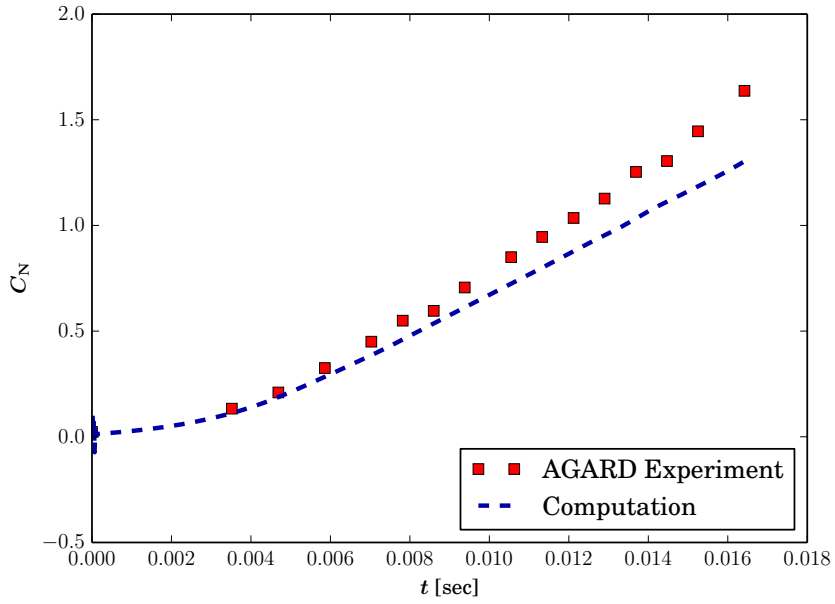

Figure 3.9. Comparison of normal force coefficient values for ramping motion.

The lift and drag coefficients C_L and C_D respectively are computed by dividing the unsteady lift and drag forces by the dynamic pressure force $\frac{1}{2}\rho V_\infty^2 c$. These force coefficients are in turn used to calculate the normal force coefficient C_N as follows.

$$C_N = C_L \cos(\alpha) + C_D \sin(\alpha) \tag{3.8}$$

The C_N values from the simulation are compared with the corresponding values from the experiment data. The comparison is shown in Fig. 3.9. As seen from the figure, correct trend is captured and the computed and measured data are within an order of magnitude so there is excellent qualitative agreement. The deviation above the angle of attack of 7 degrees is most likely due to premature separation of the flow on the suction side of the airfoil. Again, this is likely due to the inaccuracy of the turbulence model. Better agreement at high angles of attack could by achieved by tuning the model parameters for this specific case. Nonetheless, the simulation result

is good enough to merit the use of the numerical implementation involving structured grid with rigid body motion for future simulations.

3.3.2 Two-Dimensional Flow over a Hovering Flapping Wing

For this study, 2-D computational forces obtained using the numerical implementation on a generic hovering wing undergoing sinusoidal motion along a stroke plane are compared with the experimental results published in [53]. The authors, Wang et al. obtained experimental results by measuring force and low data using a dynamically scaled robotic fly, with the wing cut to the planform of *Drosophila* wing as described in [1]. For the computational results, they used a thin 2-D wing element of elliptic cross section to perform the same kinematics as that in the experiments.

For the result validation using 2-D computations, the overset structured grid determined by the grid convergence study is chosen, which uses a 2-D flat plate instead of an elliptic cross-section used by the authors. The flow solution method used to perform the simulations was kept same as that in the grid convergence study.

The wing follows a sinusoidal flapping and pitching motion, with the wing sweeping in the horizontal plane and pitches about its spanwise axis with a single frequency f. The kinematics is given by

$$x(t) = \frac{A_0}{2}\cos(2\pi f t), \tag{3.9}$$

$$\alpha(t) = \alpha_0 + \beta\sin(2\pi f t + \phi), \tag{3.10}$$

where $x(t)$ is the position of wing center, and $\alpha(t)$ is wing orientation with respect to x-axis. The translational and angular velocities are defined as

$$\mathrm{U}_0(t) = \frac{\mathrm{d}x(t)}{\mathrm{dt}} \tag{3.11}$$

$$\Omega(t) = \frac{\mathrm{d}\alpha(t)}{\mathrm{dt}} \tag{3.12}$$

The other parameters are

A_0 : stroke amplitude
α_0 : initial angle of attack
β : amplitude of pitching angle of attack
f : flapping frequency
ϕ : phase difference between $x(t)$ and $\alpha(t)$

The translational motion of the wing is non-dimensionalized using two non-dimensional parameters, the Reynolds number, $Re = \mathrm{U_{max}c}/\nu = \pi f A_0 c/\nu$, and A_0/c, where $\mathrm{U_{max}}$ is the maximum wing velocity, and c is the chord. For the validation, Re = 75, $A_0/c = 2.8$. The other parameters α_0, β and f are set to be $\pi/2$, $\pi/4$ and 0.25 Hz respectively.

Simulation results for three cases, $\phi = \pi/4$, 0 and $-\pi/4$, corresponding to the advanced, symmetric and delayed rotation are studied. Instantaneous lift (C_L) and drag (C_D) coefficients are obtained during the first four flapping cycles and are plotted for comparison. Figures 3.11–3.12 show the lift and drag coefficients for the three cases, with Fig. 3.11(a), Fig. 3.10(a) and Fig. 3.12(a) showing the instantaneous wing positions, while Fig. 3.11(b), Fig. 3.10(b) and Fig. 3.12(b) show the comparison of 2-D

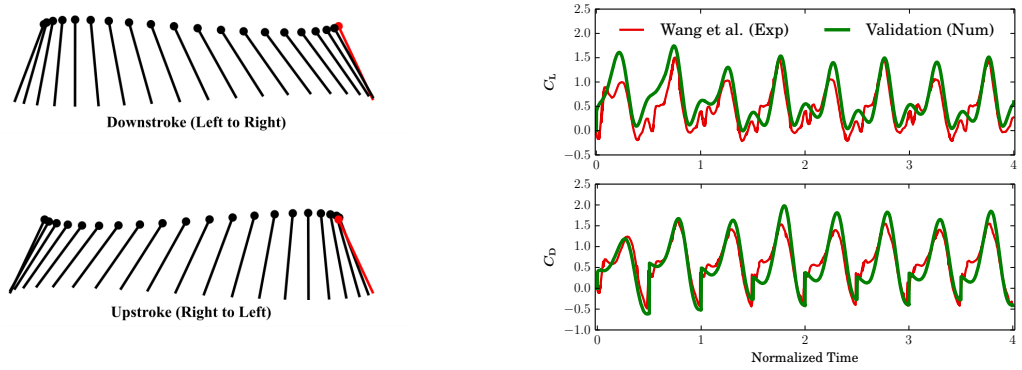

(a) (b)

Figure 3.10. Lift and drag coefficients during advanced rotation (ϕ=$\pi/4$; A_0/c=2.8) (a) Instantaneous wing positions (b) Results Comparison.

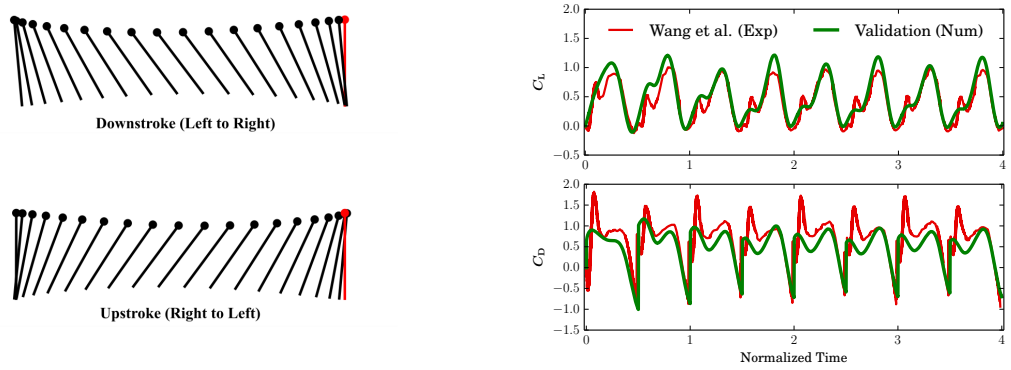

(a) (b)

Figure 3.11. Lift and drag coefficients during symmetric rotation (ϕ=0; A_0/c=2.8) (a) Instantaneous wing positions (b) Results Comparison.

numerical results obtained using structured grid with the corresponding experimental results given in the paper.

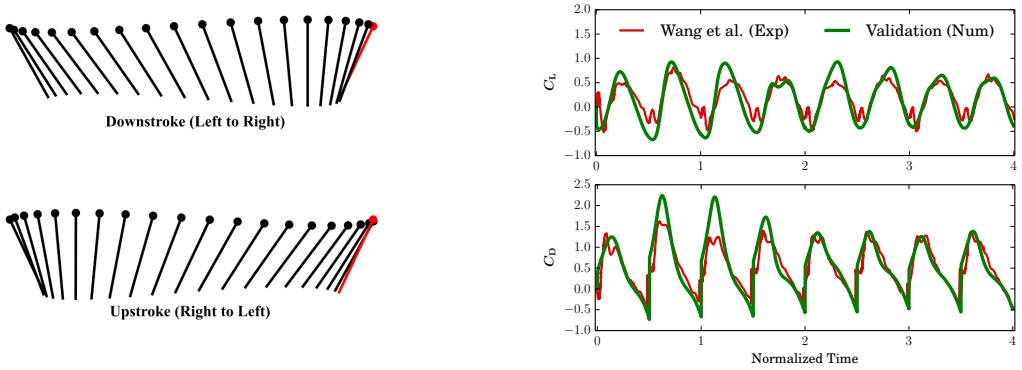

(a) (b)

Figure 3.12. Lift and drag coefficients during delayed rotation (ϕ=$-\pi/4$; A_0/c=2.8) (a) Instantaneous wing positions (b) Results Comparison.

One can see from Fig. 3.10 that for advanced rotation, that the numerical simulation overestimates the lift coefficient peak during the first half of every cycle (downstroke), while matching the value for the upstroke. The drag coefficient matches

well with the experiments overall. But the simulation cannot capture the behavior of force coefficients at the start of the cycles. In case of symmetric rotation shown in Fig. 3.11, the simulation result underestimates the drag coefficient value, while the lift coefficient is slightly overestimated. For the delayed rotation case shown in Fig. 3.12, the simulation result overestimates both lift and drag coefficients for the first three cycles, but matches well with the values in the fourth cycle. Overall, the numerical simulation manages to capture the trends of the lift and drag coefficients in all the three cases.

The above validation results illustrate that the numerical implementation setup works well with the overset structured grid. All the CFD analysis from here on will be done using this set up.

CHAPTER 4

RESULTS FOR PARAMETRIC STUDY OF FLAPPING PATHS

Results of the parametric study of figure-8 and straight flapping paths conducted using the structured grid are presented. The procedure adopted is same as the one described in sec. 2.1. For this study, a new non-dimensional number called the Inverse Strouhal number Sr is introduced, which is defined as

$$Sr = \frac{V_\infty}{fL} = \frac{1}{St} \tag{4.1}$$

For a constant flapping frequency f and semi-span L, Sr essentially describes the effect of the free stream velocity on the force production. Here numerical simulations are performed to obtain cycle-averaged vertical and horizontal force coefficients for the 51st cycle at different inverse Strouhal number values. Figures 4.1 and 4.2 show the results for force coefficients convergence for figure-8 and straight path respectively. As one can see from both the plots, the cycle-averaged force coefficients converge to higher values with increasing inverse Strouhal number. There is not much change in the values at low Sr number. Also, positive C_{Xavg} is drag. Therefore in order to get thrust, the force coefficient needs to be below zero, which is obtained when $Sr < 0.167$ for both the flapping paths.

In order to understand the result better, the instantaneous force coefficients at Sr values of 0 and 10 for straight flapping path are plotted. $Sr = 0$ corresponds to hover case, while $Sr = 10$ corresponds to a free stream velocity of 3 m/s. As seen in Fig. 4.3, the instantaneous vertical and horizontal force coefficients are plotted on the same graph, with y-axis for C_{Z} on the left and that for C_{X} on the right. Vorticity and Z-velocity contours for the two cases are shown in Fig. 4.4-4.7. These plots

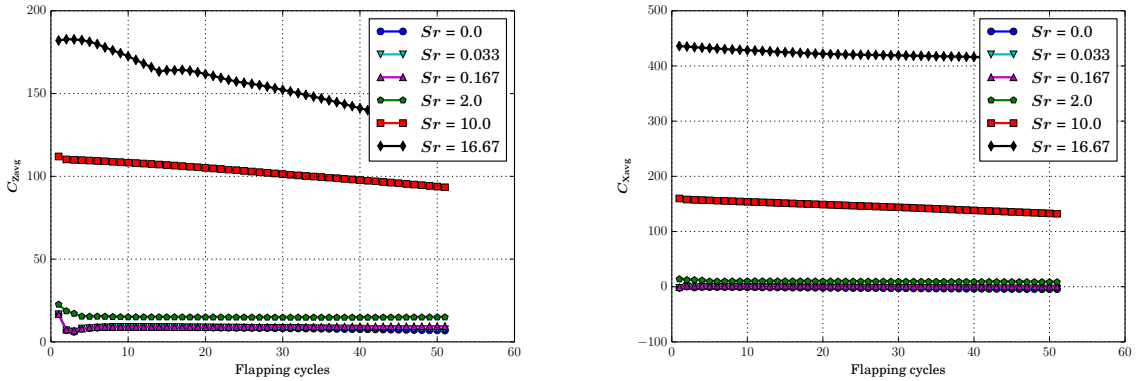

(a) (b)

Figure 4.1. Force coefficients convergence for figure-8 path (a) C_{Zavg} (b) C_{Xavg}.

are discussed based on three mechanisms of force production: *attached leading edge vorticies* (LEVs), *wake capture*, and *jet induced downward momentum*.

(a) Attached LEVs:

Leading Edge Vortex creates a region of low pressure due to which a suction force is generated on the wing. The role of LEV in lift generation in insect flight has been first identified by Ellington et al. in [55]. Following this work, several researchers [**?**, 1, 56, 57] have investigated and underlined the role of LEV in lift

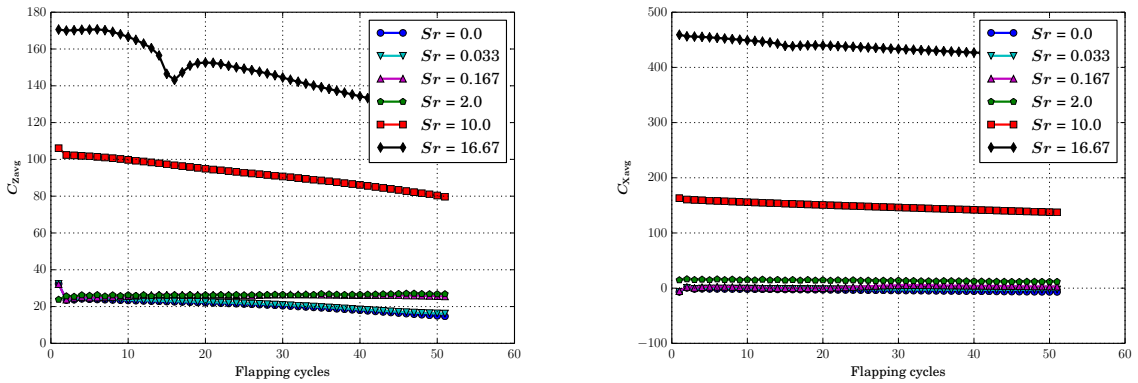

(a) (b)

Figure 4.2. Force coefficients convergence for straight path (a) C_{Zavg} (b) C_{Xavg}.

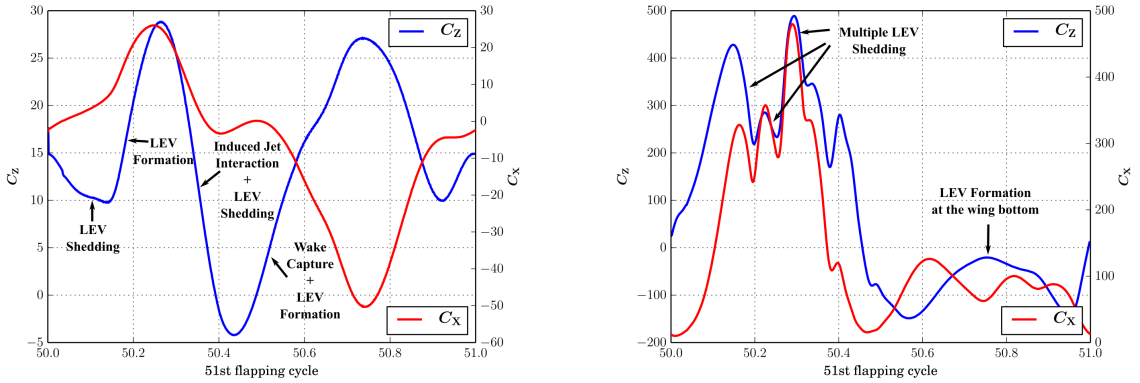

(a) (b)

Figure 4.3. Plots showing dominant force producing mechanisms to obtain C_Z-C_X values for the 51st cycle of a wing flapping in a straight path at (a) Sr=0 (b) Sr=10.

production in wings. At $Sr = 0$, the valley in the lift curve at the start of the downstroke is due to the shedding of the leading edge as shown in Fig. 4.4 plot A. The subsequent increase in lift can be attributed to the increase in circulation of the newly formed LEV (plot B) as the stroke progresses. At $Sr = 10$ as shown in Fig. 4.5 plots A-C, the LEV forms on the upper surface of the wing and sheds multiple times during the upstroke due to the higher convective velocity due to which multiple peaks are observed in force generation. During the downstroke, the LEV forms on the lower surface and creates a downward suction as seen in plots D-F. This can be seen from negative lift generation in Fig. 4.3(b).

(b) Wake Capture:

Dickinson et al. [1], Birch and Dickinson [58] have conducted experiments on low Reynolds number flapping wings representing the wing of a fruit fly to investigate the effect of wing-wake interaction. Depending on the kinematics this interaction can enhance lift production due to the induced velocity on the wing by wake vortices shed during the previous stroke. This was also shown by Trizila et al. [59] and Wang [57] using computational analysis. Wake capture is more prominent

at lower Sr. For $Sr = 0$, lift peak in the upstroke region is obtained mainly due to the wake capture, which can be seen in Fig. 4.4 plot D. Also, when the wing moves through the wake shed in the downstroke, a negative peak in drag curve is observed. Wake capture is not very prominent at higher Sr and no clear peaks are observed immediately after wing reversal (Fig. 4.3(b) plots D-F).

(c) Jet Induced Downward Momentum:

Freymuth [60] experimentally studied flow around an airfoil undergoing hover and observed a jet like profile which is a result of the Karman vortex street in reverse generated by the previous stroke. Trizila et al. [59,61] have observed a downward jet velocity profile from their computations and noticed a drop in lift curve when the wing interacts with this downward jet. The downward jet is more prominent at lower Sr numbers. The wing-jet interaction is observed during the 2nd half of the stroke as seen in Fig. 4.6. The lift reduction during the 2nd half of the stroke from the plot could be due to this interaction. At higher Sr, no jet is observed as (see Fig. 4.7). Due to the higher induced velocities in the streamwise direction, the vortices convect away and a vortex sheet is observed behind the wing instead as seen in Fig. 4.5. The reduction in lift observed during the 2nd half of the stroke is due to the formation of the LEV at the bottom of the wing.

The above study gave a clearer picture of the interaction between different force producing mechanisms that yield instantaneous values. It is to be noted that the objective of this research is not to develop reduced order models for these mechanisms, but to to develop a single aerodynamic model that is reflective of all of the above effects. Nonetheless, this study would be helpful in determining optimal flapping trajectories that produce lift and thrust.

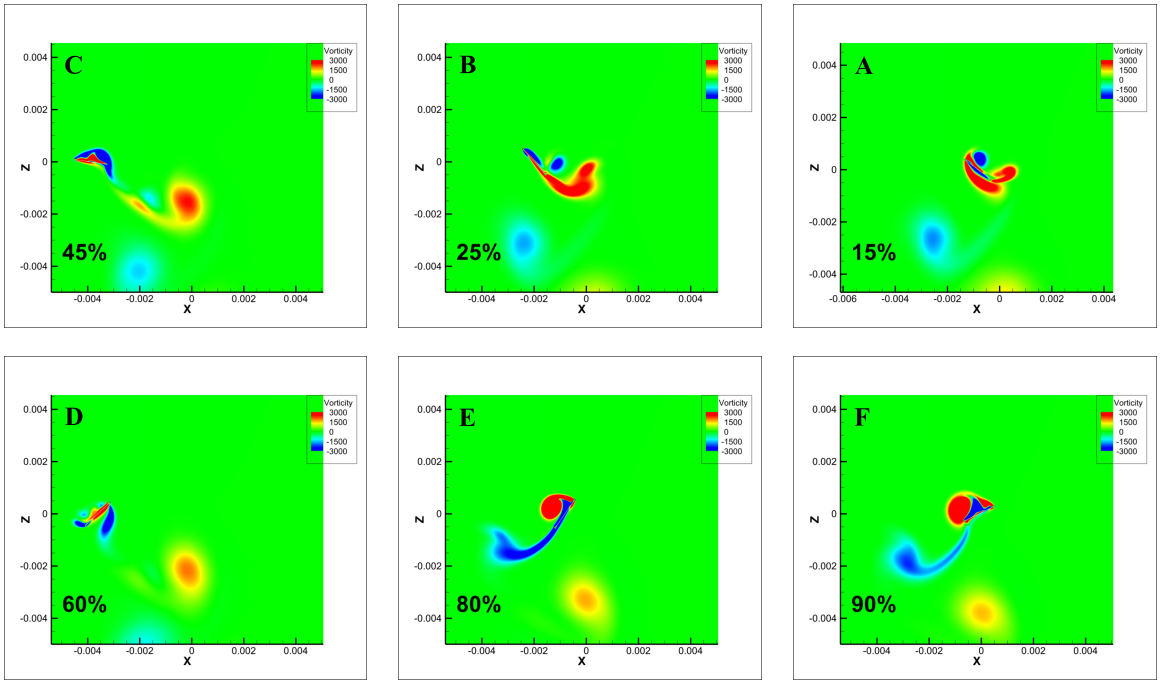

Figure 4.4. Vorticity contours in percent cycle times for $Sr = 0$. The first row shows downstroke (right to left), the next upstroke (left to right).

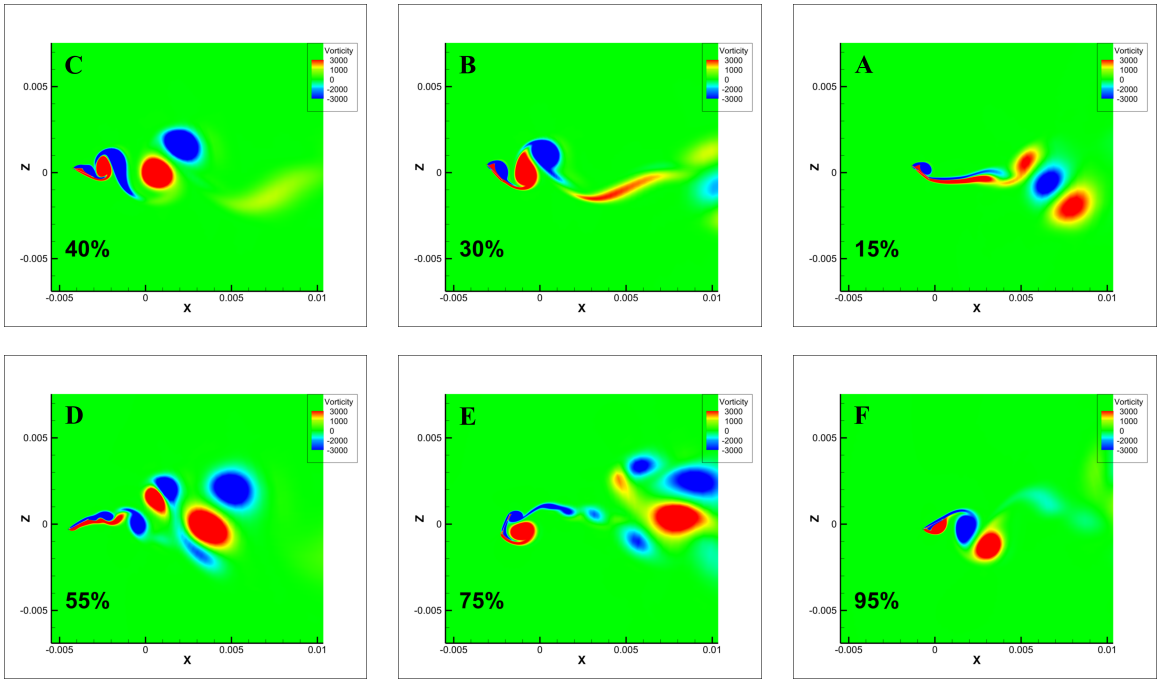

Figure 4.5. Vorticity contours in percent cycle times for $Sr = 10$. The first row shows downstroke (right to left), the next upstroke (left to right).

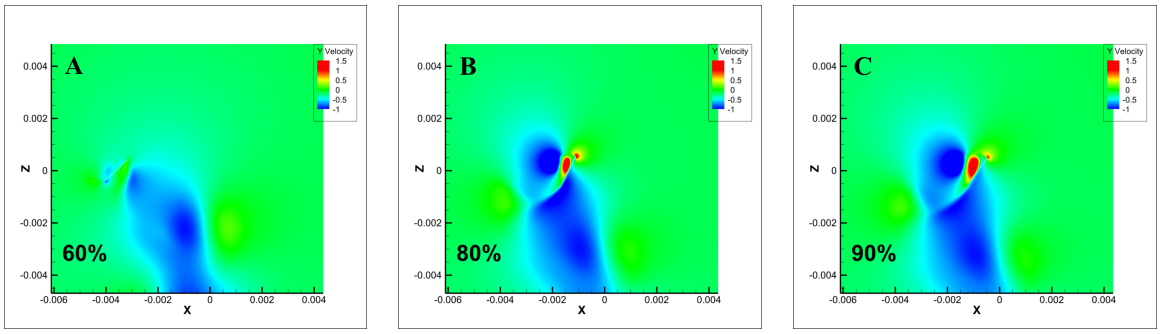

Figure 4.6. Z-Velocity contours in percent cycle times for $Sr = 0$. Upstroke only (left to right).

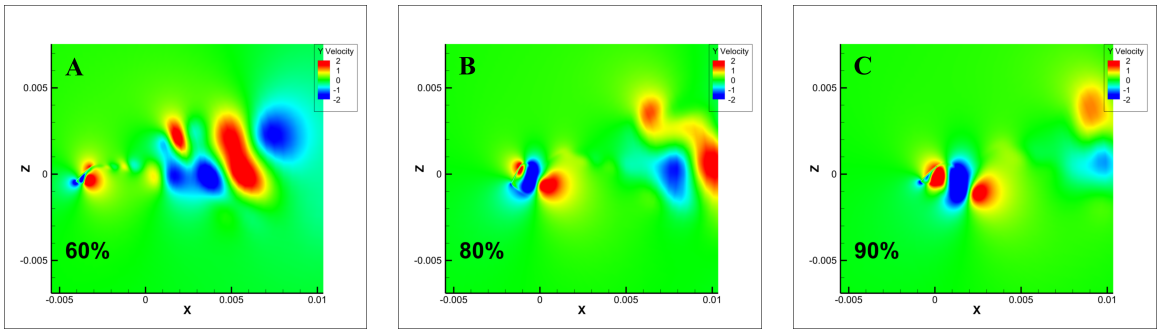

Figure 4.7. Z-Velocity contours in percent cycle times for $Sr = 10$. Upstroke only (left to right).

CHAPTER 5

RESULTS FOR SENSITIVITY ANALYSIS WITH LARGE DOE

In section 2.2, in order to understand the combined effects of the non-dimensional parameters on force production, a design of experiments (DOE) was carried out with a three-level full factorial design method to conduct sensitivity analysis using response surface methodology. Local Reynolds number, Strouhal number and stroke angle of attack were chosen as parameters for the analysis with maximum, minimum and mean values picked for each as required for the full factorial method. The geometric function was set at a constant value of 0.4 for the entire DOE. Straight flapping path was chosen for the study. Cycle-averaged horizontal and vertical force coefficient values C_{Xavg} and C_{Zavg} respectively were obtained by running flow simulations for every design point of the DOE. Since the DOE data-set was small, a quadratic polynomial graduating response function was used to approximate the values of these coefficients in the region between the design points by performing the method of least squares minimization.

In this study, an effort is being made to build up on the previous results by using a large data-set for the DOE. The idea is to thoroughly investigate the sensitivity of two parameters at a time, while setting the other parameters at a constant value. This would be helpful in providing an insight into the role played by these parameters in influencing the force generation in flapping wings. Tab. 5.1 gives the value ranges for old and new DOE data sets.

Table 5.1. Parameter Value Ranges for Large DOE Data-set

Parameter	Old Data-set	Large Data-set
Re_{l}	1 to 31.88	1 to 200
St	0.003 to 14.25	0.1 to 5
α_{S}	-5 to 5 deg	0 to 90 deg
G	constant at 0.4	constant at 0.4

5.1 Role of Stroke Angle of Attack and Local Reynolds Number

Firstly the influence of the stroke angle of attack α_{S} and the local Reynolds number Re_{l} on the average force coefficient values is studied. Re_{l} is varied from 1 to 200 and α_{S} is varied from 0 to 90 degrees. Strouhal number. The effects are studied at Strouhal numbers of 0.1 and 5.

The simulations are run for 5 flapping cycles with 1000 time steps per cycle. The unsteady forces produced by the wing section are computed by integrating the time-variant static pressure over the wing section to produce instantaneous horizontal and vertical force coefficients C_{X} and C_{Z} respectively. The reference values used for calculating these coefficients are parametrized similar to the boundary conditions. These force coefficients are then further integrated over the fifth cycle to produce the cycle-averaged force coefficients C_{Xavg} and C_{Zavg}. As mentioned previously, the sign convention for these coefficients is based on the Eulerian Frame. This means that positive C_{Xavg} is considered drag force and negative value is considered thrust force. Similarly, a positive C_{Zavg} value is considered as a net lifting force.

Fig. 5.1 shows the variation of cycle-averaged force coefficients with the stroke angle of attack at different Re_{l} values for $St = 0.1$. It can be seen from Fig. 5.1(a) that for all Re_{l} values, the C_{Zavg} value increases linearly with the increase in α_{S} value from around 0 to 48 deg. Above 48 deg, the relation has a second order behavior. Maximum and minimum C_{Zavg} values are obtained at corresponding maximum and

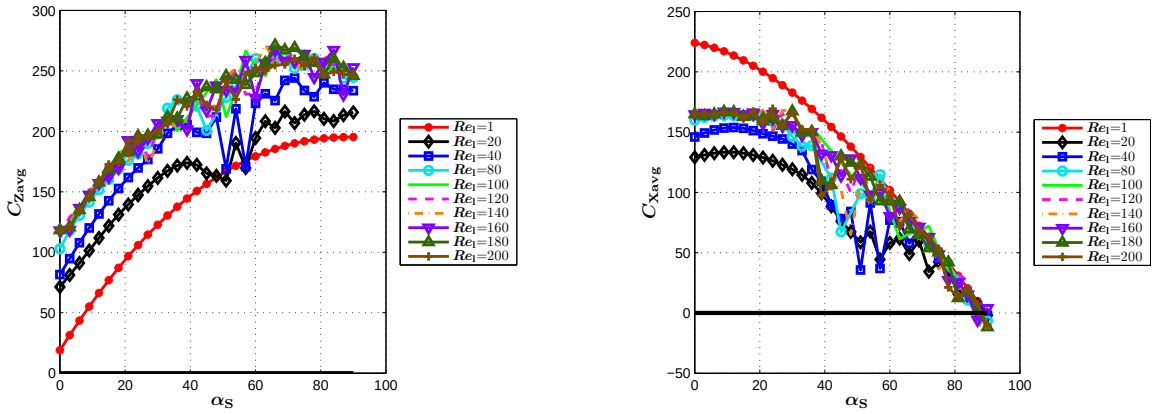

(a) (b)

Figure 5.1. (a) C_{Zavg} vs α_{S} (b) C_{Xavg} vs α_{S} for different local Reynolds number values at $St = 0.1$.

minimum α_{S} values. Fig. 5.1(b) shows C_{Xavg} has a strong quadratic behavior at lower α_{S} values. It is seen that beyond α_{S} value of 48 deg, the smooth quadratic nature of the curves for all Re_{l} values vanishes. Since positive C_{Xavg} is considered drag, maximum drag is produced at smaller magnitudes of α_{S} values for all Re_{l}, while Re_{l} values of 1 to 40 yield small thrust values around stroke angle of attack values of 90 deg.

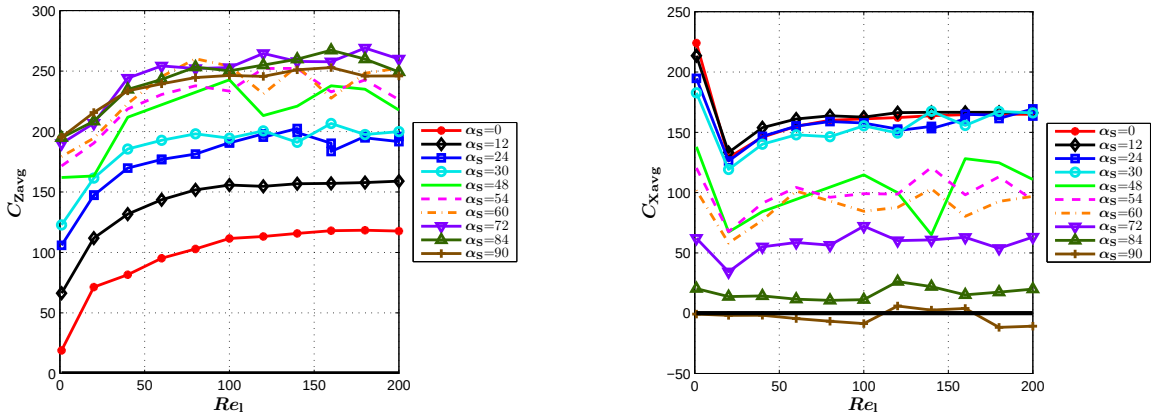

(a) (b)

Figure 5.2. (a) C_{Zavg} vs Re_{l} (b) C_{Xavg} vs Re_{l} for different stroke angle of attack values at $St = 0.1$.

Fig. 5.2 shows the variation of cycle-averaged force coefficients with the local Reynolds number at different α_S values for $St = 0.1$. It can be seen from both Fig. 5.2(a) and Fig. 5.2(b) that the force coefficient values do not change much at higher Re_l values for all α_S. The largest values of C_{Zavg} are obtained at higher α_S values. Similarly C_{Xavg} values become small as α_S is increased, with 90 deg angle yielding net thrust.

Between 40 and 60 degrees, changes in C_{Zavg} and C_{Xavg} values become very erratic. To understand this behavior, simulations are run at select α_S values and at $Re_l = 40$ and 100 for 25 cycles. Figure 5.3 shows that for $Re_l = 40$ and $84 \sim> \alpha_S <\sim 36$, average force coefficients converge in less than 5 cycles. However for α_S values between 36 and 84 deg, the force coefficients do not converge even after 25 cycles. At $Re_l = 100$, as seen in Fig. 5.4, the force coefficients fail to converge even for higher α_S values. This means at these specific parameter that averaging the force coefficients after 5 cycles would yield erroneous results.

Figures 5.5 and 5.6 show the variation in force coefficient values at different α_S and Re_l values for $St = 5$. One can see that the erratic variations in C_{Zavg}-C_{Xavg}

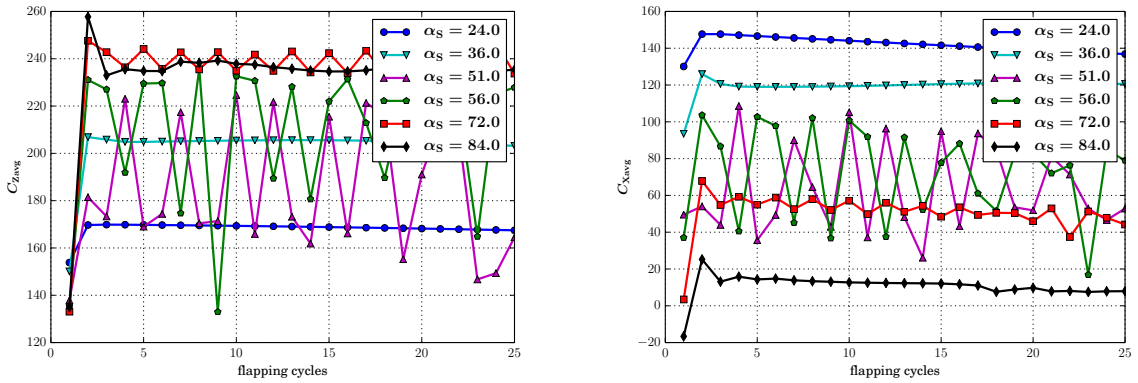

(a) (b)

Figure 5.3. (a) C_{Zavg} (b) C_{Xavg} for different α_S at $Re_l = 40$.

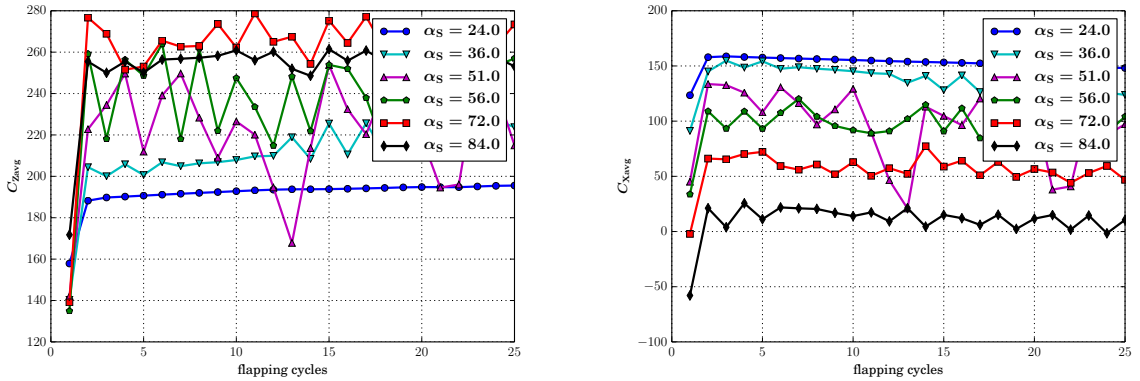

(a) (b)

Figure 5.4. (a) C_{Zavg} (b) C_{Xavg} for different α_{S} at $Re_{\mathrm{l}} = 100$.

occur only for $Re_{\mathrm{l}} >\sim 140$. Below this value, the plots show a smooth trend. This shows that the Strouhal number plays an important role in determining the validity of cycle averaging of the forces.

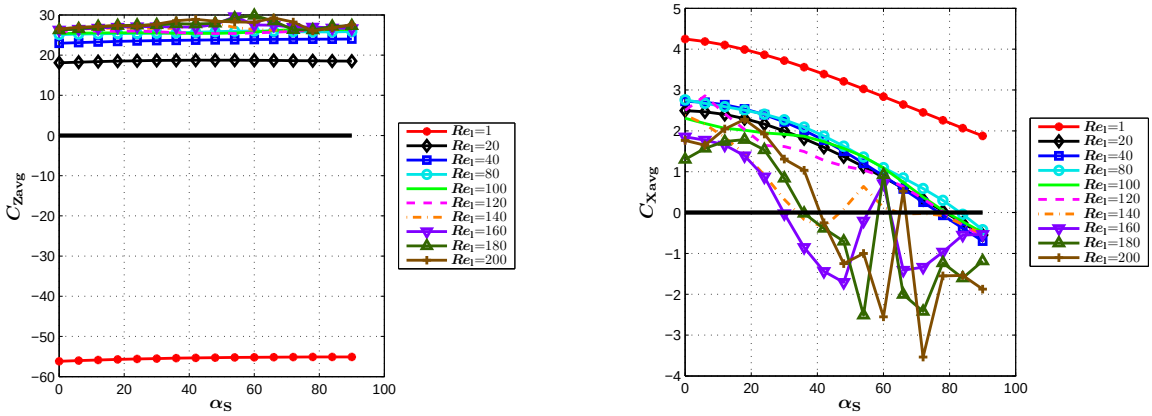

(a) (b)

Figure 5.5. (a) C_{Zavg} vs α_{S} (b) C_{Xavg} vs α_{S} for different local Reynolds number values at $St = 5$.

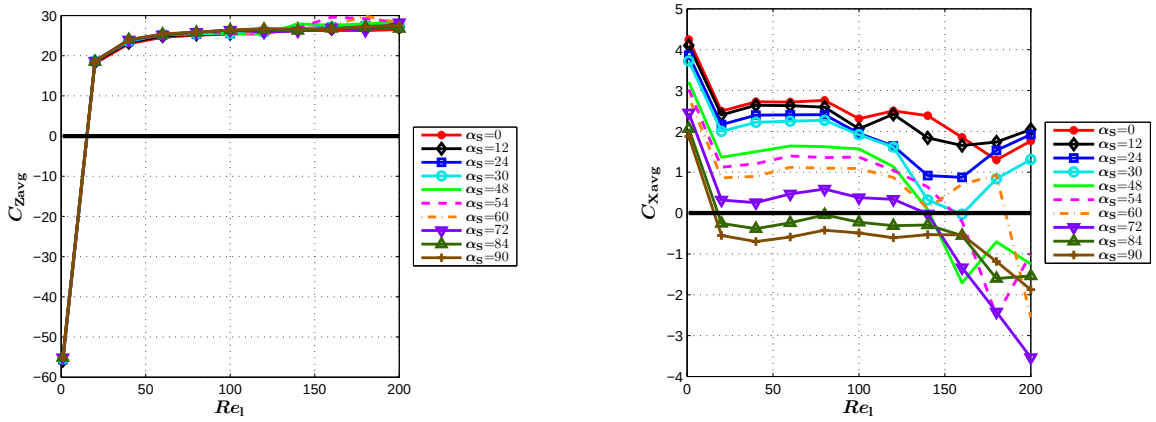

(a) (b)

Figure 5.6. (a) C_{Zavg} vs Re_{l} (b) C_{Xavg} vs Re_{l} for different stroke angle of attack values at $St = 5$.

5.2 Role of Stroke Angle of Attack and Strouhal Number

In this case, the influence of the stroke angle of attack α_{S} and the Strouhal number St on the average force coefficient values is studied. For this study, St is varied from 0.1 to 5 and α_{S} is varied from 0 to 90 degrees. Simulations are run at $Re_{\text{l}} = 40$ and 200.

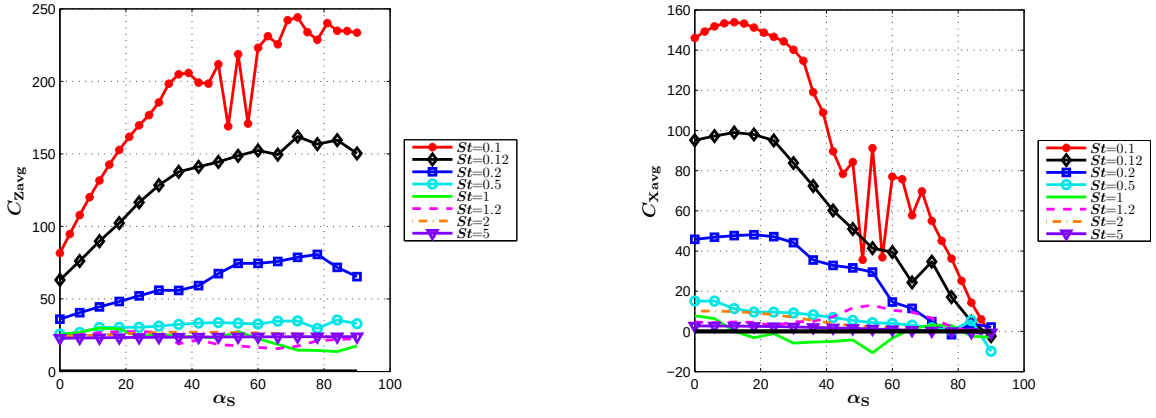

(a) (b)

Figure 5.7. (a) C_{Zavg} vs α_{S} (a) C_{Xavg} vs α_{S} for different Strouhal number values at $Re_{\text{l}} = 40$.

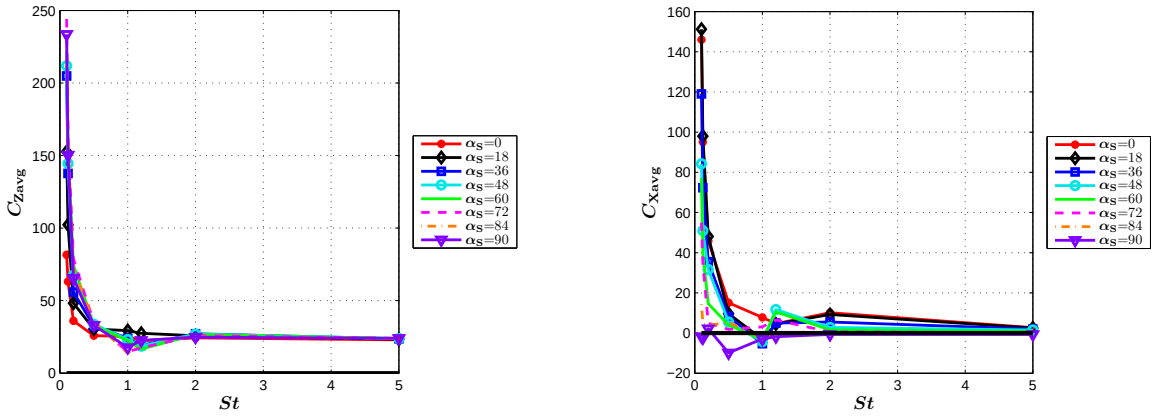

(a) (b)

Figure 5.8. (a) C_{Zavg} vs St (b) C_{Xavg} vs St for different stroke angle of attack values at $Re_{\text{l}} = 40$.

Figure 5.7 shows the force coefficients variation with stroke angle of attack for $Re_{\text{l}} = 40$. As seen in the plots, the force coefficients show erratic behavior at low St values. As St increases, the curves get smoother. Also, C_{Zavg}-α_{S} and C_{Xavg}-α_{S} curves get flatter, implying that there is no effect of stroke angle of attack on the force coefficient values. From Fig. 5.8, it can be noted that both lift and thrust can be generated together either with a combination of small St and $\alpha_{\text{S}} = 90$ deg, or at $St = 5$. As Re_{l} increases, the band of Strouhal number values giving erratic force coefficient plots also increases, as seen from Fig. 5.9 and Fig. 5.10. Also, thrust generation is seen at small St values for a number of α_{S} values.

The purpose of this study was to determine specific regions of non-dimensional parameters that yield combine lift and thrust. Although these regions were observed, results showed that the cycle averaging of the force coefficients do not work at all parameter regions. This is an important observation and needs to be followed upon while building an aerodynamic data in order to develop an aerodynamic model based on cycle-averaged force coefficient values.

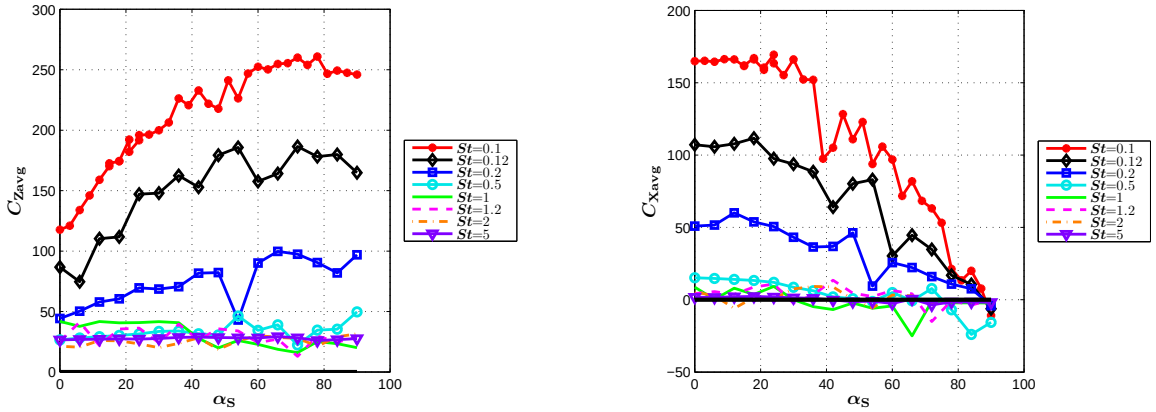

(a) (b)

Figure 5.9. (a) C_{Zavg} vs α_{S} (b) C_{Xavg} vs α_{S} for different Strouhal number values at $Re_{\text{l}} = 200$.

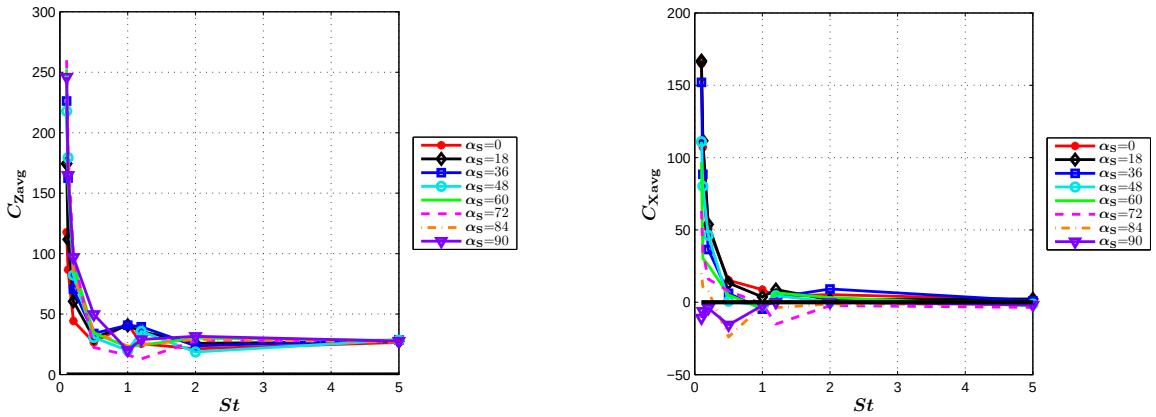

(a) (b)

Figure 5.10. (a) C_{Zavg} vs St (b) C_{Xavg} vs St for different stroke angle of attack values at $Re_{\text{l}} = 200$.

CHAPTER 6

FLIGHT DYNAMICS ANALYSIS

6.1 Flight Dynamics Formulation

In this section, the development of a nonlinear dynamic model of flapping wing micro-flyer derived from first principles is described. The derivation of a set of nonlinear, 6-DOF equations of motion of micro-flyer is similar to that adopted for a standard aircraft model stated by Etkin [62]. Here the aerodynamic forces and moments generated due to the flapping of wings are equated to the rate of change of linear momentum and angular momentum respectively to form the governing equations.

Newton's Law of Linear Motion:

$$\frac{\mathrm{d}}{\mathrm{d}t}\left[\int_V \frac{\mathrm{d}\vec{r'}}{\mathrm{d}t}\left(\rho_\mathrm{A}\mathrm{d}V\right)\right] = \int_V \vec{g}\left(\rho_\mathrm{A}\mathrm{d}V\right) + \int_S \vec{F}\mathrm{d}s \tag{6.1}$$

Euler's Law of Angular Motion:

$$\frac{\mathrm{d}}{\mathrm{d}t}\left[\int_V \vec{r'} \times \frac{\mathrm{d}\vec{r'}}{\mathrm{d}t}\left(\rho_\mathrm{A}\mathrm{d}V\right)\right] = \int_V \vec{r'} \times \vec{g}\left(\rho_\mathrm{A}\mathrm{d}V\right) + \int_s \vec{r'} \times \vec{F}\mathrm{d}s \tag{6.2}$$

In eq (6.1), the L.H.S. denotes the rate of change of linear momentum of the micro-flyer which is equated to the applied forces (Gravitational + Aerodynamic). Similarly in eq (6.2), the L.H.S. denotes the rate of change of angular momentum which is equated to the applied moments. In eq (6.1) and eq (6.2), $\vec{r'}$ is the position vector of a small elemental mass of volume $\mathrm{d}V$ and density ρ_A measured with respect to an inertial frame of reference. $\vec{g}$ is the acceleration vector due to gravity (assumed constant), $\vec{F}\mathrm{d}s$ represents the elemental surface forces (aerodynamics).

6.2 Micro-flyer Model

The flapping wing micro-flyer model shown in Fig. 6.1(a) is chosen as a system of three rigid bodies, a main body with two elliptical wings symmetrically attached to it. A fixed inertial frame of reference is defined. A body reference frame is defined which is attached to the center of gravity of the micro-flyer model. Similarly, a stroke plane frame and a wing frame are attached to each of the two wing roots of the model respectively. This ensures complete description of the motions of the body and wings relative to each other and to the inertial frame. The different frames are shown in Fig. 6.1.

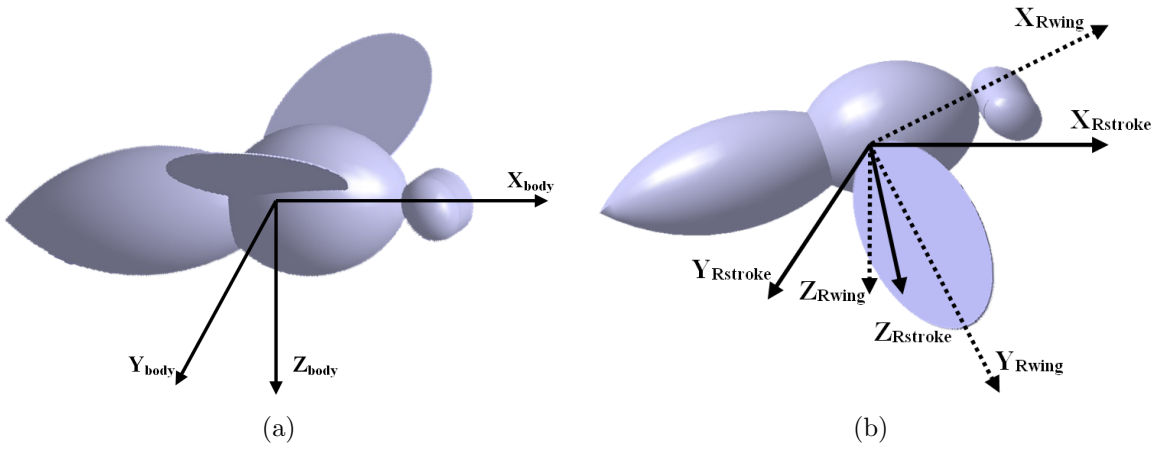

Figure 6.1. Micro-flyer model Reference Frames (a) body frame (b) Right stroke plane and wing frames.

The micro-flyer model is represented in the body frame using a standard 3-2-1 Euler angle rotation sequence with respect to the fixed inertial frame. This corresponds to a yaw-pitch-roll $(\Psi - \Theta - \Phi)$ rotation sequence, given by the rotation matrix to go from inertial to body frame, defined as

$$\mathbf{T_I^B} = \boldsymbol{\mathcal{R}_1}(\Phi)\boldsymbol{\mathcal{R}_2}(\Theta)\boldsymbol{\mathcal{R}_3}(\Psi), \tag{6.3}$$

where

$$\boldsymbol{\mathcal{R}_1}(a) = \begin{bmatrix} 1 & 0 & 0 \\ 0 & \cos a & -\sin a \\ 0 & \sin a & \cos a \end{bmatrix}, \; \boldsymbol{\mathcal{R}_2}(a) = \begin{bmatrix} \cos a & 0 & -\sin a \\ 0 & 1 & 0 \\ \sin a & 0 & \cos a \end{bmatrix}, \tag{6.4}$$

$$\boldsymbol{\mathcal{R}_3}(a) = \begin{bmatrix} \cos a & -\sin a & 0 \\ \sin a & \cos a & 0 \\ 0 & 0 & 1 \end{bmatrix}$$

'a' represents the appropriate rotation angle. As defined previously, the stroke plane is a plane about which the micro-flyer wings flap. The orientation of this plane with respect to the body frame is defined by two consecutive rotations, first about the stroke plane yaw angle '$\chi_{\mathrm{R,L}}$', and then about the stroke plane pitch angle $\theta_{\mathrm{S_{R,L}}}$. Subscripts 'R' and 'L' represent the left and right wing respectively. Positive rotations for the angles are determined using the right hand rule. The stroke plane yaw angle is positive when the stroke plane yaws away from the body. Similarly, the stroke plane pitch angle is positive when the plane pitches up. Fig 6.2(a) shows the right stroke plane yaw angle (positive), while Fig 6.2(b) shows the right stroke plane pitch angle (negative). The rotation matrix to go from body frame to the stroke plane frame is given by 3-2 sequence as

$$\mathbf{T_B^{S_{R,L}}} = \boldsymbol{\mathcal{R}_2}(\theta_{\mathrm{S_{R,L}}})\boldsymbol{\mathcal{R}_3}(\chi_{\mathrm{R,L}}) \tag{6.5}$$

The orientation of the wings with respect to the stroke plane is determined using the wing heave angle ($\beta_{\mathrm{R,L}}$), wing pitch angle ($\theta_{\mathrm{R,L}}$), and the wing flap angle ($\zeta_{\mathrm{R,L}}$). The wing pitch angle is measured from the stroke plane as shown in Fig. 6.2(b). The heaving and flapping angles are shown in Fig. 6.2(c) and Fig. 6.2(d) respectively. $\theta_{\mathrm{R,L}}$ is positive when the wing pitches up in the stroke plane frame. Similarly, a positive $\beta_{\mathrm{R,L}}$ is when the wing is deviated up and a positive $\zeta_{\mathrm{R,L}}$ when the wing is forward.

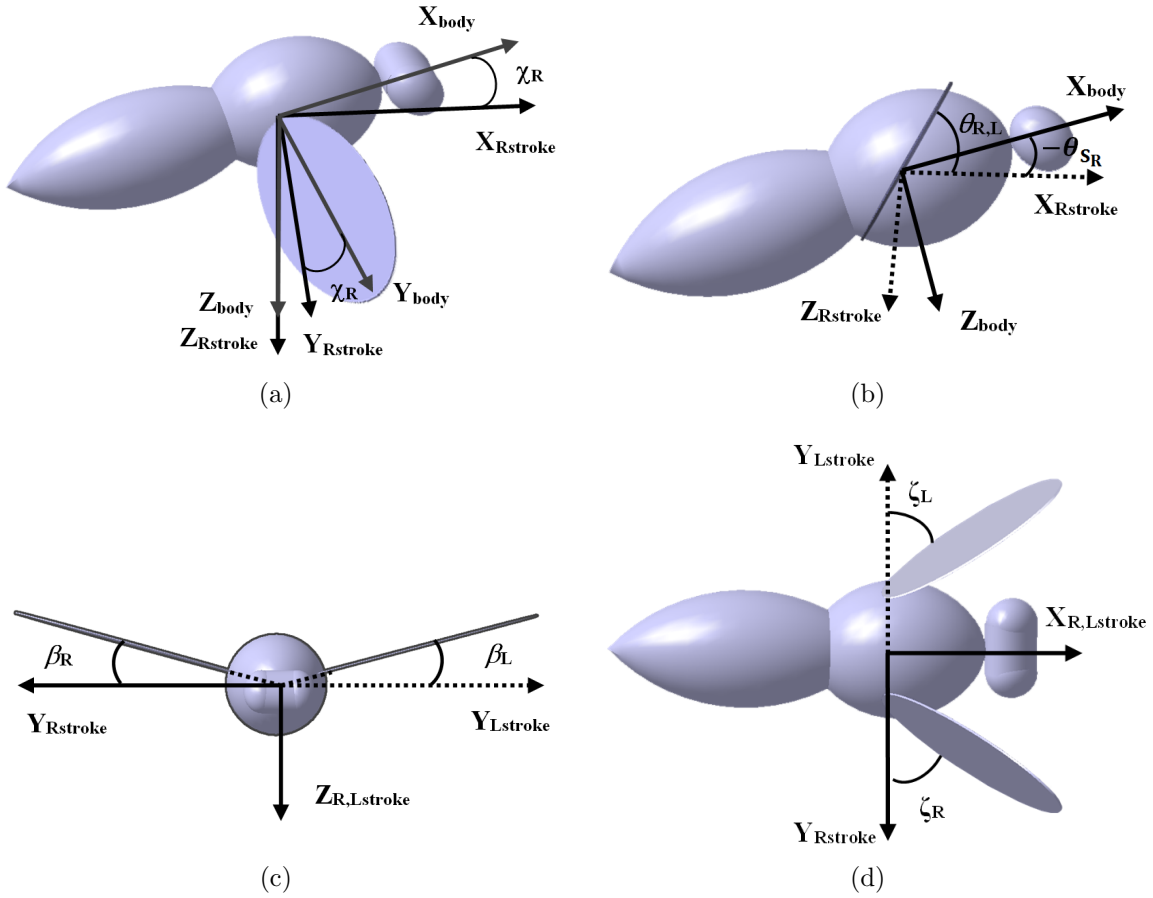

Figure 6.2. Different angles of flapping wing micro-flyer model (a) Right stroke plane yaw angle χ_{R} (b) Wing pitch angle $\theta_{\mathrm{R,L}}$ and right stroke plane pitch angle $\theta_{\mathrm{S_R}}$ (c) Wing heave angles β_{R} and β_{L} (d) Wing flap angles ζ_{R} and ζ_{L}.

The rotation matrix to go from stroke plane frame to wing frame is given by the 3-1-2 Euler angle sequence, i.e., $(\zeta) \rightarrow (\theta) \rightarrow (\beta)$. Appropriate subscripts are attached to denote the corresponding stroke plane frame. For example, the rotation matrix for the right wing with respect to the left stroke plane is

$$\mathbf{T}_{\mathbf{S_R}}^{\mathbf{W_R}} = \boldsymbol{\mathcal{R}}_{\mathbf{2}}(\beta_{\mathrm{R}})\boldsymbol{\mathcal{R}}_{\mathbf{1}}(\theta_{\mathrm{R}})\boldsymbol{\mathcal{R}}_{\mathbf{3}}(\zeta_{\mathrm{R}}) \tag{6.6}$$

The rotation matrix to go from left stroke plane to left wing frame, is similar to the eq (6.6). But the signs of ζ_{L} and β_{L} angles are opposite to that of ζ_{R} and β_{R} in order to balance aerodynamic forces and moments in the body frame for symmetric flapping.

6.3 Aerodynamic Forces and Moments Calculation

As described earlier, the forces and moments are developed on the body due to the motion of the wings. The aerodynamic expressions used to calculate these forces are obtained from the CFD simulation runs. For these runs, a 2D wing is flapped in a way that the forces will be observed in the stroke plane frame. Moreover, the forces obtained are the averages of the total forces obtained over each flapping cycle, since the aerodynamic model used in the calculation consists of cycle-averaged expressions for force coefficients.For the calculation of the forces, the wing is divided

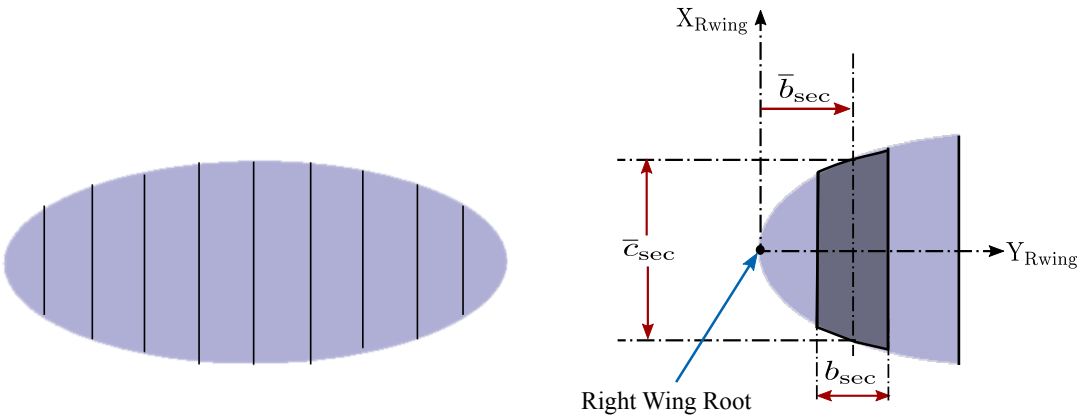

(a) (b)

Figure 6.3. (a) Micro-flyer wing divided into multiple sections (b) Semi-span and chord length defined for each section.

into multiple sections and the mean values of semi-span and chord length for each of the sections is determined as depicted in Fig. 6.3(a). The cycle-averaged vertical and

horizontal forces due to each of the individual wing sections in the stroke plane frame are calculated by

$$\begin{aligned} \mathrm{d}F_{\mathrm{ZavgS_{R,L}}} &= -\tfrac{1}{2}\rho\left(f\bar{b}_{\mathrm{sec}}\right)^2 C_{\mathrm{Zavg}}\bar{c}_{\mathrm{sec}}b_{\mathrm{sec}} \\ \mathrm{d}F_{\mathrm{XavgS_{R,L}}} &= -\tfrac{1}{2}\rho\left(f\bar{b}_{\mathrm{sec}}\right)^2 C_{\mathrm{Xavg}}\bar{c}_{\mathrm{sec}}b_{\mathrm{sec}}, \end{aligned} \tag{6.7}$$

where $\bar{b}_{\mathrm{sec}}$ is the micro-flyer sectional mean semi-span measured from wing root, $\bar{c}_{\mathrm{sec}}$ is the micro-flyer sectional mean wing chord length and b_{sec} is the semi-span of each section as shown in Fig. 6.3(b). The term '$f\bar{b}_{\mathrm{sec}}$' is essentially the local velocity due to wing flapping. C_{Zavg} & C_{Xavg} are the cycle-averaged vertical and horizontal force coefficients respectively given by the aerodynamic model(described in the next section). The negative signs in eq (6.7) are due to the fact that the computational technique adopted to determine these expressions uses the Eulerian frame, which defines the reference frame in a sense opposite to the Lagrangian frame (see Fig. 6.4). The sectional average forces acting on the wing are given by

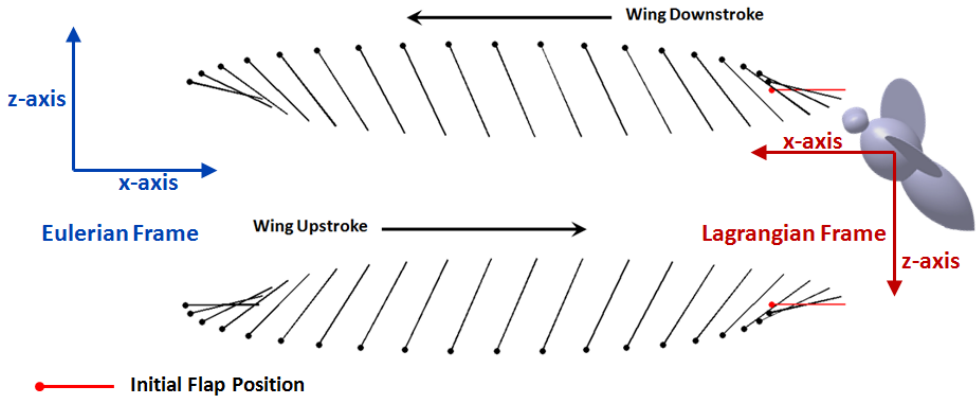

Figure 6.4. Eulerian and Lagrangian frames for a micro-flyer flapping in straight path.

$$\mathrm{d}\vec{F}_{\mathrm{avgS_{R,L}}} = \begin{bmatrix} \mathrm{d}F_{\mathrm{XavgS_{R,L}}} \\ 0 \\ \mathrm{d}F_{\mathrm{ZavgS_{R,L}}} \end{bmatrix} \tag{6.8}$$

and the corresponding sectional average moments are given by

$$\mathrm{d}\vec{M}_{\mathrm{avgS_{R,L}}} = \vec{r}_{\mathrm{R,L}} \times \mathrm{d}\vec{F}_{\mathrm{avgS_{R,L}}} \tag{6.9}$$

where $\vec{r}_{\mathrm{R,L}}$ is the position vector from the body center of gravity to the center of the sectional semi-span expressed in the stroke plane frame. As shown in Fig. 6.5,

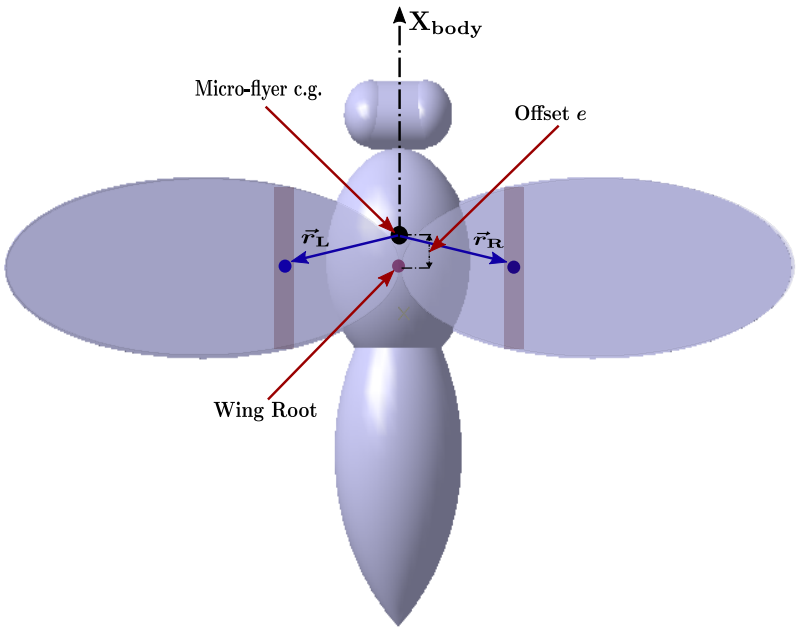

Figure 6.5. Position vector $\vec{r}_{\mathrm{R,L}}$ for calculating aerodynamic moments.

depending on the right or left wing root, this vector is defined as

$$\vec{r}_{\mathrm{R,L}} = \left[\mathbf{T}^{\mathbf{W_{R,L}}}_{\mathbf{S_{R,L}}}\right]^{\mathrm{T}} \begin{bmatrix} 0 \\ \bar{b}_{\mathrm{sec}} \\ 0 \end{bmatrix} + \left[\mathbf{T}^{\mathbf{S_{R,L}}}_{\mathbf{B}}\right] \begin{bmatrix} e \\ 0 \\ 0 \end{bmatrix} \tag{6.10}$$

where e is the offset between body center of gravity and wing root. For the calculation of the position vector, the sectional semi-span $\bar{b}_{\text{sec}}$ is measured negative for the left wing and positive for the right wing. The sectional average forces and moments are summed along the entire wing to get the average aerodynamic forces and moments due to each wing in the stroke plane frame. The average forces are given by

$$\vec{F}_{\text{avgS}_{\text{R,L}}} = \frac{1}{N} \sum_{N} \mathrm{d}\vec{F}_{\text{avgS}_{\text{R,L}}} \tag{6.11}$$

and the corresponding average moments are given by

$$\vec{M}_{\text{avgS}_{\text{R,L}}} = \frac{1}{N} \sum_{N} \mathrm{d}\vec{M}_{\text{avgS}_{\text{R,L}}} \tag{6.12}$$

where N is the number of wing sections. Therefore, the cycle-averaged body forces are then given by

$$\vec{F}_{\text{avg}} = \left[\mathbf{T}_{\mathbf{B}}^{\mathbf{S_R}}\right]^{\text{T}} \vec{F}_{\text{avgS}_{\text{R}}} + \left[\mathbf{T}_{\mathbf{B}}^{\mathbf{S_L}}\right]^{\text{T}} \vec{F}_{\text{avgS}_{\text{L}}} \tag{6.13}$$

Similarly, the cycle-averaged moments in the body frame are given by

$$\vec{M}_{\text{avg}} = \left[\mathbf{T}_{\mathbf{B}}^{\mathbf{S_R}}\right]^{\text{T}} \vec{M}_{\text{avgS}_{\text{R}}} + \left[\mathbf{T}_{\mathbf{B}}^{\mathbf{S_L}}\right]^{\text{T}} \vec{M}_{\text{avgS}_{\text{L}}} \tag{6.14}$$

6.4 Aerodynamic Model

The aerodynamic model used in the flight dynamics is based on the methodology described earlier to numerically determine the preliminary expressions for cycle-averaged force coefficients for a straight flapping path by conducting response surface methodology (sec. 2.2) over Design of Experiments (DOE). In that case, the aerodynamic expressions were functions of the local Reynolds number, the Strouhal number and the stroke angle of attack while keeping the geometric function constant. For this model two changes are made. Firstly, the geometric function is included as a fourth

parameter. Secondly, instead of the Strouhal number, Inverse Strouhal number Sr is used, which is defined in terms of micro-flyer variables as

$$Sr = \frac{V}{f\bar{b}_{\text{sec}}} = \frac{1}{St}, \tag{6.15}$$

where V is the magnitude of the micro-flyer body velocity given by

$$\vec{V} = u\hat{i} + v\hat{j} + w\hat{k} \tag{6.16}$$

Using the Inverse Strouhal number facilitates in avoiding a singularity during the implementation of the hovering flight dynamics, for which the body velocity is zero making the Strouhal number (St) infinite. It is to be noted that in the absence of wind, the body velocity is the free stream velocity that the wing experiences.

All the non-dimensional parameters are defined in the terms of micro-flyer variables. The local Reynolds number defined as

$$Re_{\text{l}} = \frac{\rho f \bar{c}_{\text{sec}} \bar{b}_{\text{sec}}}{\mu} \tag{6.17}$$

The geometric function defined as

$$G = \frac{\bar{c}_{\text{sec}}}{\bar{b}_{\text{sec}}} \tag{6.18}$$

Finally, the stroke angle of attack is defined as the angle made by the wing stroke plane with respect to the body velocity vector. So

$$\alpha_{\text{S}} = \alpha + \theta_{\text{S}}, \tag{6.19}$$

where α is the body angle of attack and is defined as

$$\alpha = \tan^{-1}\left(\frac{w}{u}\right) \tag{6.20}$$

The values used for all the DOE parameters are given in Tab. 6.1. The approximated

Table 6.1. Parameter values for aerodynamic model

Parameter	Re_{l}	Sr	α_{S} (rad)	G
maximum	31.88	28.5	$5\pi/180$	3.49
mean	16.48	14.25	0	1.84
minimum	1.07	0.003	$-5\pi/180$	0.18

expressions are given by

$$\begin{aligned} C_{\mathrm{Zavg}} &= 2.03Re_{\mathrm{l}} - 0.05{Re_{\mathrm{l}}}^2 - 136.03G + 77.8G^2 + 3.04Re_{\mathrm{l}}G \\ &+ 0.83SrG - 0.004Re_{\mathrm{l}}Sr + 0.5Sr - 0.003Sr^2 + 33.08Sr\alpha_{\mathrm{S}}, \end{aligned} \tag{6.21}$$

and

$$C_{\mathrm{Xavg}} = 59.91SrG + 0.17Re_{\mathrm{l}}Sr - 15.64Sr + 0.54Sr^2 \tag{6.22}$$

6.4.1 Micro-flyer Body Drag

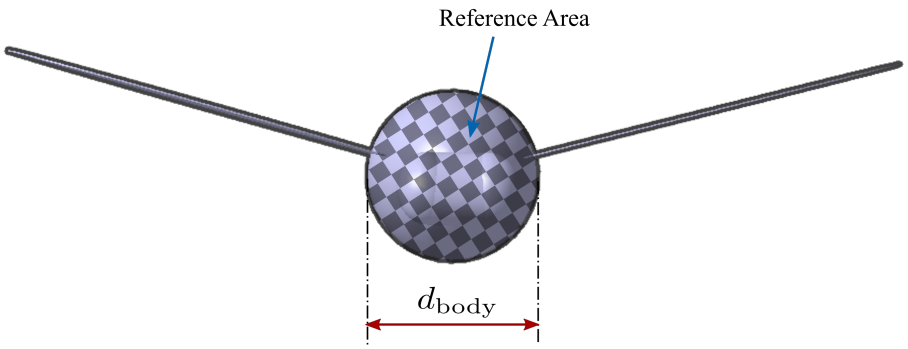

Figure 6.6. Reference area (checkered region) to calculate micro-flyer body drag.

Drag force due to micro-flyer body is calculated. The micro-flyer body is assumed to be equivalent to a sphere, with a diameter d_{body} equal to the largest cross-sectional length of the micro-flyer body, as shown in Fig. 6.6. The frontal or reference

area of the body is the cross-sectional area of the sphere (checkered region in the figure). The micro-flyer body drag force is defined as

$$D_{\text{body}} = \frac{1}{2}\rho V^2 C_{\text{Dbody}} A_{\text{ref}} \tag{6.23}$$

where A_{ref} is the reference area calculated as

$$A_{\text{ref}} = \frac{\pi}{4} d_{\text{body}}^2 \tag{6.24}$$

and C_{Dbody} is the body drag coefficient. The free stream Reynolds number for the micro-flyer flight is found to be in the region of 10-100. So the drag coefficient value for the body is fixed to be 1.5 based on the C_{D}-Re_{∞} curve given in [63]. The body drag has components in x and z-directions, defined as

$$D_{\text{Xbody}} = D_{\text{body}} \cos\alpha, \quad D_{\text{Zbody}} = D_{\text{body}} \sin\alpha \tag{6.25}$$

The body drag vector is assumed to be acting at the micro-flyer center of gravity.

6.5 Governing Equations of Motion

While deriving the equations of motion for the micro-flyer, the wing inertia effects on the micro-flyer body are neglected under the 'rigid body' assumption, which means that the micro-flyer has six degrees of freedom like a conventional aircraft. The effects of flapping wings are accounted for through flapping cycle-averaged aerodynamic forces and moments, that are time-varying over the body time scale.

Sun et al. [64] presented the conditions under which this assumption holds true. They derived the equations of motion by considering the wing inertial forces and the variation of the center of gravity during the flapping cycle. The translation and rotational dynamic equations were given as

$$\begin{aligned} {}_{\text{b}}\mathbf{F}_{\text{A}} + m_{\text{bdb}}\mathbf{g} &= m_{\text{bdb}} \left({}_{\text{b}}\dot{\mathbf{V}}_{\text{cg}} + {}_{\text{b}}\boldsymbol{\omega}_{\text{bd}} \times {}_{\text{b}}\mathbf{V}_{\text{cg}} \right) + \mathbf{a}_1 + \mathbf{b}_1 \\ {}_{\text{b}}\mathbf{M}_{\text{A}} &= ({}_{\text{b}}\boldsymbol{\omega}_{\text{bd}} \times {}_{\text{b}}\mathbf{I}_{\text{bdb}}\boldsymbol{\omega}_{\text{bd}}) + {}_{\text{b}}\mathbf{I}_{\text{bdb}}\dot{\boldsymbol{\omega}}_{\text{bd}} + \mathbf{a}_2 + \mathbf{b}_2 \end{aligned} \tag{6.26}$$

where ${}_{\mathrm{b}}\mathbf{F}_{\mathrm{A}}$ and ${}_{\mathrm{b}}\mathbf{M}_{\mathrm{A}}$ are the aerodynamic forces and moments expressed in body frame as denoted by left subscript b, m_{bdb} is the body mass, and ${}_{\mathrm{b}}\mathbf{I}_{\mathrm{bd}}$ is the body inertia matrix. The vector $\mathbf{a}_1$ represents the wing weight and the wing inertial forces due to body acceleration and rotation, while $\mathbf{a}_2$ represents the corresponding moments. Vectors $\mathbf{b}_1$ and $\mathbf{b}_2$ represent the inertial forces and moments of the wings due to flapping motion. Vectors $\mathbf{a}_1$ and $\mathbf{a}_2$ can be neglected where the wing mass is much less than the body mass. For the present research, the wing mass is less than 3% of the body mass, and hence these vectors can be neglected.

It was stated further that if the flapping frequency is relatively high (f >150 Hz), so that the time scale of the flapping motion ($1/f$) is much smaller than that of the body motion, then one can take the average of eq (6.26) over one flapping cycle to average out the fast motion and represent the equations in terms of the slower time cycle. Rewriting each variable in the equations as $\mathrm{x} = \overline{\mathrm{x}} + \hat{\mathrm{x}}$, where $\overline{\mathrm{x}}$ is the cycle-averaged value and $\hat{\mathrm{x}}$ is the difference between instantaneous and cycle-averaged values, we get

$$\begin{aligned} {}_{\mathrm{b}}\overline{\mathbf{F}}_{\mathrm{A}} + m_{\mathrm{bdb}}\mathbf{g} &= m_{\mathrm{bdb}}\left({}_{\mathrm{b}}\dot{\overline{\mathbf{V}}}_{\mathrm{cg}} + {}_{\mathrm{b}}\overline{\boldsymbol{\omega}}_{\mathrm{bd}} \times {}_{\mathrm{b}}\overline{\mathbf{V}}_{\mathrm{cg}} + \overline{{}_{\mathrm{b}}\hat{\boldsymbol{\omega}}_{\mathrm{bd}} \times {}_{\mathrm{b}}\hat{\mathbf{V}}_{\mathrm{cg}}}\right) + \overline{\mathbf{b}}_1 \\ {}_{\mathrm{b}}\overline{\mathbf{M}}_{\mathrm{A}} &= \left({}_{\mathrm{b}}\overline{\boldsymbol{\omega}}_{\mathrm{bd}} \times {}_{\mathrm{b}}\mathbf{I}_{\mathrm{bdb}}\overline{\boldsymbol{\omega}}_{\mathrm{bd}} + \overline{{}_{\mathrm{b}}\hat{\boldsymbol{\omega}}_{\mathrm{bd}} \times {}_{\mathrm{b}}\mathbf{I}_{\mathrm{bdb}}\hat{\boldsymbol{\omega}}_{\mathrm{bd}}}\right) + {}_{\mathrm{b}}\mathbf{I}_{\mathrm{bdb}}\dot{\overline{\boldsymbol{\omega}}}_{\mathrm{bd}} + \overline{\mathbf{b}}_2 \end{aligned} \tag{6.27}$$

In order to reduce the above equations to standard 6 DOF equations of motion of aircraft, the terms $\overline{{}_{\mathrm{b}}\hat{\boldsymbol{\omega}}_{\mathrm{bd}} \times {}_{\mathrm{b}}\hat{\mathbf{V}}_{\mathrm{cg}}}$, $\overline{{}_{\mathrm{b}}\hat{\boldsymbol{\omega}}_{\mathrm{bd}} \times {}_{\mathrm{b}}\mathbf{I}_{\mathrm{bdb}}\hat{\boldsymbol{\omega}}_{\mathrm{bd}}}$, $\overline{\mathbf{b}}_1$ and $\overline{\mathbf{b}}_2$ should be eliminated. Sun et al. performed longitudinal flight dynamic simulations by generating forces using CFD to compute the values of the product terms. They found that the order of each of the product terms is 10^{-2}, thereby making the order of the product term 10^{-4}, while the order of the acceleration terms is 10^{-1}. So the product terms can be neglected. Vectors $\overline{\mathbf{b}}_1$ and $\overline{\mathbf{b}}_2$, which represent the cycle-averaged inertial forces and moments of the wings due to flapping motion, were found to be of the order 10^{-6}.

This is because if the upstroke and downstroke are symmetric, the inertial forces and moments generated during flapping cancel each other out. So it is essential to have symmetric flapping for the rigid body assumption to hold true. It is also to be noted that elimination of these terms is based on cycle averaging. So the wing inertial effects can be neglected so long as the cycle-averaging assumption is valid. Sun et al. in their conclusions noted that the rigid body assumption is reasonable for the insects with relatively high flapping frequency like hoverfly, dronefly and bumblebee. Flapping frequencies of all these insects is upwards of 150 Hz, which is the range the present research deals with. Also, the aerodynamic model is based on the straight flapping trajectory which has a symmetric upstroke and downstroke. So the rigid body assumption can be safely employed for the present research.

The equations of motion are now summarized for the flapping wing micro-flyer. The translational kinematics equation is given by

$$\dot{\vec{X}} = \left[\mathbf{T}_{\mathbf{I}}^{\mathbf{B}}\right]^{\mathrm{T}} \vec{V} \tag{6.28}$$

The translational dynamics equation is given by

$$\vec{F}_{\mathrm{avg}} - \vec{D}_{\mathrm{body}} + m_{\mathrm{total}} \mathbf{T}_{\mathbf{I}}^{\mathbf{B}} \vec{g} = m_{\mathrm{total}} \left(\dot{\vec{V}} + \vec{\Omega} \times \vec{V} \right), \tag{6.29}$$

where $m_{\mathrm{total}} = m_{\mathrm{body}} + m_{\mathrm{wingR}} + m_{\mathrm{wingL}}$, the total mass of the microflyer and $\vec{\Omega} = p\hat{i} + q\hat{j} + r\hat{k}$ is the angular velocity of the microflyer. The rotational kinematics equation is given by

$$\begin{bmatrix} \dot{\Phi} \\ \dot{\Theta} \\ \dot{\Psi} \end{bmatrix} = \begin{bmatrix} 1 & S_\Phi \tan\Theta & C_\Phi \tan\Theta \\ 0 & C_\Phi & -S_\Phi \\ 0 & S_\Phi \sec\Theta & C_\Phi \sec\Theta \end{bmatrix} \begin{bmatrix} p \\ q \\ r \end{bmatrix}, \tag{6.30}$$

where $S_\Phi = \sin\Phi,\ C_\Phi = \cos\Phi$. The rotational dynamics equation is given by

$$\vec{M}_{\mathrm{avg}} = \vec{\Omega} \times \mathbf{I}_{\mathbf{body}} \vec{\Omega} + \mathbf{I}_{\mathbf{body}} \dot{\vec{\Omega}}, \tag{6.31}$$

Table 6.2. Body inertia tensor of micro-flyer model

Inertia I_{Bii}	Value in gm-cm^2
I_{Bxx}	3×10^{-6}
I_{Byy}	12×10^{-6}
I_{Bzz}	13×10^{-6}
I_{Bxy}	0
I_{Byz}	0
I_{Bxz}	-4.36488×10^{-8}

where $\mathbf{I_{body}}$ is the moment of inertia tensor of the body. The values of the body inertia tensor were obtained from a cad model based on *Drosophila* (fruit-fly) given in [47], and are listed in Tab. 6.2.

6.5.1 Longitudinal Flight Dynamics

For the flight dynamics analysis, the cycle-averaged aerodynamic model is implemented with a reduced order longitudinal dynamics of the flapping wing micro-flyer. Equations of motion for the longitudinal dynamics are given as follows.

$$\begin{aligned}
\dot{u} &= -qw - g\sin\Theta + \tfrac{1}{m_{\text{total}}}\left(F_{\text{Xavg}} - D_{\text{Xbody}}\right)\\
\dot{w} &= qu + g\cos\Theta + \tfrac{1}{m_{\text{total}}}\left(F_{\text{Zavg}} - D_{\text{Zbody}}\right)\\
\dot{\Theta} &= q\\
\dot{q} &= \tfrac{M_{\text{Yavg}}}{I_{\text{Byy}}}\\
\dot{x} &= u\cos\Theta + w\sin\Theta\\
\dot{z} &= -u\sin\Theta + w\cos\Theta
\end{aligned} \tag{6.32}$$

where Θ is the micro-flyer body pitch angle and q is the body pitch rate.

6.6 Simulation Parameters

The wing flap angle of the wing is given by

$$\zeta(t) = \zeta_0 + \zeta_1 \sin(\omega t), \tag{6.33}$$

where $\omega = 2\pi f$. The stroke amplitude of a fruit-fly is 160 deg. Therefore $\zeta_1 = 80$ deg. Also, since the angles are defined in accordance with the straight flapping trajectory used in the flow simulations, the flapping starts with an offset angle of $\zeta_0 = -80$ deg, which corresponds to start of the downstroke. The wing heave angle is given by

$$\beta(t) = \beta_0 + \beta_1 \sin\left(2\omega t - \frac{\pi}{2}\right) \tag{6.34}$$

The wing heave angle is set at 0 deg for the simulation runs. The wing pitch angle is given by

$$\theta(t) = \theta_0 + \theta_1 \sin(\omega t) \tag{6.35}$$

where θ_1 is taken as 60 deg and θ_0 is set to 0. The properties of the micro-flyer model are based on *Drosophila*, and are listed in Tab. 6.3.

Table 6.3. Properties of micro-flyer model

Property	Value
Mass of body, m_{body}	1736×10^{-6} g
Mass of each wing, $m_{\text{wingR,L}}$	57×10^{-6} g
Wing semi-span, b	0.3 cm
Wing maximum chord, $c_{\max}$	0.12 cm
Body diameter, d_{body}	0.11 cm
Offset, e	-0.001 cm

6.7 Closed-Loop Control of Micro-flyer

Steady-state flight conditions for the micro-flyer with the given aerodynamic model are determined using trim analysis. Appropriate trim conditions are applied to see if a particular steady-state flight condition is met. The nonlinear flight dynamics model is then linearized about that trim point and linear systems analysis is performed. A linear controller is developed and tested on the nonlinear model. Results for open loop and closed loop systems are then compared.

6.7.1 Trim Analysis

Authors in [65] state that a set of flight dynamics equations can be generalized by an implicit form

$$\mathbf{f}\left(\dot{\mathbf{X}}, \mathbf{X}, \mathbf{U}\right) = 0, \tag{6.36}$$

where $\mathbf{f}$ is a vector of n scalar nonlinear functions f_i $(i = 1, \ldots, n)$. $\mathbf{X}$ is the state vector and $\mathbf{U}$ is the input vector. The concept of an 'equilibrium point' or 'trim point' for an autonomous time-invariant system given by eq (6.36) is introduced in the theory of nonlinear systems [66]. It states that the trim point of a set of a implicit nonlinear system of equations given by the solution vector, $\mathbf{X} = \mathbf{X_e}$ satisfies

$$\mathbf{f}\left(\dot{\mathbf{X}}, \mathbf{X}, \mathbf{U}\right) = 0, \quad \text{with} \;\; \dot{\mathbf{X}} \equiv 0; \;\; \mathbf{U} \equiv 0 \text{ or } \mathbf{U_e} \tag{6.37}$$

$\mathbf{U_e}$ is defined as the trim control input required to achieve the steady-state flight. Eq. (6.37) implies that for a system to achieve a particular steady-state, derivatives of all the states need to be identically zero. So the linear and angular velocities are constant or zero, while the accelerations are zero.

Three steady-state flight conditions are checked for the micro-flyer longitudinal flight dynamics with the prescribed aerodynamic model. They are *hover*, *straight* &

level, and *steady climb/descent*. The equation constraints for each of the three cases are as follows.

i. Hover: $\dot{\mathbf{X}} = \left[\dot{u},\ \dot{w},\ \dot{\Theta},\ \dot{q},\ \dot{x},\ \dot{z}\right]^{\mathrm{T}} \equiv 0$ (n=6)

ii. Straight & Level: $\dot{\mathbf{X}} = \left[\dot{u},\ \dot{w},\ \dot{\Theta},\ \dot{q},\ \dot{z}\right]^{\mathrm{T}} \equiv 0$ (n=5)

iii. Steady Climb/Descent: $\dot{\mathbf{X}} = \left[\dot{u},\ \dot{w},\ \dot{\Theta},\ \dot{q}\right]^{\mathrm{T}} \equiv 0$ (n=4)

Trim point $(\mathbf{X_e}, \mathbf{U_e})$ for a steady-state flight condition is obtained by numerically solving an constrained optimization problem where a cost function is minimized for a given set of bounds for states and control inputs. This cost function is given by

$$\mathcal{J} = \dot{\mathbf{X}}^{\mathrm{T}}\dot{\mathbf{X}} \tag{6.38}$$

Recall that the aerodynamic model uses the flapping frequency and the stroke angle of attack to generate aerodynamic forces and moments. However, it is known from eq (6.19) the stroke angle of attack itself is a function of the stroke plane pitch angle. So the control input vector is defined as

$$\mathbf{U} = [f, \theta_{\mathrm{S}}]^{\mathrm{T}} \tag{6.39}$$

The upper and lower bounds for states and control inputs are given as

$$\begin{aligned} \mathbf{X_{LB}} \leq \mathbf{X} \leq \mathbf{X_{UB}} \\ \mathbf{U_{LB}} \leq \mathbf{U} \leq \mathbf{U_{UB}} \end{aligned} \tag{6.40}$$

The analysis did not yield any trim points for hover and straight & level flight conditions. However a trim point was determined for the steady descent flight. This means that the micro-flyer can only perform a trimmed descent using the given aerodynamic model. The values of the trim point are given in Tab. 6.4.

Table 6.4. Trim point $(\mathbf{X_e}, \mathbf{U_e})$ for steady descent

Variable	u_e cm/s	w_e cm/s	Θ_e deg	q_e rad/s	f_e Hz	θ_{Se} deg
Value	34.26	19.86	-22.7	-0.04	277.017	-62.4

6.7.2 System Linearization

The longitudinal nonlinear flight dynamic model given in eq (6.32) is linearized about the trim point obtained for the steady descent flight condition. The linearized model is of the form

$$\mathbf{\Delta \dot{X}} = \mathbf{A\Delta X} + \mathbf{B\Delta U}, \tag{6.41}$$

where $\mathbf{A} \in \mathbb{R}^{4\times4}$ and $\mathbf{B} \in \mathbb{R}^{4\times2}$ are the numerically computed 'Jacobian' matrices given by

$$\mathbf{A} = \left.\frac{\partial \mathbf{f}}{\partial \mathbf{X}}\right|_{(\mathbf{X_e},\mathbf{U_e})}, \quad \mathbf{B} = \left.\frac{\partial \mathbf{f}}{\partial \mathbf{U}}\right|_{(\mathbf{X_e},\mathbf{U_e})} \tag{6.42}$$

The perturbations in eq (6.41) are defined as

$$\mathbf{\Delta X} = \mathbf{X} - \mathbf{X_e}, \quad \mathbf{\Delta U} = \mathbf{U} - \mathbf{U_e} \tag{6.43}$$

and the output vector is

$$\mathbf{\Delta Y} = \mathbf{\Delta X} \tag{6.44}$$

$\mathbf{A}$ and $\mathbf{B}$ matrices are found to be

$$\mathbf{A} = \begin{bmatrix} -32.37 & 7.80 & -905.16 & -19.86 \\ -7.72 & -18.41 & 378.22 & 34.26 \\ 0 & 0 & 0 & 1 \\ 710.2 & -438.85 & 0 & 0 \end{bmatrix}, \quad \mathbf{B} = \begin{bmatrix} -1.43 & 4.59 \\ -3.89 & -99.25 \\ 0 & 0 \\ 45.63 & -29081.8 \end{bmatrix} \tag{6.45}$$

The eigen values of $\mathbf{A}$ matrix are

$$\lambda = -0.79 \pm j170.57, \ \& \ -24.6 \pm j4.42 \tag{6.46}$$

6.7.3 Linear Control Design

In order to design a control law for the linearized system, its controllability is checked using the Popov-Belevitch-Hautus (PBH) rank test [67–69], which is stated as follows:

Definition 1. *The pair* $(\mathbf{A}, \mathbf{B})$ *is controllable if and only if* $[\lambda\mathbf{I} - \mathbf{A} \quad \mathbf{B}] = n$ *for all* $\lambda \in \mathbb{C}$

Applying the PBH test to the linearized system, it is found that the obtained pair of Jacobian matrices is controllable. For the control design, a Linear Quadratic Regulator (LQR) method is implemented. This technique determines the optimal feedback gains for the system by minimizing a quadratic cost function given by

$$J = \frac{1}{2}\int_0^\infty \left(\mathbf{\Delta X}^{\mathrm{T}}\mathbf{Q}\mathbf{\Delta X} + \mathbf{\Delta U}^{\mathrm{T}}\mathbf{R}\mathbf{\Delta U}\right) \mathrm{d}\tau, \tag{6.47}$$

where $\mathbf{Q} \in \mathbb{R}^{4\times4}$ is a positive-semi-definite Hermitian or real symmetric matrix and $\mathbf{R} \in \mathbb{R}^{2\times2}$ is a positive-definite Hermitian or real symmetric matrix. $\mathbf{Q}$ and $\mathbf{R}$ are used as weighting matrices to determine the relative importance of the states and control inputs respectively and are appropriately tuned to get the desired result. The control law is given by

$$\mathbf{\Delta U} = -\mathbf{K_{opt}}\mathbf{\Delta X} \tag{6.48}$$

$\mathbf{K_{opt}}$ is the optimal gain matrix given by

$$\mathbf{K_{opt}} = \mathbf{R}^{-1}\mathbf{B}^{\mathrm{T}}\mathbf{P} \tag{6.49}$$

where $\mathbf{P}$ is the unique positive definite solution to the Algebraic Riccati Equation (ARE)

$$\mathbf{A}^{\mathrm{T}}\mathbf{P} + \mathbf{P}\mathbf{A} - \mathbf{P}\mathbf{B}\mathbf{R}^{-1}\mathbf{B}^{\mathrm{T}}\mathbf{P} + \mathbf{Q} = 0 \tag{6.50}$$

For the control design, the $\mathbf{Q}$ matrix is selected based on Bryson's rule [70] such that

$$\mathbf{Q_{ii}} = \frac{1}{\max(\mathbf{\Delta X_i^2})}, \quad \mathbf{i} = 1, \ldots, 4 \tag{6.51}$$

The $\mathbf{Q}$ and $\mathbf{R}$ matrices are given in eq (6.52).

$$\mathbf{Q} = \begin{bmatrix} \frac{1}{0.1^2} & 0 & 0 & 0 \\ 0 & \frac{1}{0.1^2} & 0 & 0 \\ 0 & 0 & \frac{1}{(0.5\pi/180)^2} & 0 \\ 0 & 0 & 0 & \frac{1}{3^2} \end{bmatrix}, \quad \mathbf{R} = \begin{bmatrix} 1 & 0 \\ 0 & 10000 \end{bmatrix} \tag{6.52}$$

The optimal gain matrix is found to be

$$\mathbf{K_{opt}} = \begin{bmatrix} -3.4198 & -3.5179 & 67.548 & 0.1712 \\ -0.0238 & -0.0644 & -0.5582 & -0.0149 \end{bmatrix} \tag{6.53}$$

The closed loop state matrix $\mathbf{A_{cl}} = \mathbf{A} - \mathbf{BK_{opt}}$ is given in eq (6.54).

$$\mathbf{A_{cl}} = \begin{bmatrix} -37.37 & 3.062 & -805.86 & -19.55 \\ -18.65 & -38.4773 & 585.26 & 33.44 \\ 0 & 0 & 0 & 1 \\ 1557.4 & -2152.4 & -19315.4 & -441.75 \end{bmatrix} \tag{6.54}$$

The closed loop eigen values are

$$\lambda_{\text{cl}} = -224.41 \pm j272.54, \ \& \ -34.39 \pm j7.15 \tag{6.55}$$

6.7.4 Nonlinear Dynamics Open and Closed Loop Simulations

The designed LQR controller is implemented in the nonlinear longitudinal dynamics framework. For the open loop simulations, the controls inputs are fixed to be the trim input values obtained earlier and given in Tab. 6.4. For the closed loop simulations, the control law is derived by substituting eq (6.48) in eq (6.43), and rearranging terms to solve for $\mathbf{U}$. The control law is given by

$$\mathbf{U} = \mathbf{K_{opt}} \left(\mathbf{X_e} - \mathbf{X} \right) + \mathbf{U_e} \tag{6.56}$$

For both open and closed loop simulations, the time step size of the simulation is taken as inverse of the flapping frequency $1/f$. This ensures that the average forces are calculated after each flapping cycle. These forces are used as inputs to the nonlinear dynamics and thus the system is propagated after each flapping cycle to get cycle-averaged motion of the micro-flyer.

ODE4 Runge-Kutta fixed time-step solver is used to perform all the simulations in MATLAB/Simulink. For open loop simulations, the flapping frequency remains at a constant trim value in turn maintaining a constant time-step for the entire simulation length. For the closed loop simulations however, the time-step may change after every flapping cycle, depending upon the controller to provide an appropriate flapping frequency input to the system every time the system propagation happens. Additionally, for the closed loop simulations, the control inputs are saturated so as to prevent the input values from going beyond the accepted values of each of the corresponding inputs. The saturation limits are set as

$$150 < f < 1000 \text{ (Hz)}, \quad -\pi/2 < \theta_{\mathrm{S}} < \pi/2 \text{ (rad)} \tag{6.57}$$

The results for open and closed loop simulations are plotted on the same graph. The micro-flyer is assumed to be initially descending from a height of 5 meters, with the body velocities, pitch angle and pitch rate set to trim values. Figure 6.7 shows the inertial positions and velocities of the micro-flyer. We can see that the inertial velocities seem to stabilize in quick time. From Fig. 6.8 we see that the micro-flyer descending to a height of around 3.3 meters by the end of simulation time, while moving ahead in x-direction by 1.3 meters.

At this point, both open loop and closed loop simulations seem to be yielding same results. However, Fig. 6.9 shows the micro-flyer body velocities converging to trim values at a much faster rate for closed loop simulation than for open loop with

much less transient amplitude. Figure 6.10 shows similar behavior with the pitching angle as well as the pitching rate converging faster for the closed loop. Similarly, we can see from Fig. 6.11 that the closed loop does a better job at stabilizing the cycle-averaged forces to a finite value while making pitching moment go to zero. Figure 6.12 shows that the frequency input for the closed loop settles at slightly higher value than constant trim frequency input value for open loop. The closed loop stroke plane pitch angle value is equal to that of open loop.

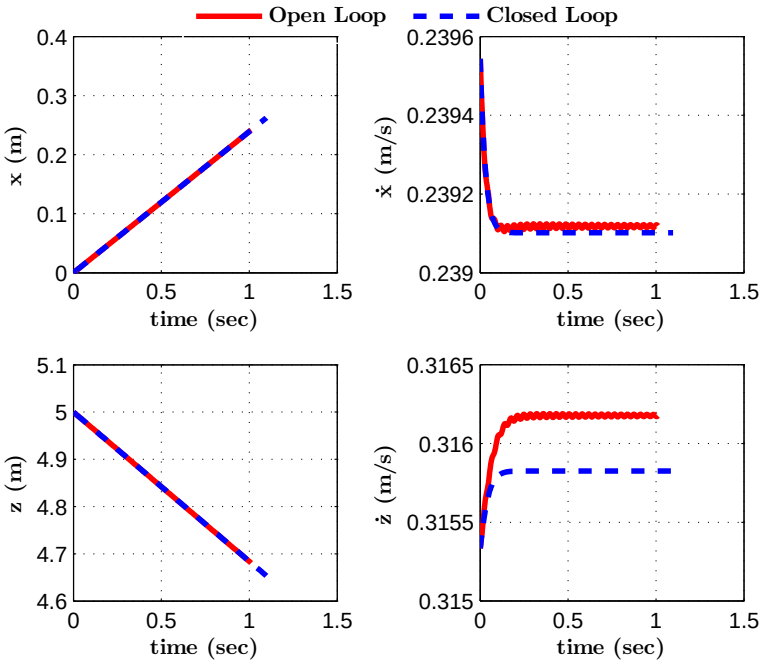

Figure 6.7. Inertial positions and velocities.

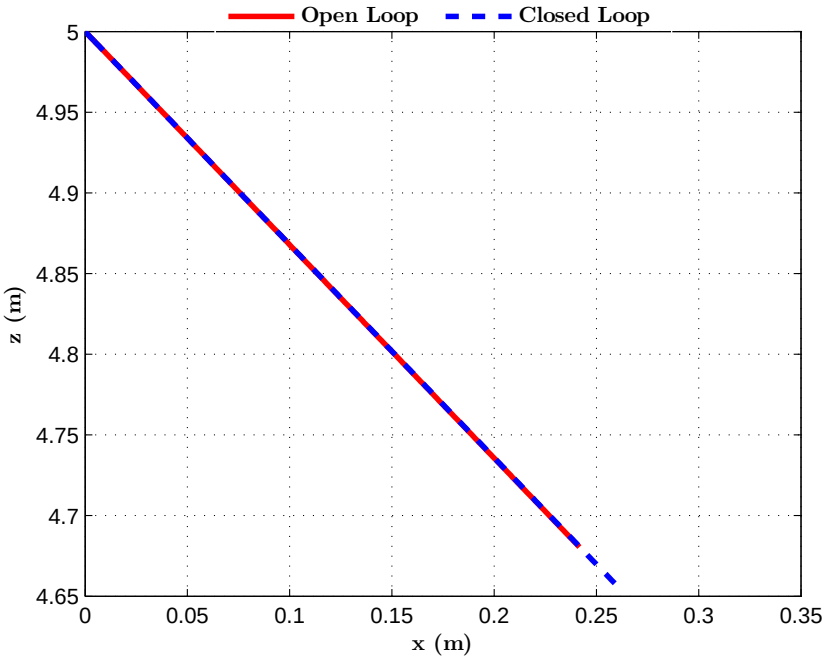

Figure 6.8. x-z position plot.

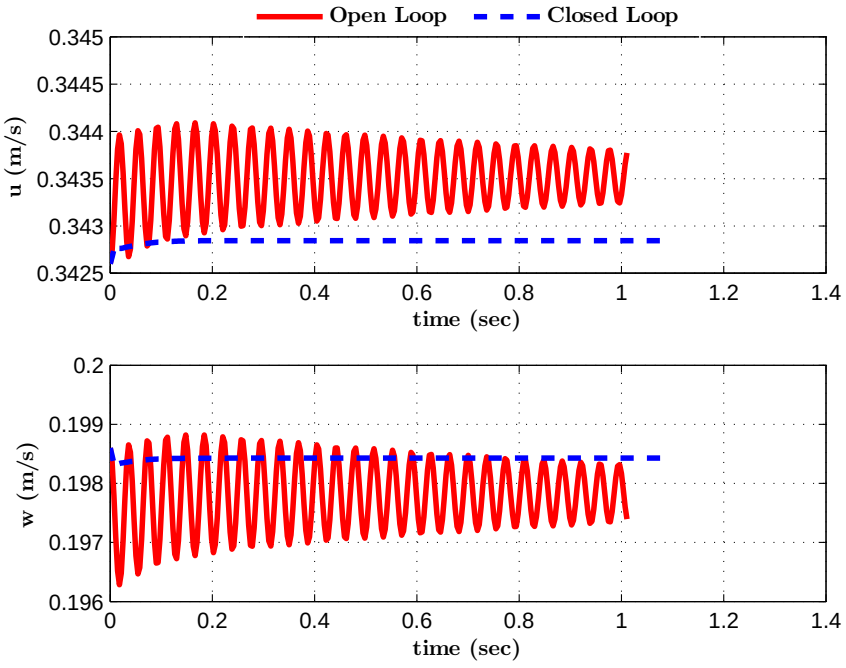

Figure 6.9. Body velocities.

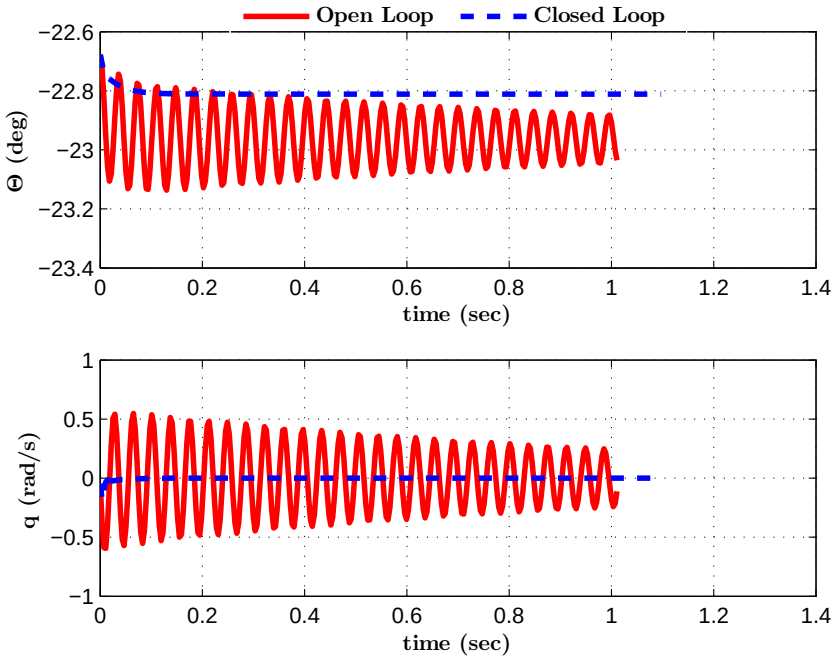

Figure 6.10. Body pitch angle and pitch rate.

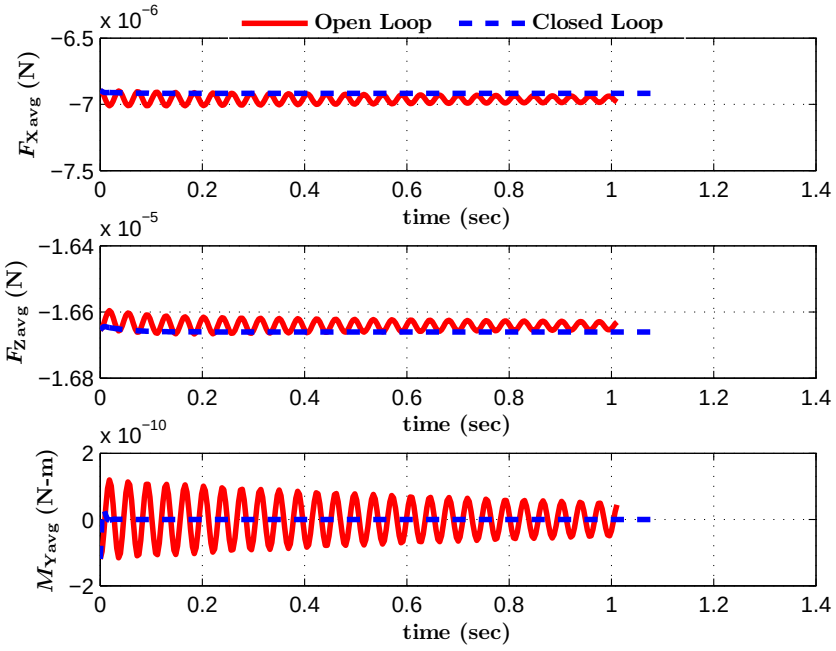

Figure 6.11. Cycle-averaged forces and pitching moment.

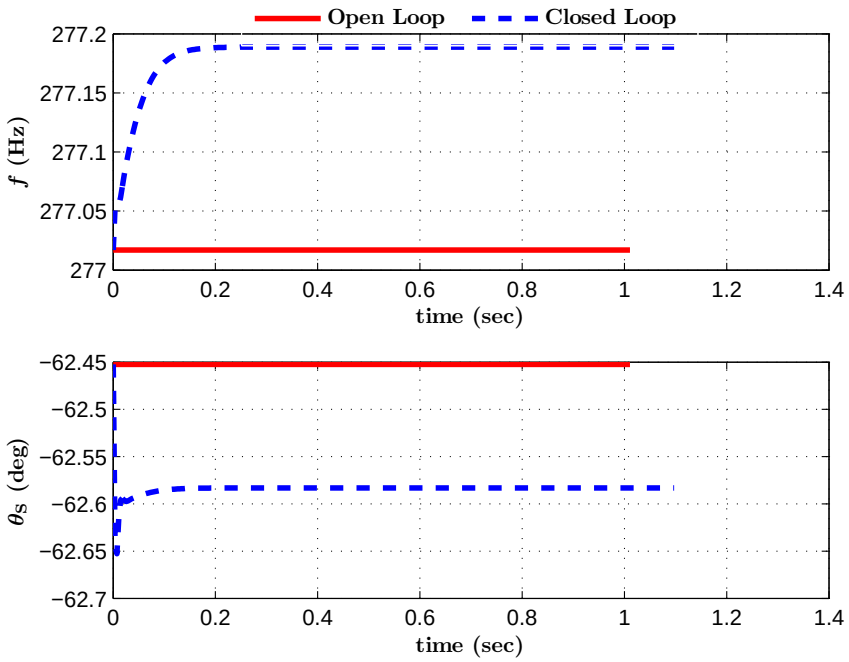

Figure 6.12. Input frequency f and stroke plane pitch angle θ_{S}.

6.8 Micro-flyer with Scaled Mass Properties

Previous section described the procedure to perform a closed-loop control of the micro-flyer. Results showed that the micro-flyer model could perform a steady state descent. In this section, a new micro-flyer model is used for the control design, such that its mass properties are scaled. A scaling factor 'γ' is introduced so as to scale the mass and mass moment of inertia of the micro-flyer model. In the practical application, it is similar to material of different density to build the micro-flyer without changing its volume. The new mass of the micro-flyer body is therefore

$$m_{\text{sbody}} = \gamma m_{\text{body}} \tag{6.58}$$

and I_{sByy} is the corresponding new mass moment of inertia about the y-axis. For this case $\gamma = 0.089$.

Trim analysis conducted on the scaled micro-flyer model yields trim points for a steady state climb (Tab. 6.5) and a straight & level flight (Tab. 6.6).

Table 6.5. Trim point $(\mathbf{X_e}, \mathbf{U_e})$ for steady climb

Variable	u_{e} cm/s	w_{e} cm/s	Θ_{e} deg	q_{e} rad/s	f_{e} Hz	θ_{Se} deg
Value	4.36	-3.77	-2.12	-0.263	185.11	-90.0

Table 6.6. Trim point $(\mathbf{X_e}, \mathbf{U_e})$ for straight & level flight

Variable	u_{e} cm/s	w_{e} cm/s	Θ_{e} deg	q_{e} rad/s	z_{e} cm	f_{e} Hz	θ_{Se} deg
Value	5.29	-3.48	-34.09	-0.225	-500.0	169.9	-58.45

Same procedure is followed to performed closed-loop control for the two flight conditions. The optimal gain matrices for steady climb and straight & level flight are found to be

$$\mathbf{K_C} = \begin{bmatrix} 15.805 & -28 & 2.55 & 0.104 \\ -0.156 & 0.182 & -0.718 & -0.007 \end{bmatrix} \tag{6.59}$$

$$\mathbf{K_{SL}} = \begin{bmatrix} 2.605 & -11.155 & -51.04 & -0.164 \\ -0.074 & 0.109 & -0.621 & -0.005 \end{bmatrix} \tag{6.60}$$

respectively. Figures 6.14 to 6.18 show the results for steady climb, while figures 6.20 to 6.24 show the straight & level flight results. It is to be noted that the trim input frequency for a steady climb is 185 Hz, higher than that for straight & level flight, which is 170 Hz. This means that the micro-flyer is trying to reduce the wing flapping frequency to maintain its altitude. Also, these frequency magnitudes are much less than the one needed for steady descent for the old micro-flyer model. This is because since the new micro-flyer model is lighter and requires less force (see Fig. 6.17 and Fig. 6.23) to fly than the old micro-flyer model (see Fig. 6.11). The saturation blocks ensure that the control inputs never go beyond the acceptable limits (see Fig. 6.18 and Fig. 6.24).

6.8.1 Combined Straight & Level and Climb Maneuver

The trim analysis conducted with the scaled model properties showed that the micro-flyer can achieve a steady climb as well as straight & level flight. In this section, a combined straight & level and climb flight maneuver is performed, in which the micro-flyer would initially perform a straight & level flight, then do a steady climb for certain period, and finally end with a straight & level flight. Appropriate gains and trim values for the two steady-state flight conditions are used. In order to have

a smooth transition between the flight conditions a 'gain scheduling law' is proposed which interpolates between the two flight gain and trim values. The gain scheduling law is given by

$$\mathbf{K} = (1 - \sigma)\,\mathbf{K_{SL}} + \sigma \mathbf{K_C} \tag{6.61}$$

where σ is the gain scheduling parameter. From the equation, it is seen that for straight & level flight, $\sigma = 0$, while for steady climb, $\sigma = 1$. To perform the maneuver, σ is defined to be a linear function of time, such that

$$\sigma = \begin{cases} 0 & \text{if } t < 10 \\ 0.1\,(t - 10) & \text{if } 10 \geq t < 20 \\ 1 - 0.1\,(t - 20) & \text{if } 20 \geq t < 30 \\ 0 & \text{if } t > 30 \end{cases} \tag{6.62}$$

where t is the time given in seconds. It is ensured that σ never goes beyond the maximum value of 1. Figures 6.25 to 6.31 show the results for the combined flight maneuver. Fig. 6.25 clearly shows the changes in the micro-flyer inertial velocities during the two transitions, first from straight & level flight to climb, and then from climb back to straight & level flight. The flight maneuver can be seen in Fig. 6.26, where the micro-flyer initially flying straight at 5 meters climbs 0.35 meters before flying straight again. Figures 6.27 and 6.28 show the body velocities and the pitch angle and rate going to their appropriate trim values of the two flight conditions. It is seen from Fig. 6.29 that the cycle-averaged vertical force F_{Zavg} changes smoothly during the flight transitions than the horizontal force. Fig. 6.30 shows the change in the control inputs required to perform the maneuver. The variation of gain scheduling parameter σ with time is shown in Fig. 6.31.

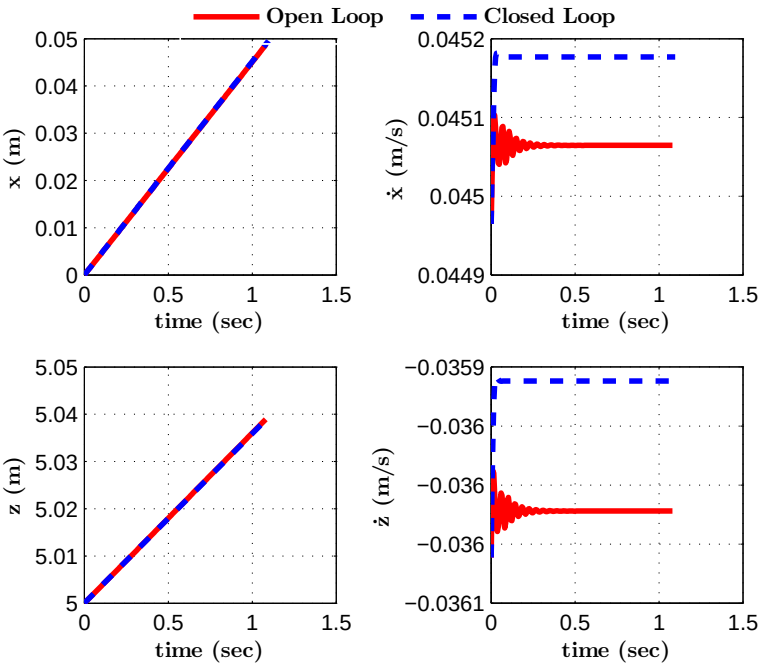

Figure 6.13. Inertial positions and velocities for steady climb.

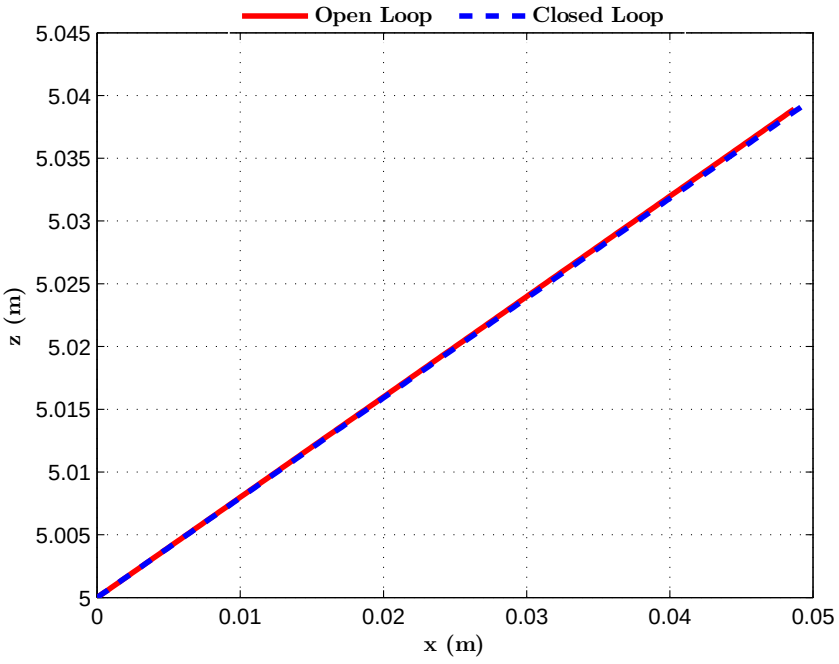

Figure 6.14. x-z position plot for steady climb.

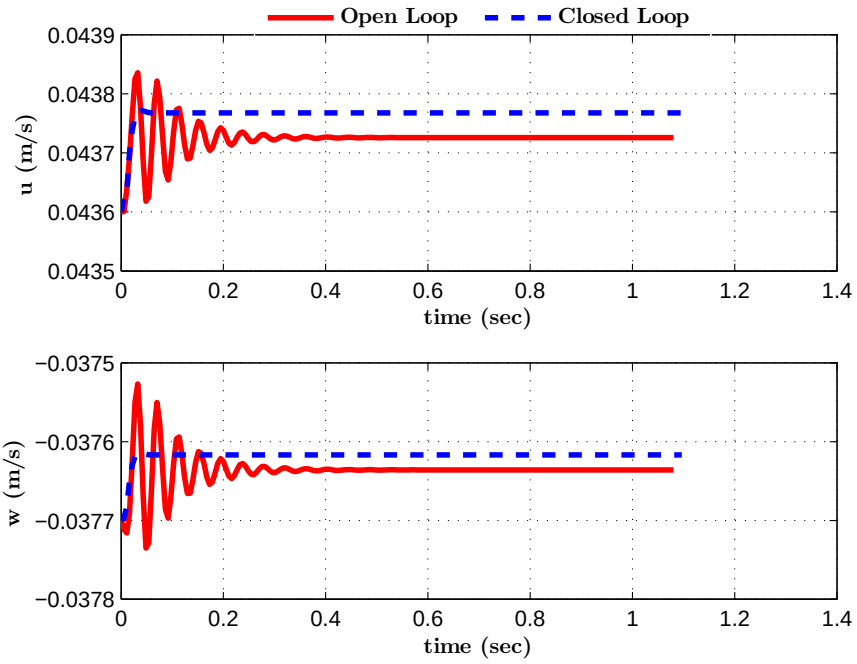

Figure 6.15. Body velocities for steady climb.

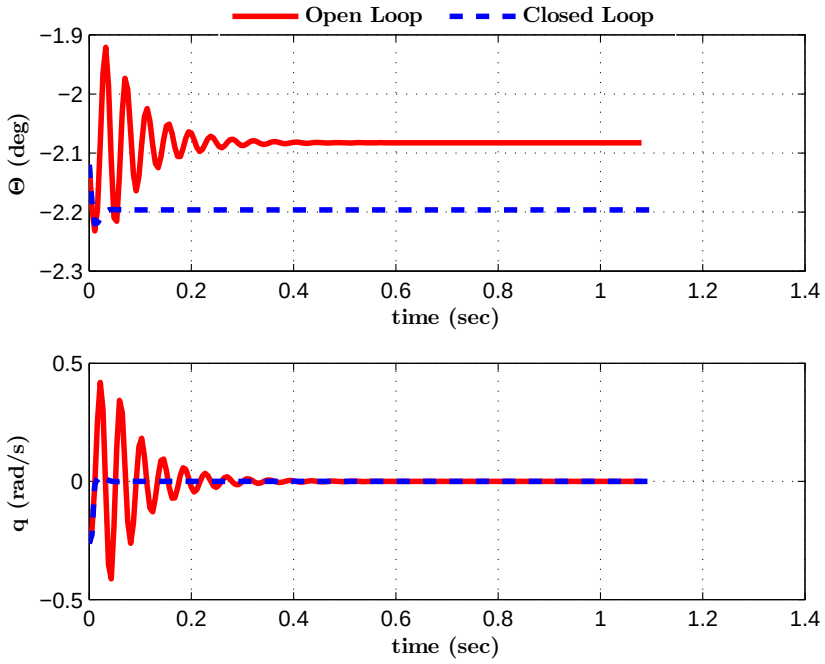

Figure 6.16. Body pitch angle and pitch rate for steady climb.

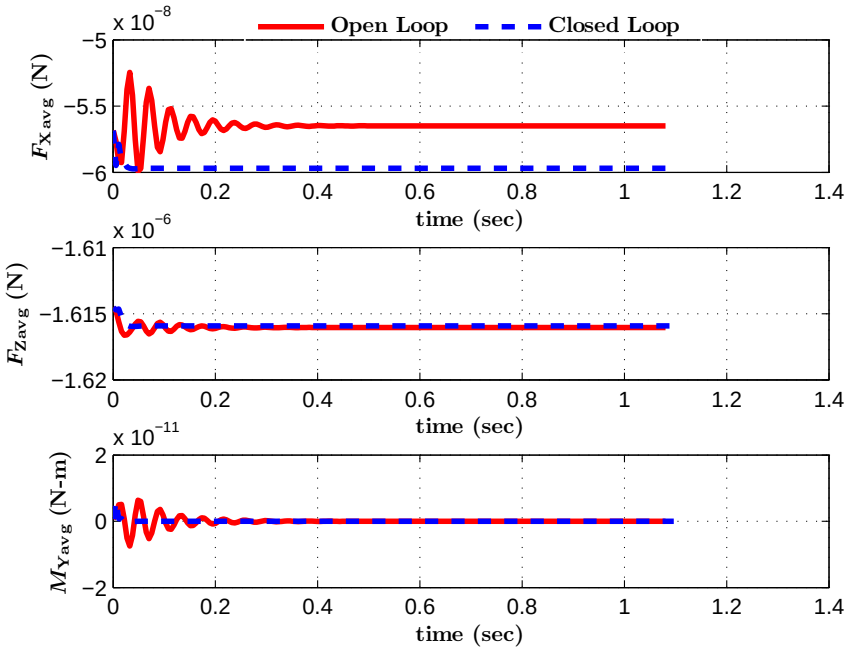

Figure 6.17. Cycle-averaged forces and pitching moment for steady climb.

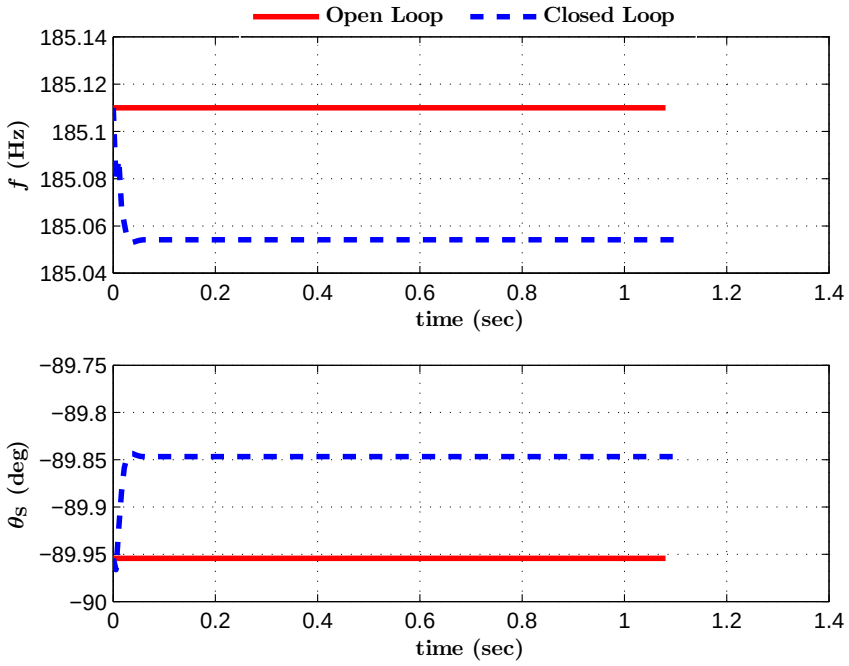

Figure 6.18. Input frequency f and stroke plane pitch angle θ_S for steady climb.

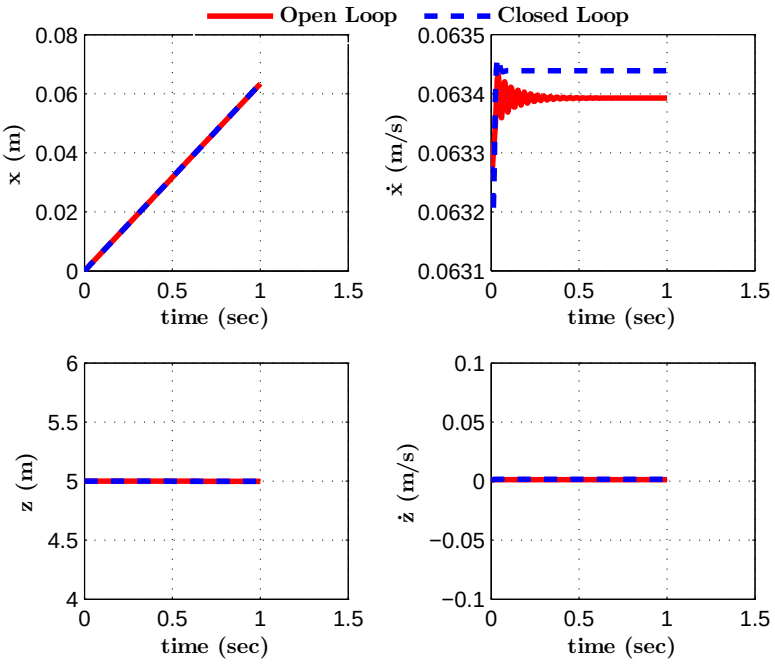

Figure 6.19. Inertial positions and velocities for straight & level flight.

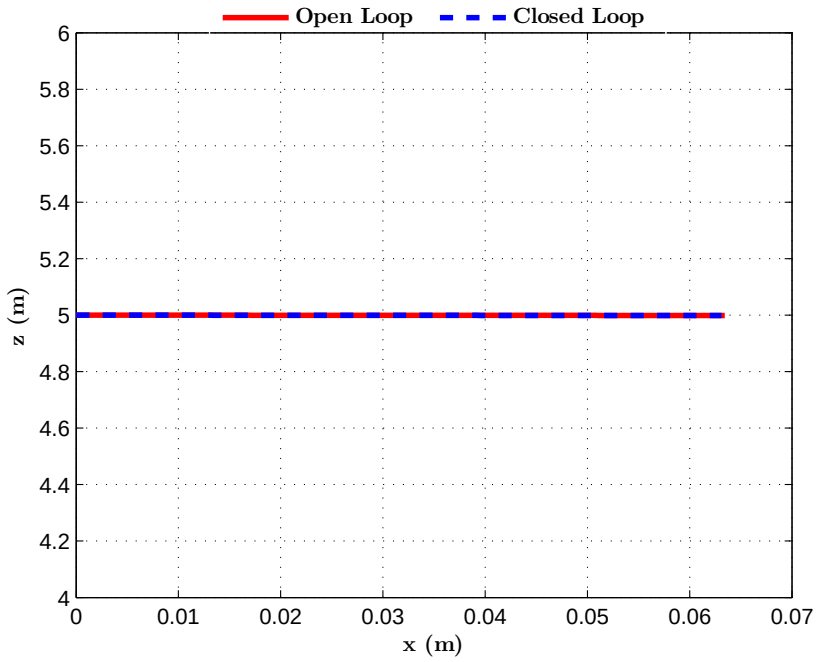

Figure 6.20. x-z position plot for straight & level flight.

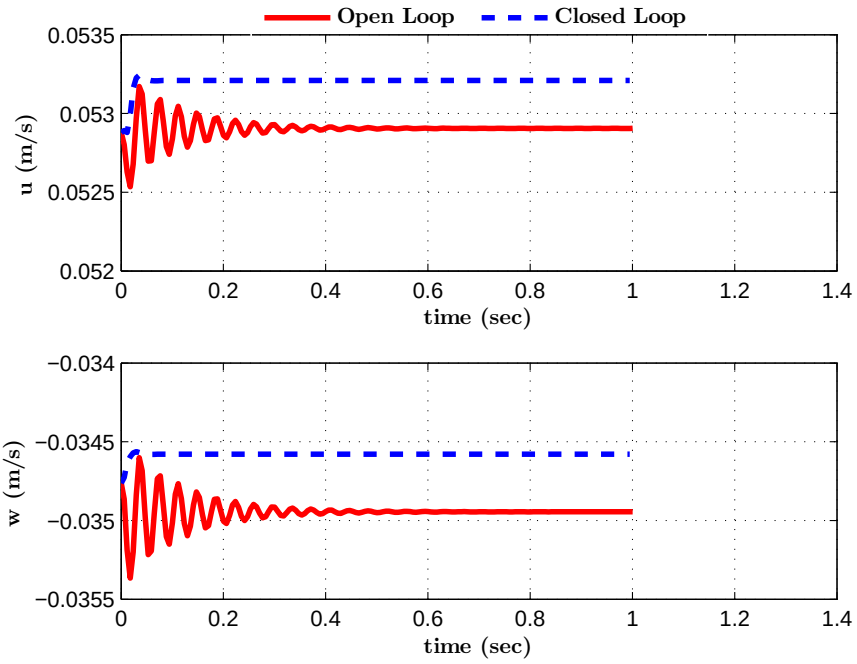

Figure 6.21. Body velocities for straight & level flight.

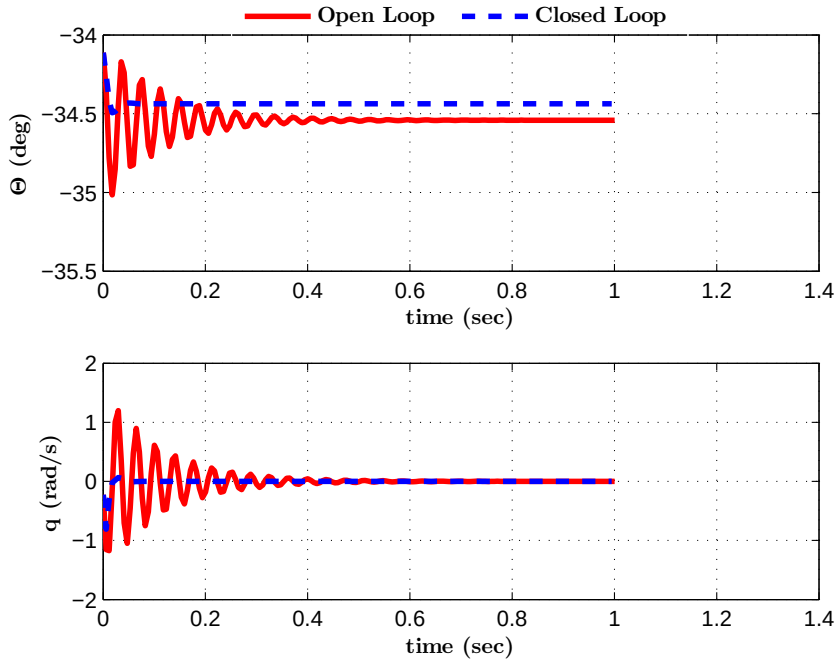

Figure 6.22. Body pitch angle and pitch rate for straight & level flight.

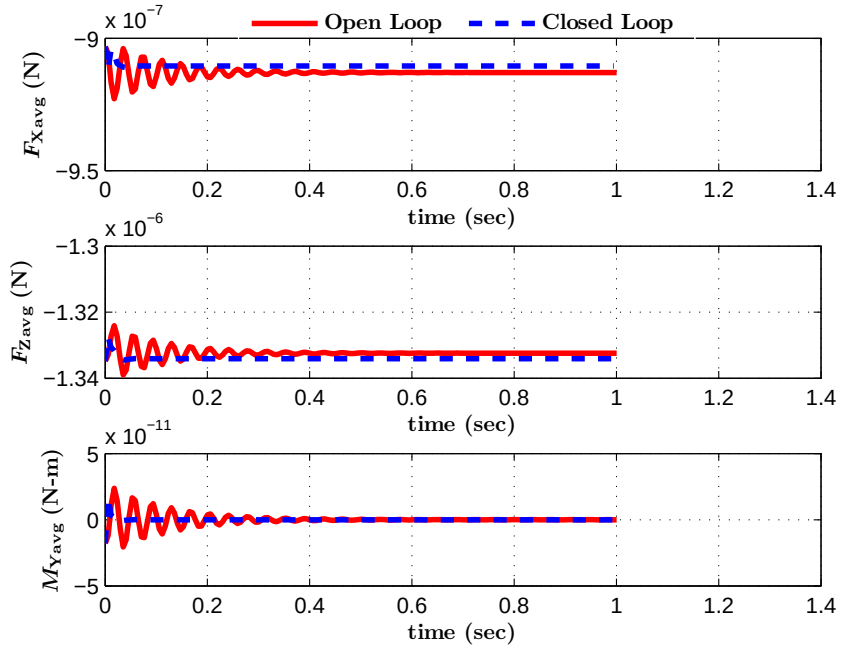

Figure 6.23. Cycle-averaged forces and pitching moment for straight & level flight.

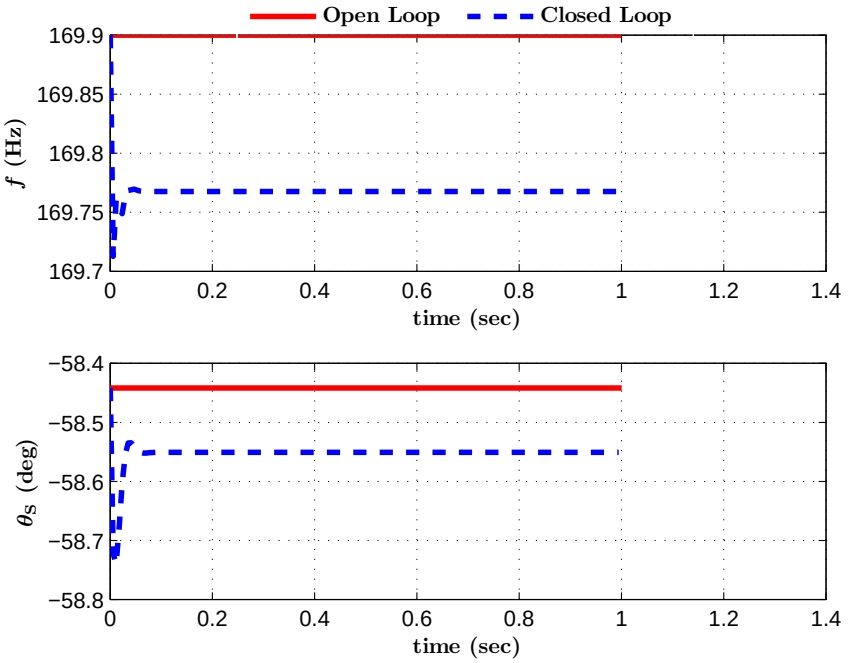

Figure 6.24. Input frequency f and stroke plane pitch angle θ_S for straight & level flight.

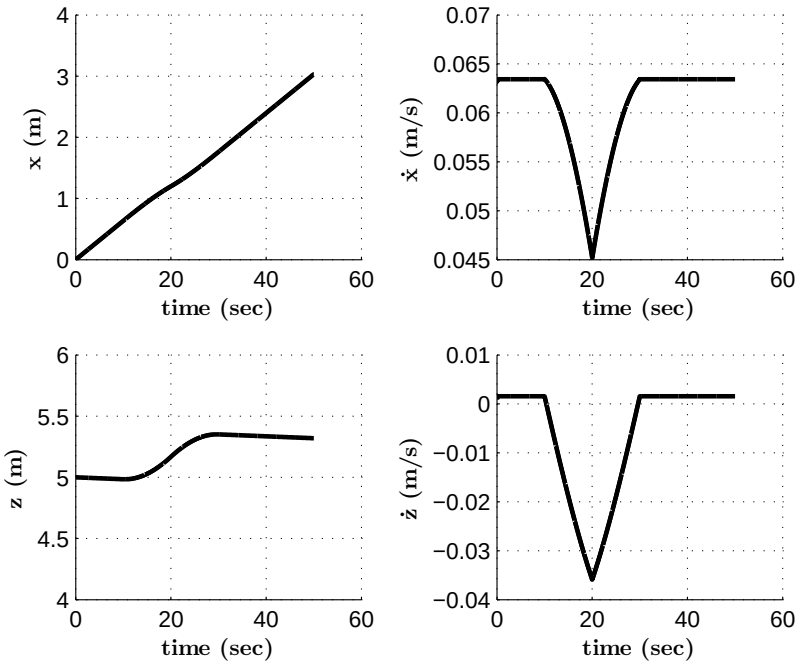

Figure 6.25. Inertial positions and velocities for combined flight maneuver.

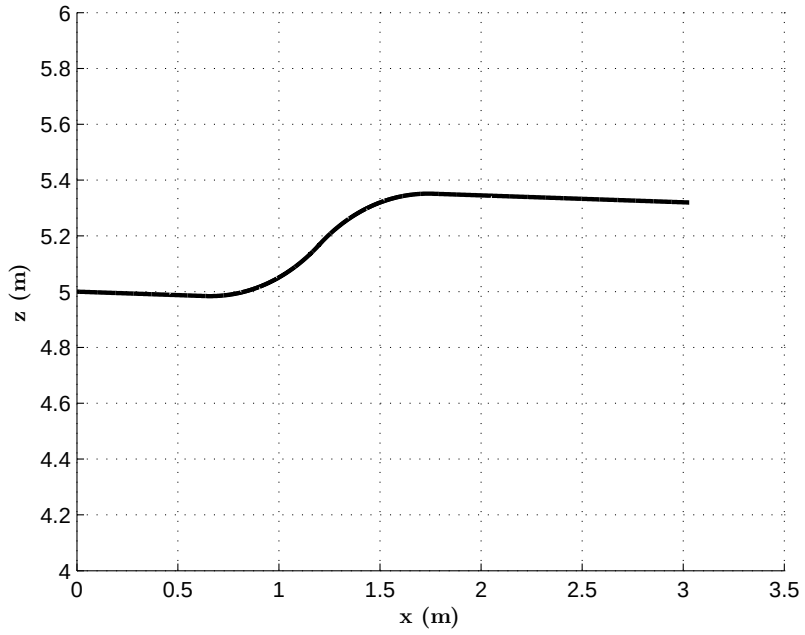

Figure 6.26. x-z position plot for combined flight maneuver.

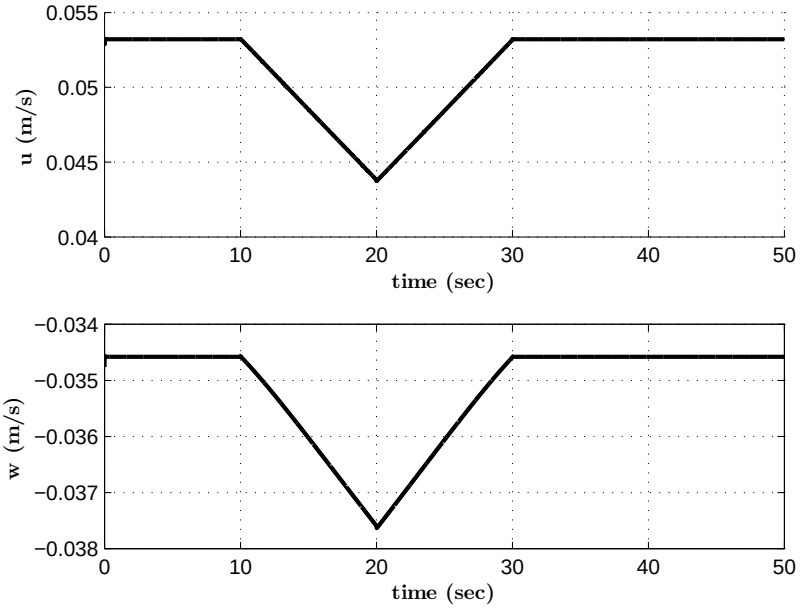

Figure 6.27. Body velocities for combined flight maneuver.

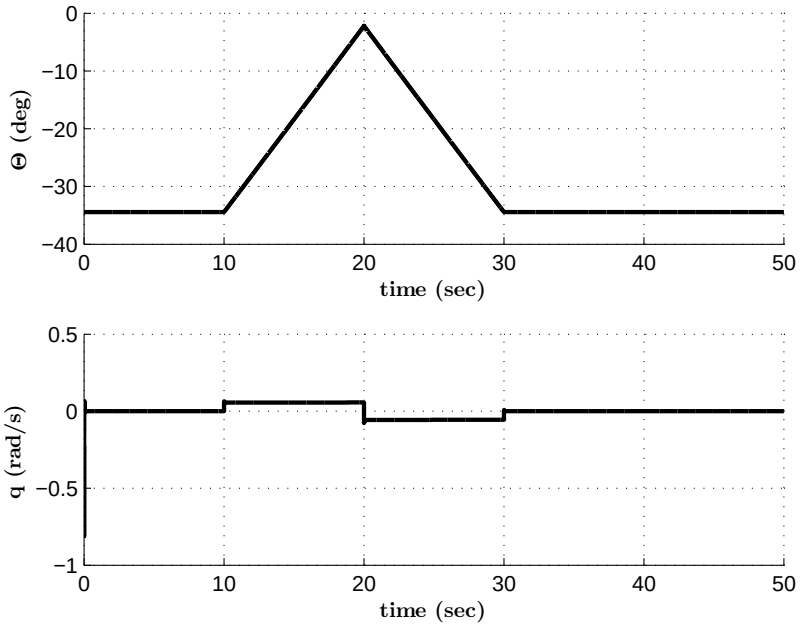

Figure 6.28. Body pitch angle and pitch rate for combined flight maneuver.

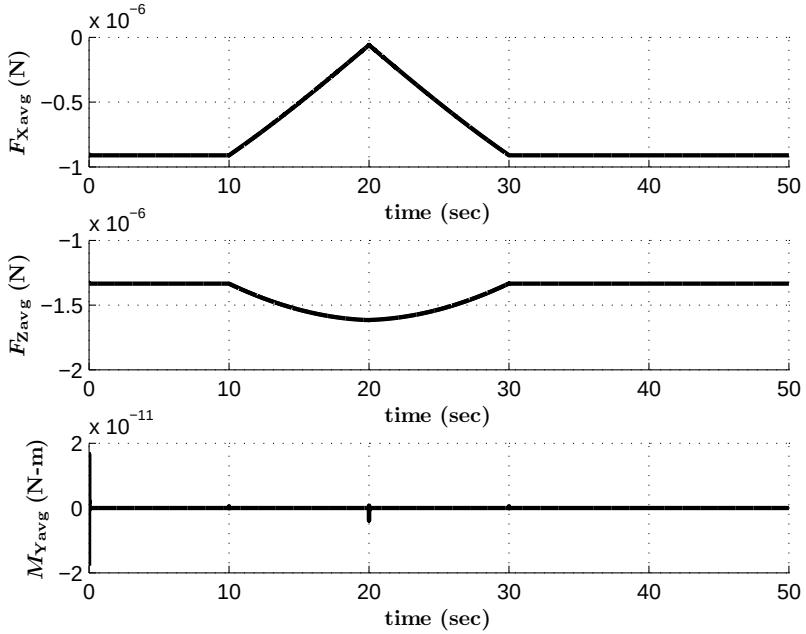

Figure 6.29. Cycle-averaged forces and pitching moment for combined flight maneuver.

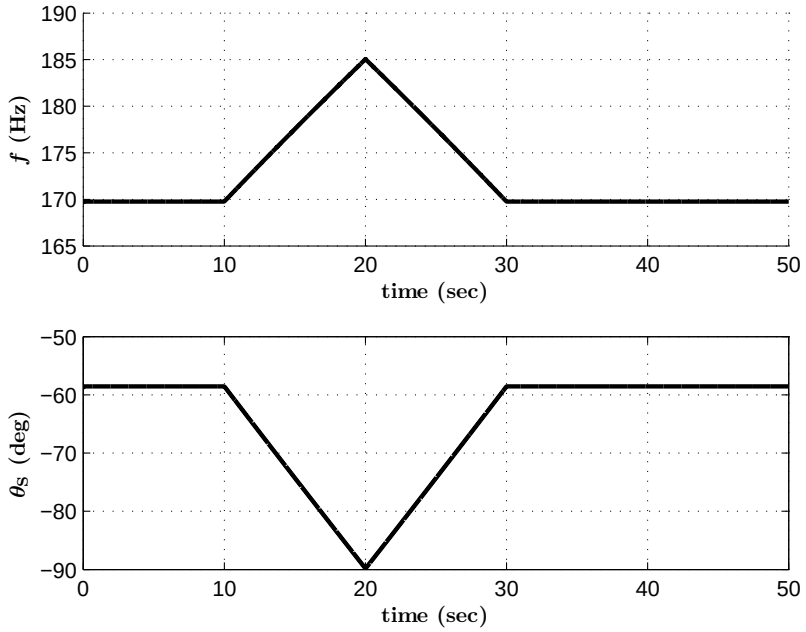

Figure 6.30. Input frequency f and stroke plane pitch angle θ_S for combined flight maneuver.

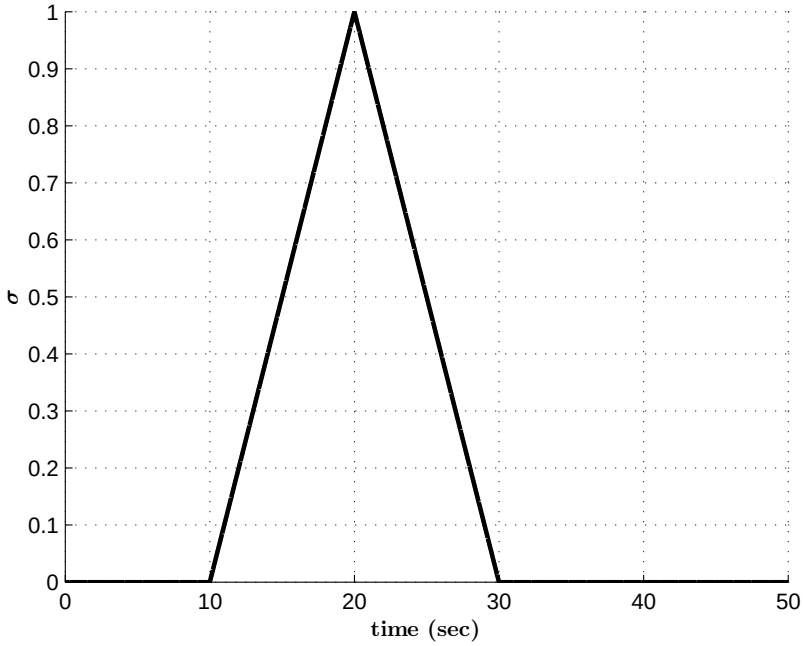

Figure 6.31. Gain scheduling parameter σ.

6.9 Summary of Results

The results show that the dynamic states of the micro-flyer stabilized to the trim values at a faster rate by implementing a linear control technique. Trim study of the nonlinear dynamics revealed which steady state flight condition could be achieved for the micro-flyer model using the cycle-averaged aerodynamic model for straight path flapping. The results also highlight the importance of the model properties of the micro-flyer to achieve certain flight maneuvers.

The nonlinear dynamics framework is a function of the aerodynamic model, which will vary with the flapping trajectory chosen. The framework will help in ascertaining the ideal values of micro-flyer model properties in order to achieve different flight maneuvers using a particular flapping trajectory.

CHAPTER 7

CONCLUDING REMARKS

7.1 Summary

In this research, a nonlinear dynamics framework to develop flapping wing micro-flyers was proposed. Every aspect of the framework, viz., the kinematics, dynamics and the aerodynamic model was discussed in detail.

The primary focus was to develop an aerodynamic model which would be representative of the unsteady aerodynamics involved in flapping wing insect flight. Efforts were taken towards achieving this goal, starting with the parametric study performed on straight and figure-8 flapping trajectories using a two-dimensional wing section of a micro-flyer model. This work dealt with determining the variables that affect the force generation by a flapping wing motion.

The next task was to define the identified variables in a non-dimensional form. This helped in creating a generic model representing aerodynamics for different insects. The defined non-dimensional parameters were the local Reynolds number Re_{l}, the Strouhal number St, the geometric function G and the stroke angle of attack α_{S}. A procedure was described to perform sensitivity analysis using the non-dimensional parameters in a design of experiments (DOE), and then determine the expressions for cycle-averaged force coefficients in terms of the non-dimensional parameters.

Results of the grid validation and convergence study were presented. The validated grid was then used to perform parametric study and sensitivity analysis of the non-dimensional parameters using large DOE data-set.

Flight dynamics analysis was performed using a micro-flyer model based on *Drosophila*. Trim study showed which steady state flight conditions could be achieved for a given set of micro-flyer model properties. An example was illustrated where by scaling the mass properties the micro-flyer could perform more maneuvers. An LQR control design was used for the closed-loop control. Results for the open and closed-loop simulations were presented. The study showed that the nonlinear dynamics framework could be used to determine the values for model properties of a micro-flyer that would enable it to perform different flight maneuvers.

APPENDIX A

DERIVATIONS & FORMULAE

A.1 Determination of Initial Wall Spacing

The procedure to determine the initial wall spacing is taken from White [71]. The local Reynolds number of the flow along the surface is given by

$$Re_x = \frac{\rho V_\infty c}{\mu} \tag{A.1}$$

From the skin friction law for turbulent flat-plate flow, the formula skin coefficient of the wall is obtained as

$$c_\mathrm{f} = \frac{0.027}{Re_x^{1/7}} \tag{A.2}$$

The wall shear stress is given by

$$\tau_\mathrm{w}(x) = \frac{\rho V_\infty^2 c_\mathrm{f}}{2} \tag{A.3}$$

Friction velocity at the wall is given by

$$u^* = \sqrt{\frac{\tau_\mathrm{w}(x)}{\rho}} \tag{A.4}$$

The initial wall spacing is given by the formula

$$\delta = \frac{y^+ \mu}{u^* \rho} \tag{A.5}$$

where y^+ is the dimensionless wall distance.

REFERENCES

[1] M. H. Dickinson, L. F.-O., and S. Sane, "Wing Rotation and the Aerodynamic Basis of Insect Flight," *Science*, vol. 284, no. 5422, pp. 1954–1960, June 1999.

[2] R. Kumar and S. Shkarayev, "Kinematics and Aerodynamic Response of Locusts in Sideslip," *51st AIAA Aerospace Sciences Meeting including the New Horizons Forum and Aerospace Exposition*, vol. 7, no. 2, 2013.

[3] S. Shkarayev and R. Kumar, "Kinematics and Inertial Effects in Locust Flapping Wings," *Experimental Mechanics*, no. July 2014, 2015.

[4] ——, "Simultaneous measurement of aerodynamic forces and kinematics in flapping wings of tethered locust," *Bioinspiration & Biomimetics*, vol. 10, no. 6, p. 066003, 2015.

[5] J. M. Zanker, "The Wing Beat of Drosophila Melanogaster. I. Kinematics," *Philosophical Transactions of the Royal Society B: Biological Sciences*, vol. 327, no. 1238, pp. 1–18, Feb. 1990.

[6] J. M. Zanker and K. G. Gotz, "The Wing Beat of Drosophila Melanogaster. II. Dynamics," *Philosophical Transactions of the Royal Society B: Biological Sciences*, vol. 327, no. 1238, pp. 19–44, Feb. 1990.

[7] C. Ellington, "The aerodynamics of hovering insect flight . I. The quasi-steady analysis," *Philosophical Transactions of the Royal Society of London. Series B: Biological Sciences*, vol. 305, no. 1122, pp. 1–15, 1984.

[8] ——, "The aerodynamics of hovering insect flight. II. Morphological parameters," *Philosophical Transactions of the Royal Society of London. B, Biological Sciences*, vol. 305, no. 1122, pp. 17–40, 1984.

[9] ——, "The aerodynamics of hovering insect flight. III. Kinematics," *Philosophical Transactions of the Royal Society of London. Series B: Biological Sciences*, vol. 305, no. 1122, pp. 41–78, 1984.

[10] ——, "The aerodynamics of hovering insect flight. IV. aerodynamic mechanisms," *Philosophical Transactions of the Royal Society B: Biological Sciences*, vol. 305, no. 1122, pp. 79–113, 1984.

[11] ——, "The aerodynamics of hovering insect flight. V. A vortex theory," *Philosophical Transactions of the Royal Society of London. Series B: Biological Sciences*, vol. 305, no. 1122, pp. 115–144, 1984.

[12] T. Weis-Fogh, "Quick estimates of flight fitness in hovering animals, including novel mechanisms for lift production," *Journal of Experimental Biology*, vol. 59, no. 1, pp. 169–230, 1973.

[13] H. Wagner, "Über die Entstehung des dynamischen Auftriebes von Tragflügeln," *ZAMM - Zeitschrift für Angewandte Mathematik und Mechanik*, vol. 5, no. 1, pp. 17–35, 1925.

[14] C. Ellington, "Unsteady aerodynamics of insect flight," *Symposia of the Society for Experimental Biology*, vol. 49, pp. 109–129, 1994.

[15] W. Shyy, Y. Lian, J. Tang, H. Liu, P. Trizila, B. Stanford, L. Bernal, C. Cesnik, P. Friedmann, and P. Ifju, "Computational aerodynamics of low Reynolds number plunging, pitching and flexible wings for MAV applications," *Acta Mechanica Sinica*, vol. 24, no. 4, pp. 351–373, July 2008.

[16] M. Sun and D. Gang, "Lift and power requirements of hovering insect flight," *Acta Mechanica Sinica*, vol. 19, no. 5, 2003.

[17] J.-S. Lee, J.-H. Kim, and C. Kim, "Numerical Study on the Unsteady-Force-Generation Mechanism of Insect Flapping Motion," *AIAA Journal*, vol. 46, no. 7, pp. 1835–1848, July 2008.

[18] R. Ramamurti and W. C. Sandberg, "A three-dimensional computational study of the aerodynamic mechanisms of insect flight." *The Journal of Experimental Biology*, vol. 205, no. Pt 10, pp. 1507–18, May 2002.

[19] P. Bai, E. Cui, F. Li, W. Zhou, and B. Chen, "A new bionic MAVs flapping motion based on fruit fly hovering at low Reynolds number," *Acta Mechanica Sinica*, vol. 23, no. 5, pp. 485–493, Sept. 2007.

[20] J. Tang, D. Viieru, and W. Shyy, "Effects of Reynolds Number and Flapping Kinematics on Hovering Aerodynamics," *AIAA Journal*, vol. 46, no. 4, pp. 967–976, 2008.

[21] M. F. Platzer, K. D. Jones, J. Young, and J. C. S. Lai, "Flapping Wing Aerodynamics: Progress and Challenges," *AIAA Journal*, vol. 46, no. 9, pp. 2136–2149, Sept. 2008.

[22] H. E. Taha, M. R. Hajj, and A. H. Nayfeh, "Flight dynamics and control of flapping-wing MAVs: A review," *Nonlinear Dynamics*, vol. 70, no. 2, pp. 907–939, 2012.

[23] G. K. Taylor and A. L. R. Thomas, "Dynamic flight stability in the desert locust Schistocerca gregaria," *Journal of Experimental Biology*, vol. 206, no. 16, pp. 2803–2829, 2003.

[24] G. K. Taylor and R. Zbikowski, "Nonlinear time-periodic models of the longitudinal flight dynamics of desert locusts Schistocerca gregaria," *Journal of The Royal Society Interface*, vol. 2, no. 3, pp. 197–221, 2005.

[25] T. L. Hedrick and T. L. Daniel, "Flight control in the hawkmoth Manduca sexta: the inverse problem of hovering." *The Journal of Experimental Biology*, vol. 209, no. Pt 16, pp. 3114–3130, 2006.

[26] S. P. Sane and M. H. Dickinson, "The aerodynamic effects of wing rotation and a revised quasi-steady model of flapping flight," *Journal of Experimental Biology*, vol. 205, no. 8, pp. 1087–1096, 2002.

[27] L. W. Traub, "Analysis and estimation of the lift components of hovering insects," *Journal of Aircraft*, vol. 41, no. 2, pp. 284–289, 2004.

[28] G. J. Berman and Z. J. Wang, "Energy-minimizing kinematics in hovering insect flight," *Journal of Fluid Mechanics*, vol. 582, p. 153, June 2007.

[29] A. Andersen, U. Pesavento, and Z. J. Wang, "Analysis of transitions between fluttering, tumbling and steady descent of falling cards," *Journal of Fluid Mechanics*, vol. 541, pp. 91–104, 2005.

[30] C. T. Orlowski and A. R. Girard, "Modeling and Simulation of Nonlinear Dynamics of Flapping Wing Micro Air Vehicles," *AIAA Journal*, vol. 49, no. 5, pp. 969–981, May 2011.

[31] Z. A. Khan and S. K. Agrawal, "Force and moment characterization of flapping wings for micro air vehicle application," in *American Control Conference, 2005. Proceedings of the 2005*, 2005, pp. 1515–1520.

[32] S. Ansari, R. bikowski, and K. Knowles, "Aerodynamic modelling of insect-like flapping flight for micro air vehicles," *Progress in Aerospace Sciences*, vol. 42, no. 2, pp. 129–172, Feb. 2006.

[33] S.-J. Chung and M. Dorothy, "Neurobiologically inspired control of engineered flapping flight," *Journal of Guidance, Control, and Dynamics*, vol. 33, no. 2, pp. 440–453, 2010.

[34] X. Deng, L. Schenato, W. C. Wu, and S. S. Sastry, "Flapping flight for biomimetic robotic insects: Part I-system modeling," *Robotics, IEEE Transactions on*, vol. 22, no. 4, pp. 776–788, 2006.

[35] X. Deng, L. Schenato, and S. S. Sastry, "Flapping flight for biomimetic robotic insects: Part II-flight control design," *Robotics, IEEE Transactions on*, vol. 22, no. 4, pp. 789–803, 2006.

[36] D. B. Doman, M. W. Oppenheimer, and D. O. Sigthorsson, "Dynamics and control of a biomimetic vehicle using biased wingbeat forcing functions: Part ii: Controller," *AIAA , Washington*, vol. 1024, 2010.

[37] M. W. Oppenheimer, D. B. Doman, and D. O. Sigthorsson, "Dynamics and control of a biomimetic vehicle using biased wingbeat forcing functions: Part i-aerodynamic model," in *Proceedings of the 48th AIAA Aerospace Sciences Meeting Including the New Horizons Forum and Exposition, Orlando, Florida, USA*, 2010.

[38] D. B. Doman, M. W. Oppenheimer, and D. O. Sigthorsson, "Wingbeat shape modulation for flapping-wing micro-air-vehicle control during hover," *Journal of Guidance Control and Dynamics*, vol. 33, no. 3, pp. 724–739, 2010.

[39] M. W. Oppenheimer, D. B. Doman, and D. O. Sigthorsson, "Dynamics and Control of a Minimally Actuated Biomimetic Vehicle : Part II - Control," in *AIAA GNC 2009*, no. August, 2009, pp. 1–23.

[40] D. B. Doman, M. W. Oppenheimer, and D. O. Sigthorsson, "Dynamics and Control of a Minimally Actuated Biomimetic Vehicle: Part I- Aerodynamic Model," in *AIAA Guidance Navigation and Control Conference*, Chicago, 2009, pp. 1–25.

[41] L. Schenato, D. Campolo, and S. S. Sastry, "Controllability issues in flapping flight for biomimetic micro aerial vehicles (mavs)," in *Decision and Control, 2003. Proceedings. 42nd IEEE Conference on*, 2003, pp. 6441–6447.

[42] W. Su and C. Cesnik, "Flight dynamic stability of a flapping wing MAV in hover," in *52nd AIAA/ASME/ASCE/ AHS/ASC Structures, Structural Dynamics, and Materials Conference*, Denver, Colorado, 2011.

[43] U. Pesavento and Z. J. Wang, "Navier-Stokes solutions, model of fluid forces, and center of mass elevation," *Physical review letters*, vol. 93, no. 14, 2004.

[44] A. A. Rege, B. H. Dennis, and K. Subbarao, "Parametric Study on Wing Flapping Path of a Micro Air Vehicle Using Computational Techniques," in *51st AIAA Aerospace Sciences Meeting including the New Horizons Forum and Aerospace Exposition*, Grapevine, 2013.

[45] ——, "Sensitivity Analysis Of The Factors Affecting Force Generation By Wing Flapping Motion," in *ASME 2013 International Mechanical Engineering Congress & Exposition*, San Diego, 2013.

[46] A. A. Rege, K. Subbarao, and B. H. Dennis, "Nonlinear Dynamics of Flapping Wing MAV using Cycle-Averaged Force Coefficients," in *52nd Aerospace Sciences Meeting, 13-17 January 2014*, 2014.

[47] A. Rege, "CFD Based Aerodynamic Modeling to Study Flight Dynamics of a Flapping Wing Micro Air Vehicle," Master's thesis, University of Texas at Arlington, 2012.

[48] F.-O. Lehmann and S. Pick, "The aerodynamic benefit of wing-wing interaction depends on stroke trajectory in flapping insect wings." *The Journal of Experimental Biology*, vol. 210, no. Pt 8, pp. 1362–77, Apr. 2007.

[49] A. Ueno and B. H. Dennis, "Optimization of Flapping Airfoil Motion with Computational Fluid Dynamics," *International Review of Aerospace Engineering (I.RE.AS.E)*, vol. 2, no. April, pp. 104–111, 2009.

[50] I. B. Celik, U. Ghia, P. J. Roache, and Others, "Procedure for Estimation and Reporting of Uncertainty Due to Discretization in CFD Applications," *Journal of Fluids Engineering-Transactions of the ASME*, vol. 130, no. 7, 2008.

[51] F. Stern, R. V. Wilson, H. W. Coleman, and E. G. Paterson, "Comprehensive approach to verification and validation of CFD simulationspart 1: methodology

and procedures," *Journal of Fluids Engineering-Transactions of the ASME*, vol. 123, no. 4, pp. 793–802, 2001.

[52] Various, "AGARD-R-702 - Compendium of Unsteady Aerodynamic Measurments," NATO Research and Technology Organization, Tech. Rep., 1982.

[53] Z. J. Wang, J. M. Birch, and M. H. Dickinson, "Unsteady forces and flows in low Reynolds number hovering flight: two-dimensional computations vs robotic wing experiments," *Journal of Experimental Biology*, vol. 207, no. 3, pp. 449–460, Feb. 2004.

[54] P. R. Spalart and S. R. Allmaras, "A one-equation turbulence model for aerodynamic flows," in *AIAA 30th Aerospace Sciences Meeting and Exhibit*, Reno, NV, 1992, pp. 5–21.

[55] C. P. Ellington and A. L. Van Den Berg, Coen Willmott, Alexander P Thomas, "Leading-edge vortices in insect flight," *Nature*, vol. 384, no. 6610, pp. 626–630, 1996.

[56] S. P. Sane, "The aerodynamics of insect flight," *Journal of Experimental Biology*, vol. 206, no. 23, pp. 4191–4208, Dec. 2003.

[57] Z. J. Wang, "Dissecting insect flight," *Annu. Rev. Fluid Mech.*, vol. 37, pp. 183–210, 2005.

[58] J. M. Birch and M. H. Dickinson, "The influence of wing–wake interactions on the production of aerodynamic forces in flapping flight," *Journal of Experimental Biology*, vol. 206, no. 13, pp. 2257–2272, 2003.

[59] P. Trizila, C.-k. Kang, M. Visbal, and W. Shyy, "A surrogate model approach in 2d versus 3d flapping wing aerodynamic analysis," *AIAA Paper*, vol. 5914, 2008.

[60] P. Freymuth, "Thrust generation by an airfoil in hover modes," *Experiments in Fluids*, vol. 9, no. 1-2, pp. 17–24, 1990.

[61] P. Trizila, C.-k. Kang, M. R. Visbal, and W. Shyy, "Unsteady fluid physics and surrogate modeling of low Reynolds number, flapping airfoils," *AIAA Paper*, vol. 3821, 2008.

[62] B. Etkin, *Dynamics of Atmospheric Flight*. John Wiley & Sons, 1972.

[63] B. R. Munson, D. F. Young, and T. H. Okiishi, *Fundamentals of fluid mechanics*. New York: John Wiley & Sons, 1990.

[64] M. Sun, J. Wang, and Y. Xiong, "Dynamic flight stability of hovering insects," *Acta Mechanica Sinica*, vol. 23, no. 3, pp. 231–246, May 2007.

[65] B. L. Stevens and F. L. Lewis, *Aircraft Control and Simulation*. John Wiley & Sons, 2003.

[66] M. Vidyasagar, *Nonlinear Systems Analysis*. Siam, 2002.

[67] V. M. Popov, *Hiperstabilitatea Sistemelor Automate*. Ed. Academiei Republicii Socialiste Romania, 1966.

[68] V. Belevitch, *Classical Network Theory*. Holden-Day, 1968.

[69] M. Hautus, "Controllability and observability conditions of linear autonomous systems," *PROCEEDINGS OF THE KONINKLIJKE NEDERLANDSE AKADEMIE VAN WETENSCHAPPEN SERIES A-MATHEMATICAL SCIENCES*, vol. 72, no. 5, pp. 443–448, 1969.

[70] A. E. Bryson, *Applied optimal control: optimization, estimation and control*. CRC Press, 1975.

[71] F. M. White, *Fluid Mechanics*, 7th ed. New York: McGraw Hill, 2011.

BIOGRAPHICAL STATEMENT

Alok Rege was born in the city of Mumbai, India in 1984. He obtained his Bachelor's degree in Aeronautical Engineering with a major in Aerodynamics from the Aeronautical Society of India (AeSI), New Delhi in 2009. He came to US in 2010 to pursue a Masters degree in Aerospace engineering at the University of Texas, Arlington (UTA) under the guidance of professors Kamesh Subbarao (Aerospace Systems Laboratory) and Brian Dennis (Computational Fluid Dynamics Laboratory). After graduation, he was hired as an engineering intern at Cummins Power Generation, Minnesota from July to September 2012. He returned to UTA to begin work on his doctoral dissertation under his professors in Fall 2012, and received the 'Carrizo Oil & Gas Graduate Research Fellowship' for 2012-2013.

Alok has completed an 'Unmanned Vehicle Systems Graduate Certification Program' offered at UTA in May 2015. His research interests include linear & nonlinear dynamics, modeling & control of dynamical systems and state & parameter estimation. He has been a Graduate Teaching Assistant at UTA since 2010. He is a graduate member of AeSI and a student member of AIAA and ASME.